

Computational Study of Turbulent Combustion Systems and Global Reactor Networks

Lu Chen

Dissertation submitted to the faculty of the Virginia Polytechnic Institute and State
University in partial fulfillment of the requirement for degree of

Doctor of Philosophy
In
Mechanical Engineering

Francine Battaglia, Chair
Javid Bayandor
Brian Y. Lattimer
Ayman M. Karim
Mark R. Paul

July 17, 2017
Blacksburg, Virginia

Keywords: Turbulent combustion, turbulence model, chemical reactor network, sensitivity
analysis, reduced chemical mechanism

Computational Study of Turbulent Combustion Systems and Global Reactor Networks

Lu Chen

ABSTRACT

A numerical study of turbulent combustion systems was pursued to examine different computational modeling techniques, namely computational fluid dynamics (CFD) and chemical reactor network (CRN) methods. Both methods have been studied and analyzed as individual techniques as well as a coupled approach to pursue better understandings of the mechanisms and interactions between turbulent flow and mixing, ignition behavior and pollutant formation. A thorough analysis and comparison of both turbulence models and chemistry representation methods was executed and simulations were compared and validated with experimental works. An extensive study of turbulence modeling methods, and the optimization of modeling techniques including turbulence intensity and computational domain size have been conducted. The final CFD model has demonstrated good predictive performance for different turbulent bluff-body flames. The NO_x formation and the effects of fuel mixtures indicated that the addition of hydrogen to the fuel and non-flammable diluents like CO_2 and H_2O contribute to the reduction of NO_x .

The second part of the study focused on developing chemical models and methods that include the detailed gaseous reaction mechanism of GRI-Mech 3.0 but cost less computational time. A new chemical reactor network has been created based on the CFD results of combustion characteristics and flow fields. The proposed CRN has been validated with the temperature and species emission for different bluff-body flames and has shown the capability of being applied to general bluff-body systems. Specifically, the rate of production of NO_x and the sensitivity analysis based on the CRN results helped to summarize the reduced reaction mechanism, which not only provided a promising method to generate representative reactions from hundreds of species and reactions in gaseous mechanism but also presented valuable information of the combustion mechanisms and NO_x formation. Finally, the proposed reduced reaction mechanism from the sensitivity analysis was applied to the CFD simulations, which created a fully coupled process between CFD and CRN, and the results from the reduced reaction mechanism have shown good predictions compared with the probability density function method.

Computational Study of Turbulent Combustion Systems and Global Reactor Networks

Lu Chen

GENERAL AUDIENCE ABSTRACT

Turbulent combustion has been regarded as one of the most typical occurrences with industrial burners, where turbulent flow is produced by large vortex eddies when fuel and oxidizer mixes. Due to increasing demands for energy and concerns for environmental pollution, it is important to have a comprehensive understanding of turbulent combustion processes. To help provide information related to turbulent combustion, computational modeling can be used to give physical insights of the combustion process. A numerical study of turbulent combustion systems was pursued to examine different computational modeling techniques and to understand the mechanisms in terms of fluid dynamics and chemical kinetics. Computational fluid dynamics (CFD) was used to predict the flow field, including gas velocities, temperatures and fuel characteristics. Another computational technique known as the chemical reactor network (CRN) was used to provide information related to the chemical reactions and pollutant production. A method was developed as part of the study to couple the computational methods to pursue better understandings of the mechanisms and interactions between turbulent flow and mixing, ignition behavior and pollutant formation. Results have been compared with experimental data to optimize the modeling techniques and validate the developed model. The CRN model with the detailed gaseous reaction mechanism from the Gas Research Institute GRI-Mech 3.0 created a reacting network across the combustor with flame chemistry details. By post-processing the CRN results using a sensitivity analysis, the reduced reaction mechanism was summarized, which provided a promising method to generate representative reactions of the system from hundreds of species and reactions that occur in the combustion process. The proposed reduced reaction mechanism was applied to the CFD simulations, which created a fully coupled process between CFD and CRN. The results from the reduced reaction mechanism have shown good predictions compared with the probability density function method, which is a simplified way to model combustion. Pollutant emission such as NO_x has also been studied in both CFD and CRN models, in terms of the effects of fuel mixtures, the formation mechanisms and influential factors as well as reactions to the formation process. The work provides guidance for an integrated framework to model and study turbulence and chemical reactions for turbulent combustion systems.

ACKNOWLEDGMENTS

First, I would like to express my whole-hearted acknowledgment and gratitude to Dr. Francine Battaglia, for being my mentor and my role model with full of support, supervision and encouragement throughout my graduate study. I have been learning from her every moment in everyday through her profession, discipline, and passion in work, research and teaching. Her solid professional knowledge and great expertise have taught me the state-of-art in computational fluid dynamics during the past four years and now, I am honored and excited to join her in the next academic journey.

I would like to thank my committee members, Dr. Javid Bayandor, Dr. Brian Lattimer, Dr. Ayman Karim and Dr. Mark Paul for their insightful suggestions and supervisions during my graduate study.

I would like to thank Dr. Gerardo Flintsch, from Virginia Tech Transportation Institute (VTTI) and Dr. David Kibler for the great hydroplaning project that I can involve, get supervision and financial support.

I thank all my current and previous fellows in the Computational Research for Energy Systems and Transport (CREST) lab: Dr. David Park, Dr. Bahareh Estejab, Dr. Jeffrey Feaster, Dr. Jihong Wang and Dr. Wayne Soncini for supports and friendships.

I would like to acknowledge the Advanced Research Computing (ARC) center at Virginia Tech for High Performance Computing (HPC) resources and supports. Specifically, I would like to thank Alana, for having me involved in the Extreme Science and Engineering Discovery Environment (XSEDE) program.

Lastly, I would like to thank my parents for the unconditional love and support thousands miles away. My Ph.D. journey would not have begun without the inspiration and support from them. I appreciate their accompanying in each step of my growth and the encouragements to stand in front of difficulties. I would also thank all my supportive friends during good and bad times.

Contents

Lists of Figures	ix
Lists of Tables.....	xiii
Nomenclature.....	xiv
Chapter 1. Introduction	1
1.1. Background.....	1
1.2. Research objectives and approaches.....	4
1.3. Outline of the dissertation.....	5
Chapter 2. Literature review	7
2.1. Turbulence models of bluff-body flames.....	7
2.2. Inlet turbulence intensity levels and computational domains.....	9
2.3. Effects of fuel mixtures.....	11
2.4. Combustion models of bluff-body flames	14
2.5. Chemical reactor network.....	17
Chapter 3. Numerical methodology.....	22
3.1. Governing equations	22
3.2. Turbulence models.....	22
3.2.1. The RANS-based models.....	22
3.2.2. The standard $k-\varepsilon$ model	23
3.2.3. The RNG $k-\varepsilon$ model	24

3.2.4. The realizable $k-\varepsilon$ model	24
3.2.5. The reynolds stress model (RSM).....	25
3.2.6. The LES model	26
3.3. Combustion models	26
3.3.1. The non-premixed combustion model	26
3.3.2. Reduced chemical mechanisms: the eddy dissipation concept (EDC) model	30
3.4. Discretization schemes.....	31
Chapter 4. CFD modeling techniques development and optimization	34
4.1. Introduction.....	34
4.2. RANS vs. LES method	35
4.3. Grid resolution study.....	39
4.4. Comparative study of turbulence models	41
4.5. Effects of inlet turbulence intensity and computational domain	44
4.5.1. Inlet turbulence intensity.....	45
4.5.2. Effects of inlet turbulence intensity levels (no bluff-body)	46
4.6. Effects of the bluff-body addition.....	50
4.7. Conclusions.....	57
Chapter 5. Turbulent combustion application in the other bluff-body flame	59
5.1. Introduction.....	59
5.2. Experimental setup and uncertainty estimation	60

5.2.1. Uncertainty estimation method	60
5.2.2. Results of uncertainty estimate	64
5.3. CFD results for the Dally et al. flame	67
5.4. NO _x prediction	70
5.5. Effects of fuel mixtures on NO emission.....	73
5.6. Conclusions.....	79
Chapter 6. Chemical reactor network analysis for combustion systems modeling	81
6.1. Introduction.....	81
6.2. Reactor models in CRN approach.....	82
6.2.1. Perfectly stirred reactor (PSR)	83
6.2.2. Plug-flow reactor (PFR).....	84
6.2.3. Non-reactant mixer	84
6.3. CRN model for the non-premixed flames.....	85
6.4. CRN Results of temperature and species.....	89
6.4.1. CRN results of the Correa and Gulati flame.....	90
6.4.2. CRN results of the Dally et al. flame	91
6.5. Reactions of NO _x formation.....	92
6.6. Mechanism reduction based on sensitivity analysis of CRN.....	98
6.7. CFD performance of reduced reaction mechanisms	104
6.7.1. 3-step mechanism.....	104

6.7.2. 8-step mechanism.....	104
6.7.3. 9-step mechanism.....	105
6.7.4. Comparison between reduced mechanisms and PDF method	106
6.7.5. Comparison of computational time.....	110
6.8. Conclusions.....	111
Chapter 7. Conclusions and Future work.....	113
7.1. Summary	113
7.2. Significance and contribution	115
7.3. Future work.....	117
References.....	119

Lists of Figures

Figure 2.1 Schematic of bluff-body flame	7
Figure 3.1 Temperature profiles of PDF function and CFD results based on the non-premixed combustion models	30
Figure 4.1 Schematic of the bluff-body burner.....	35
Figure 4.2 Instantaneous images from 3D LES for temperature; black line is the location of the stoichiometric mixture fraction.....	37
Figure 4.3 Temperature comparison between the time and space averaged results of LES and RANS.....	38
Figure 4.4 Grid cells comparison for the (a) nonuniform rectilinear 75 (axial) \times 60 (radial), (b) nonuniform rectilinear 150 (axial) \times 120 (radial), (c) nonuniform rectilinear 300 (axial) \times 240 (radial) and (d) uniform 150 (axial) \times 120 (radial) cells.....	40
Figure 4.5 Radial profiles at $X/D_j = 10$ and 20 comparing grid resolutions: (a) mixture fraction; (b) temperature	41
Figure 4.6 Radial profiles at at $X/D_j = 20$: (a) temperature and mixture fraction profiles; (b) mass fraction profiles of CO, H ₂ and H ₂ O species	42
Figure 4.7 Temperature contours of CFD predictions of the Correa and Gulati flame: (a) temperature contours in full axisymmetric domain and (b) temperature contour with streamlines in enlarged scale.....	43
Figure 4.8 Schematic of bluff-body burner: (a) no bluff-body in the computational domain (NoBB); (b) bluff-body included in the computational domain (BB). The origin is at the centerline of the inlet for each domain.	45

Figure 4.9 (a) centerline profiles of mixture fraction; (b) radial profiles of mixture fraction and temperature at $X/D_j=20$	48
Figure 4.10 Centerline profiles for $I = 1$ and 4% (NoBB): (a) velocity magnitude; (b) strain rate	50
Figure 4.11 Mixture fraction profiles along the centerline comparing experiments [16] and 2D axisymmetric simulations without and with the bluff body	51
Figure 4.12 Radial profiles at $X/D_j = 10$ and 20 comparing experiments [16] and 2D axisymmetric simulations without and with the bluff body: (a) mixture fraction; (b) temperature	52
Figure 4.13 Axial velocity profiles at different axial locations within the bluff-body when $I = 1\%$	52
Figure 4.14 Axial positions for the profile shown in Figure 4.13.....	53
Figure 4.15 Turbulence intensity profiles at the end of the bluff-body	54
Figure 4.16 Comparison of mixture fraction (left) and temperature (right) when $I = 1\%$ and 4% for NoBB cases (upper) and BB cases (lower).....	55
Figure 5.1 Schematic of CFD simulation of bluff-body flame.....	59
Figure 5.2 Errors in the measurement of a variable x	62
Figure 5.3 Radial profiles of mean mixture fraction from experimental measurements and estimated uncertainty using (top) standard deviation, (middle) 95% confidence interval and (bottom) ASME guideline.....	65
Figure 5.4 Radial profiles of mean temperature from experimental measurements and estimated uncertainty using (top) standard deviation, (middle) 95% confidence interval and (bottom) ASME guideline.....	66

Figure 5.5 Instantaneous measurement data of temperature at $X/D_j=12.5$, $R=17.2$ mm with the uncertainties estimated using standard deviation (green line), 96% confidence interval (blue line) and ASME guideline (red line).....	67
Figure 5.6 Initial jet flow field measured by Masri et al. [18].....	68
Figure 5.7 Temperature contours of CFD predictions of the Dally et al. flame: (a) temperature contours in full axisymmetric domain and (b) temperature contour with streamlines in enlarged scale.....	69
Figure 5.8 Radial profiles of mixture fraction from experimental measurements and CFD results	70
Figure 5.9 Radial profiles of mean temperature from experimental measurements and estimated uncertainty using three different method	70
Figure 5.10 Scatter plots of NO from experimental database (black points: instantaneous value; red points: mean value) and solid profile of NO prediction from CFD model.....	73
Figure 5.11 Scatter plots of temperature from experimental database (black points: instantaneous value; red points: mean value) and solid profile of temperature prediction from CFD model.....	73
Figure 5.12 Radial profiles of mixture fraction, strain rate and radial velocity at $X/D_j = 20$	74
Figure 5.13 Profiles of temperature and NO mass fraction versus mixture fraction at $X/D_j = 20$	77
Figure 5.14 Radial profiles at $X/D_j = 20$: (a) temperature and NO mass fraction; (b) OH and CO mass fraction	78
Figure 6.1 Schematic of a bluff body burner and its zones network [156].....	82
Figure 6.2 Perfectly stirred reactor and its parameters	83
Figure 6.3 Plug-flow reactor and its parameters	84
Figure 6.4 Non-reactant mixer and its parameters	85

Figure 6.5 Temperature contours of CFD predictions of the Correa and Gulati flame; the upper half identifies key flame regions and the lower half shows the streamlines.....	86
Figure 6.6 Temperature contours of CFD predictions of the Dally et al. flame; the upper half identifies key flame regions and the lower half shows the streamlines	87
Figure 6.7 Schematic of the CRN model.....	89
Figure 6.8 Main products transportation and pollutants distribution for Correa burner.....	91
Figure 6.9 Main products transportation and pollutants distribution for Dally burner.....	92
Figure 6.10 CRN distribution and rate of production for Dally flame: (a) distribution of NO, N ₂ O and NO ₂ ; (b) total rate of production each species	93
Figure 6.11 Reactions with high ROP of NO in the region of RECIR., FLAME.2 and FLAME.4	95
Figure 6.12 Reactions with high ROP of NO ₂ (top figures) and N ₂ O (bottom) in the region of RECIR., FLAME.2 and FLAME.4.....	96
Figure 6.13 CRN distribution and rate of production for Correa and Gulati flame: (a) distribution of NO, N ₂ O and NO ₂ ; (b) total rate of production each species	97
Figure 6.14 Reactions with high ROP of NO in the region of FLAME.2 and FLAME.4.....	97
Figure 6.15 Reactions with high ROP of NO ₂ (left) and N ₂ O (right) in the region of FLAME.2 and FLAME.4.....	97
Figure 6.16 Temperature contour comparison with PDF method	107
Figure 6.17 Radial temperature profiles at X/D _j = 10 and X/D _j = 20.....	108
Figure 6.18 Radial profiles at X/D _j =20: (a) H ₂ mass fraction; (b) H ₂ O mass fraction	109
Figure 6.19 Temperature along the time scale of reactions	110
Figure 6.20 Comparison of computational time	111

Lists of Tables

Table 3.1 Overview of the tested turbulence models.....	23
Table 4.1 Summary of the relative errors and CPU time.....	56
Table 5.1 Experimental bluff-body flames studied in this paper.....	60
Table 5.2 Fuel-side operating conditions (volumetric analysis).....	74
Table 6.1 Volumetric inputs in the CRN models for Correa and Gulati and Dally et al. burners	89
Table 6.2 Temperature and main species at the exit of the bluff-body burners.....	90
Table 6.3 Sensitivity of H ₂ with respect to the rate coefficients.....	99
Table 6.4 Sensitivity of CO with respect to the rate coefficients	100
Table 6.5 Sensitivity of CO ₂ with respect to the rate coefficients	101
Table 6.6 Sensitivity of H ₂ O with respect to the rate coefficients.....	101
Table 6.7 Sensitivity of NO with respect to the rate coefficients	102
Table 6.8 Sensitivity of NO ₂ with respect to the rate coefficients.....	103
Table 6.9 Overview of the 3-step reduced mechanism.....	104
Table 6.10 Overview of the 8-step reduced mechanism.....	105
Table 6.11 Reduced reactions based on sensitivity analysis.....	105

Nomenclature

D	Diameter
E	Total Energy
f	Mixture fraction
G	Generation of turbulent kinetic energy
\bar{g}	Gravitational vector
H	Enthalpy
I	Turbulence intensity
k	Turbulence kinetic energy
k_{eff}	Effective conductivity
m	Mass
p	Pressure
R	Radial coordinate
r	Stoichiometric air-to-fuel mass ratio
S	Strain rate
T	Temperature
t	Turbulent
U	Uniform velocity magnitude
\vec{v}	Fluid velocity vector
X	Horizontal coordinate
Y	Mass fraction

Greek Letters

α	Prandtl number
----------	----------------

ε	Dissipation rate
κ	Reaction-rate coefficient
λ	Length scale
ρ	Fluid density
ϕ	Filter variable
Φ	Equivalence ratio
σ	Turbulent Prandtl number
τ	Residence time
τ	Fluid stress tensor
μ	Fluid viscosity
χ	Mole fraction

Sub/superscripts

b	Bluff-body
F	Fuel
i	Chemical element
j	Fuel jet
O	Oxidizer
st	Stoichiometric conditions

Chapter 1. Introduction

1.1. Background

Combustion has been widely used for about 1.5 million years by human, from cooking and heating, to transportation, power generation and other industrial applications. The control of fire became a turning point for human evolution and cultural advancements, which changes human life from the cold and dark into warm and bright. In the modern century, however, growing energy demands and increasing environmental concerns about pollution have motivated new and higher standards for combustion applications. Combustion is not just for providing heat and light but also for generating tremendous power for industrial needs that also meets the high environmental standards. Therefore, turbulent combustion research, as the most typical application of combustion in industry, from thermal energy and power generation to fundamental flame dynamics, mixing fuel burnout and pollutant formation has been extensively studied to improve the combustion processes and reduce environmental pollution [1, 2].

Two types of combustion flow patterns can be distinguished, depending on if the flow is laminar or turbulent. In laminar combustion, flame mixing has only molecular character, where molecules move from an area of higher concentration to an area of lower concentration. In contrast, turbulent combustion is characterized with large scale turbulent mixing and small scale molecular mixing [3]. In turbulent flames, convection mixes fuel and air macroscopically and then molecular mixing enables chemical reactions [3], which contributes to a larger heat generation because of the higher mixing intensity and flow velocities compared to laminar combustion [4]. Therefore, turbulent combustion processes have been implemented as the major way of energy generation to meet the extreme high demands on energy in both domestic and industrial applications [5-7]. On the other hand, experimental measurements become difficult due to the fast chemical reactions and

fluid flow. Hence, numerical prediction methods as well as theoretical studies of turbulent flames and turbulent combustion processes become essential and necessary.

Another issue related to combustion is the use of gaseous fuels as a source of energy. Recently, gaseous fuels have gained popularity and are widely used in power plants and gas turbines [8]. Besides the large reserves of natural gas, additional environmental advantage of gaseous fuels over other fossil fuels is the absence of sulfur dioxide (SO_2), a precursor to acid rain and particle emissions, such as particulate matter (PM) $\text{PM}_{2.5}$ or PM_{10} . $\text{PM}_{2.5}$ and PM_{10} represent fine particulates with diameters ranging from 2.5 to 10 μm [9]. These fine particles are difficult to filter or capture and can deposit in human lungs once inhaled, which therefore becomes a key factor of air quality measurement. One type of fuel, synthesis gas (or syngas), with primary fuel components of CO and H_2 , can be produced in an integrated gasification combined cycle (IGCC) system using a variety of fossil fuels [10]. The use of syngas not only avoids possible pollutant emissions (known to be produced in fossil fuel combustion), but also helps remove harmful pollutants in post-gasification processes. Therefore, syngas is expected to play an important role in future energy production with the growth of world environmental concerns [11, 12]. However, gaseous fuel is limited like other fossil fuels and some of the products can have negative impacts on the environment as well. For example, high temperatures associated with gas burners can lead to high levels of nitrogen oxide (NO_x) emissions, a family of air polluting chemical compounds. A recent Department of Energy (DOE) initiative aimed at reducing NO_x emissions from syngas combustion systems to less than 3 parts per million (ppm) provides motivation for fundamental research of gaseous fuel combustion and NO_x emissions from diffusion flames [10]. Therefore, the investigation of diluents application in syngas combustion and the effects on flame and emission characteristic become necessary. For example, CO_2 is a good candidate for diluent due to its

inevitability of production in combustion process. To satisfy the increasingly stringent emissions restrictions and attain economic benefits of high combustion efficiency, numerous studies about combustor designs and associated turbulent combustion problems have been conducted in academic and industrial fields [1, 2, 13-15]. There are several approaches to study turbulent combustion process, commonly experimental investigation and numerical analysis. Some burners are suitable for experimental study of the turbulence-chemistry interaction and are similar to practical combustors in industrial applications. A good example is the bluff-body flame with experimental work done by previous researchers [16-18]. However, under realistic circumstances, it will be rather challenging and time consuming for experimental study due to the complexity of the system. In addition to experimental testing of burners, significant progress has been made using computational fluid dynamics (CFD) to understand combustion process and assist the design of combustors over the last few decades [6, 19, 20]. Compared with experimental methods, CFD is more effective and costs less to investigate the effects of operating conditions on the turbulence-chemistry interactions. In addition, valuable information, such as flow patterns, pressure distribution, etc. can be provided throughout the entire flow domain, which can be very hard for experiments to conduct. CFD studies of industrial burners involve turbulent combustion, which is a complex problem that spans multiple length and time scales, and involves recirculating and swirling flows, fuel diffusion and mixing, oxidation of carbon/hydrocarbon fuels, and the formation and burnout of pollutants such as soot, carbon monoxide and nitrogen oxides [1, 21]. Resolving the important problems like turbulent flow, chemical kinetics, thermal radiation and pollutant formation coupled with complex geometry and boundary conditions are typical of CFD modeling issues [17]. Due to the involvement of multi-scale problems, the turbulence modeling techniques in previous studies are not very consistent [17, 22-25]. A comparative study of

turbulence models is necessary to conduct to ensure accurate predictive modeling methods that can be used in academia and industry with confidence on a robust basis.

Recently, studies on chemical reactions and mass transport have been conducted to improve the efficiency of combustion processes [19, 26, 27] and lower environmental pollution [28-31]. It is helpful to get critical relationships between chemical kinetics mechanisms and the complicated flow fields. These relationships provide a quick and useful way to evaluate the emission trends and the effects of parameters of interest using detailed chemical kinetic mechanisms. Since the combustion modelling methods in CFD mainly consist of the reduced chemical mechanism that allows limited amount of species in the transport equations and limited reactions, and the statistical method with the conserved mixing scalar representing fuel and air mixing, main reactions in the turbulent combustion system are either assumed or unknown. The unclear representative reactions obstacle understandings of the critical relationship between chemical kinetics mechanism and flow fields. An intelligently designed chemical reactor network (CRN) can provide critical relationships for the chemical mechanisms and flow paths in a complex reacting-flow system with full chemical mechanism. The developed CRN results with sensitivity analysis can provide insights of principal reaction mechanisms and answers regarding flame and emission characteristics across the combustor [32].

1.2. Research objectives and approaches

The main objective of this research is to conduct a thorough analysis and comparison of both turbulence models and chemistry representation methods in terms of accuracy, memory requirements, and computational costs as well as the effects of modeling assumptions on the long-time error accumulation. In addition, the goal of this research is to computationally model turbulent combustion to provide a better understanding of combustion processes and emissions in typical

non-premixed burners. Understandings of the interactions between turbulent flows and chemical reactions will be addressed using ANSYS Fluent 14.5 and CHEMKIN 17.0. A detailed study of the turbulent flow, the chemistry of combustion and their interconnections will be conducted by using CFD. A global understanding of flame formation, reaction paths as well as pollutant emissions will be studied based on a chemical reactor network (CRN) analysis. Whenever possible, predictions will be validated with experimental measurements. From a practical point of view, the experimental configuration used for validation purposes will be simple and well defined.

CFD simulations of turbulent combustion systems will be primarily conducted to obtain theoretical understandings of the effects of turbulence modeling methods, turbulence intensity levels and computational domains on the numerical predictions of a well-defined bluff body burner. More studies of the predictive capabilities of different chemical methods will also be conducted by comparing the performances of a statistical probability density function (PDF) model, the chemical reactor network (CRN) and the reduced chemical reactions mechanism created from the sensitivity analysis of CRN. The pollutant formation will be discussed in both CFD and CRN models and the optimization of fuel mixtures that can reduce the pollutant emissions will be suggested herein.

1.3. Outline of the dissertation

In Chapter 2, a broad literature review on turbulent combustion is presented. Chapter 3 describes the fundamental equations and numerical formulations implemented in CFD models. Chapter 4 presents the CFD study of a well-defined bluff-body flame, discussing the choice between the Reynolds-averaged Navier-Stokes (RANS) and the large eddy simulation (LES) approaches, and the RANS-based turbulence modeling methods. The effects of inlet turbulence intensity levels and computational domains are further discussed on the predictions of the same

bluff-body flame. Results are validated with the experimental measurements from Correa and Gulati [16]. Chapter 5 presents another bluff-body flame based on the CFD model established in previous chapters and compares the CFD results with the experimental work from Dally et al. [17]. The experimental uncertainty estimation has been analyzed and compared under different methods based on the available database of measurements. The NO_x formation and emission is studied based on Dally et al. flame and the effect of fuel mixtures on the NO_x emissions is also studied based on Correa and Gulati flame. Chapter 6 includes the study of chemical reactor network with the model built and validated based on previous studied bluff-body flames for a global picture of the flame constructions, reaction paths and predictions of exhaust emissions in the gaseous combustor systems. The study of rate of production of NO_x has been conducted to discover the formation and trend of NO_x and the contributing reactions. Sensitivity analysis has been conducted in the built network to generate the reduced chemical mechanism based on hundreds of species and reactions in the detailed chemical kinetics of gas phase reactions, GRI-Mech 3.0. A comparative study of reduced reaction mechanisms is conducted to compare the performance of the created reduced reaction mechanism with the PDF model in the bluff-body flames. Lastly, Chapter 7 summarizes and concludes the research presented in this dissertation, the significance and contribution, as well as possible future extensions to the current research.

Chapter 2. Literature review

2.1. Turbulence models of bluff-body flames

The bluff-body stabilized flame is a class of combustion where fuel and oxidizer enter separately into the combustor chamber, shown in Figure 2.1. It provides a wide range of industrial applications such as engines, boilers, furnaces, etc, where the diffusion and mixing become the key characteristics for the flame and combustion process [33]. It is also an ideal case to investigate the interactions between chemical reactions and turbulence and is a good bridge between theoretical problems and engineering applications [34]. However, bluff-body flames are still challenging for turbulent combustion modeling not only because of the complexity of turbulent flow but also the complexity of the finite-rate chemistry [34]. The interactions between turbulence and chemical reactions strongly affect the burning characteristics of the flames [23, 35]. In such cases, the use of a good turbulence model is crucial [29].

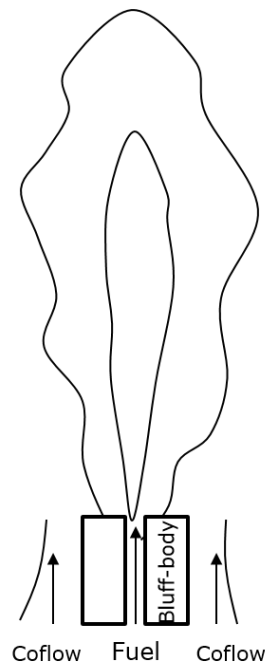


Figure 2.1 Schematic of bluff-body flame

The most accurate approach to simulate turbulent flows is the direct numerical simulation (DNS). The full Navier-Stokes equations are numerically solved with a very fine mesh to capture all the scales of eddies so the DNS method needs significant computational time, which can only be practically applied to low Reynolds number flows [22]. On the contrary, the Reynolds-averaged Navier-Stokes (RANS) approach has been the backbone in the industrial CFD applications and been widely studied by many researchers for the last few decades [17, 22, 23, 25]. Since the RANS approach only solves the averaged quantities and models the small scales fluctuating quantities, it requires relatively modest computing resource and time. Van Karim et al. [23] applied and compared the RANS-based turbulence models, namely the standard k- ϵ , realizable k- ϵ and the RNG k- ϵ turbulence models to the swirling flames in the Sydney burner. They determined that none of the models accurately predicted the central jet flow at the axis of symmetry, while in general, the realizable k- ϵ model yielded slightly better flow field predictions. Dally et al. [17] modified the constant $C_{1\epsilon}$ in the dissipation transport equation of the standard k- ϵ model and found that the modified k- ϵ model performed better than the Reynolds stress model (RSM) for the bluff-body flame. Frassoldati et al. [25] applied a comparative study between the RSM model, the standard k- ϵ and the modified k- ϵ with the coefficient $C_{1\epsilon}=1.6$ and found that the modified k- ϵ model succeeded in predicting the fuel jet fluid dynamics in a CH₄/H₂ moderate and intense low oxygen dilution (MILD) combustion burner. Nevertheless, the RANS approach sometimes is not sufficient when the transition dynamics of the turbulent flow becomes crucial. For some problems where the instantaneous results with the enormous range of scales must be resolved, the large eddies simulation (LES) method becomes more necessary and feasible, which can characterize turbulence flow by large and small eddies. Yilmaz et al. [24] compared the numerical results between large eddy simulations (LES) and the standard k- ϵ model using the probability density

function (PDF) approach with the flamelet model but without including the RSM model and found that the LES model gave better predictions. However, the computational mesh must be fine enough to resolve the smallest dynamical length-scale (the Kolmogorov micro-scale) to satisfy an accurate simulation [22]. In addition, unlike RANS, the grid cannot only be refined in the wall normal direction, but also must be refined to resolve turbulence in the wall parallel plane. It can only be achieved for flows at very low Reynolds number and on very small geometric scales that cannot be larger than 10-100 times the boundary layer thickness parallel to the wall. For this reason, using LES is only recommended for flows where wall boundary layers are not relevant and need not be resolved or for flows where the boundary layers are laminar due to the low Reynolds number.

Moreover, previous assessments of turbulence modeling techniques in non-premixed combustion are not very consistent [17, 22-25] and a comparative study of turbulence models will be necessary to conduct the study herein for the bluff-body syngas flames. The experimental data archives from the turbulent non-premixed flames (TNF) workshop [36] on bluff-body flames and swirl flames have been used by many researchers to test the performance and predictive capabilities of different turbulence models for numerical simulations [17, 23, 24, 37].

2.2. Inlet turbulence intensity levels and computational domains

Different modeling approaches have been used to study the effects of boundary conditions and computational domains on the simulation accuracy. For example, inlet turbulence intensity is one topic that has been considered by some researchers but overlooked by others in numerical studies [16, 17, 38-40]. The assumption of 2% turbulence intensity for co-flowing air was also adopted by Dally et al. [17]. Merci et al. [39] applied an inlet turbulence intensity of 1% to model the jets flow onto a plate. Mardani et al. [41] used a fuel turbulence intensity of 7% to yield the best agreement between the calculated and measured mixture fraction distribution, while the experimentally

estimated mean turbulence intensity was 4%. Gran et al. [38] argued that the value of turbulence in the fuel-jet has a substantial impact on the axial decay of mixture fraction and temperature, which did not support the conclusion of Correa and Gulati [16]. In fact, Correa and Gulati [16] stated that the flow was relatively insensitive to the inlet profiles and the variance of turbulence intensity made little difference since turbulence rapidly overwhelmed the inlet levels. Ligrani et al. [42] found that changes in the channel inlet turbulence intensity level affected conduction and convection in a channel flow with shallow dimples surfaces. However, most of the previous studies related to turbulence intensity were based on published recommendations and the effects of intensity were ignored in the combustion and turbulence characteristics [16, 17, 38-40].

The choice of a computational domain is also critical in modeling turbulent reacting flows. It has been generally acknowledged that quantitative differences may exist between computational domains, and most numerical studies have mainly focused on the differences between two-dimensional (2D) axisymmetric or planar geometries, and three-dimensional (3D) simulations [43-45]. Axisymmetric numerical simulations have been widely studied and reported in the literature for turbulent non-premixed combustion [16, 25, 29, 34, 39, 46-48]. It is also well known that axisymmetric simulations have advantages such as computational efficiency and simplification of the numerical treatment of angular derivative terms [49]. However, some researchers in the multiphase field like Reuge et al. [50] and Li et al. [44] have identified that the axisymmetric assumption was not commonly used in simulations of gas-particle flows due to the unphysical accumulation of particles along the axis in unsteady flow simulations. Significant differences in radial profiles of void fraction and bed expansion were also found between 2D axisymmetric and 3D calculations in a perfectly designed cylindrical fluidized bed [44]. So far, the reasons for the differences between 2D and 3D in the turbulent combustion field have not been generally accepted,

however, a factor that might explain the differences is selecting a reliable turbulence model to predict recirculating flows in a 2D axisymmetric domain [44, 45, 50-52]. Sundaram et al. [43] examined the recirculation zones in 2D axisymmetric and 3D domains and compared profiles along the centerline. They found that the magnitude of vorticity and the spreading rate from a 3D simulation were higher than the 2D axisymmetric case. Cammarara et al. [53] carried out both 2D and 3D simulations and suggested that 3D simulations are preferable for validating the CFD models with available correlations and experimental data.

Apart from the comparison between 2D axisymmetric and 3D geometries, the bluff-body was not physically modeled to save computational time and resources in most of the numerical investigations [16, 17, 40, 54, 55]. In addition, the majority of studies defined the inlet of the computational domain to start after the fluids passed the bluff-body to save computational time [16, 40, 55], however, the existence of the bluff-body can be crucial for better predictions. Several studies in wind tunnels have found that the shape and size of bluff-body significantly influenced vortex shedding [56-58]. Fan et al. [59] studied the effects of bluff body shapes, for cross-sections of an equilateral triangle and semicircle, on the blow-off limit in a planar micro-combustor. They found that the recirculation zones downstream of the bluff bodies had a very similar shape and size. However, the blow-off limit of the combustor and the radical OH distribution downstream of the combustion chamber was different in the two bluff-body burners. Therefore, the present work has been motivated to compare the differences and numerical accuracy of modeling the bluff-body inside and outside the computational domain.

2.3. Effects of fuel mixtures

Syngas mixtures can be a viable and alternative fuel due to the improved flame stability and performance, and the reduction of pollutant emissions [60]. Previous studies [30, 31, 61, 62] have

focused on the effects of hydrogen composition on the flame structure and emission characteristics of non-premixed flames. Choudhuri and Gullahali [30] studied the effect of a hydrogen-hydrocarbon composition in turbulent jet flames. They found that since elevation in hydrogen causes increasing combustion temperatures in CH₄/H₂ flames, NO_x was also found to increase. On the contrary, Naha et al. [61] investigated NO_x characteristics of methane/hydrogen and n-heptane/hydrogen blends in non-premixed and partial premixed flames. Results indicated that the addition of hydrogen can significantly reduce NO_x emission in n-heptane flames but has a negligible effect on NO_x emission in methane flames. Sanusi et al. [62] performed experiments to study the effects of hydrogen enrichment of methane fuels on the stability of a non-premixed combustor and found that NO_x emission increased due to increasing combustor temperatures. Hwang et al. [31] conducted an experimental study of hydrogen compositions for two fuel cases of H₂:N₂ = 1:1 and H₂:N₂ = 1:2. Unlike hydrocarbon flames, soot formation does not exist and local mixing does not have a significant effect on the temperature increase in the case of the H₂/N₂ flame.

Noting that hydrogen is often present in syngas mixtures, it is important to understand how the composition affects flame properties. Moreover, since syngas composition varies due to the fossil fuel source, gasification process, and post-gasification treatment and the type and amount of diluents present in the syngas mixture can vary significantly, the effects of diluent compositions need more attention as recommended by Giles et al. [12]. There are a few notable studies that address the diluents present in syngas. Rørtveit et al. [63] investigated diluents such as N₂, CO₂, and He on NO_x formation in H₂/N₂ counterflow flames and they found that CO₂ was the most effective, which significantly reduced the flame temperature. Zhang et al. [64] performed micro-mixing injection combustion experiments with CO₂ as the diluent in a hydrogen-rich syngas fuel,

which greatly reduced NO_x emissions and the wall temperature near the nozzle exit. Giles and Som [12] numerically investigated the airstream dilution effect on NO_x emission in syngas flame and learned that a strong dependency of steam addition on OH radical behavior affected NO emission behavior remarkably. The effects of H_2O and CO_2 on flame structure and NO for H_2/N_2 laminar diffusion flames were investigated by Kim et al. [65] and they found that adding H_2O is more superior to enhance effects of prompt NO than with adding CO_2 . Imteyaz and Habib [66] found that the reason temperature levels drop was due to the higher molar heat capacity of CO_2 compared with N_2 . The influence of additives (CH_4 , N_2 , CO_2 and steam) on a laminar flame of hydrogen in air was studied numerically by Azatyan et al. [67] and they found that methane caused the burning velocity to diminish approximately 5 times with increasing adiabatic flame temperature.

There has been an extensive body of literature dealing with the study of syngas mixtures on effective NO_x reduction [12, 30, 31, 61-67]. However, most of these studies focused on reducing NO emission at the penalty of a reduced flame temperature [30, 61-66]. It is crucial to maintain the flame temperature for flame stability and optimal combustion performance [68]. Hasegawa and Tanaka [69] stated that combustion using high temperature diluted air may improve flame properties such as stability, luminosity, and NO_x emission with lower heat release rate compared to ordinary flames. Therefore, numerical investigations can be efficiently used to characterize the detailed effects of syngas components and to find suitable syngas mixtures to both effectively reduce NO and maintain flame temperature [70]. Motivated by these considerations, the effects of hydrogen composition and nonflammable diluent mixtures on the combustion and NO emission characteristics will be examined and studied.

2.4. Combustion models of bluff-body flames

Besides the importance of turbulence model and boundary conditions, chemical kinetics in the turbulent-chemical interactions can be mainly studied through combustion model. Several combustion models have been developed and applied in CFD modeling of diffusion/non-premixed flames, which is mainly built up by two categories, namely the reduced chemical mechanism and mixture fraction statistical method [33]. In the reduced chemical mechanism, limited amount of species with reactions can be included and specified in the species transport equation. The different assumption and description of reaction rate classifies to different methods under reduced chemical mechanism, namely laminar finite-rate model, eddy-dissipation (ED) model [71] and eddy-dissipation-concept (EDC) model [72]. In laminar finite-rate model, the effect of turbulent fluctuations is ignored, which is usually not suitable for turbulent combustion. The ED model assumes that reaction rate are controlled by turbulence but for realistic, only one or two step chemical mechanism can be included [73]. The EDC model, on the other hand, includes detailed Arrhenius chemical kinetics with turbulent flow interaction, yet the computational calculation is expensive. The advantage of these models is that the detailed chemical mechanisms can be included to predict large amount of possible products and intermediates that may exist in all possible reactions. However, the disadvantage is that the dimension of the ODEs also increases accordingly as the number of chemical species increases [72]. Therefore, the more detailed chemical mechanisms included, the larger computational time needed. Reduced mechanism techniques of the full mechanisms may help to reduce the calculation efforts to an applicable/affordable scale, but still yield accurate predictions.

The other main combustion model is the mixture fraction statistical method, which is designed to model a conserved scalar mixture fraction to greatly simplify the reacting flow problem to a

mixing problem between fuel and air. In the mixture fraction statistical method, the chemistry calculations are performed using either the equilibrium model or the laminar flamelet model and the turbulence-chemistry interactions are modeled using the probability density function (PDF) [37]. The equilibrium model assumes the “fast” chemistry is invoked most often in the situations where fuel and oxidizer enter the combustion system in separate streams and the chemistry is sufficiently fast for all reactions to go to equilibrium as soon as the reactants are mixed [33]. When the chemical reaction is faster than diffusion, diffusion becomes rate controlling and the mixing scalar becomes very important. With the assumptions of equal diffusivity with unity Lewis number (ratio between Prandtl number and Schmidt number), all conserved scalars can be related to a single mixture fraction value [74]. A pre-assumed PDF-equilibrium look-up table can be constructed and used to determine different mean scalars (elemental mass fraction and enthalpy). To decouple the thermochemical scalars, the Burke-Schumann solution [75] for complete combustion is one type way to resolve the results of diffusion flame via a single step reaction of the form: fuel + oxidant \rightarrow products. In the fuel rich side where mixture fraction is larger than the stoichiometric mixture fraction ($f \geq f_{st}$), the mass fraction of oxidant is zero and the mass fraction of fuel is solely dependent on the function of mixture fraction. While in fuel lean region where $f \leq f_{st}$, the mass fraction of fuel is zero and the oxidant becomes a function of mixture fraction value. The calculations of thermochemical scalars are further developed by Kuo [76], Wamatz et al.[77] and S. B. Pope [78] and also adopted in the most CFD modeling, where the equilibrium composition and temperature of the flame are calculated as a function of mixture fraction based on the minimization of Gibbs free energy. The laminar flamelet model also used the concept of mixture fraction, however, an extra parameter as the mean scalar dissipation is also defined to quantify the non-equilibrium effects produced by the aerodynamic strain [37].

To reduce the computational time, many researchers [24, 25, 29, 34] studied the gas-phase diffusion flames by creating an assumed shape PDF table over the thermochemical variables under equilibrium assumptions. Jones et al. [79] have simulated the methane flames using the PDF-equilibrium method with good agreement with experimental data. Dally et al. [17] compared the performance of turbulence models with the PDF-equilibrium method and discussed the modification to the constants $C_{1\varepsilon}$ in the dissipation equations. Naha et al. [61] reported the effects of fuel mixtures on NO_x emissions in n-heptane flames and Azatyan et al. [67] studied the influence of additives on a laminar flame, both of which used the PDF-equilibrium method. Previous studies have shown that the need for high efficiency and accuracy of prediction is satisfied by using the PDF-equilibrium approach. However, the salient reactions that take place in the syngas burner remain unclear. With only a few major species included, the PDF-equilibrium method might give poor prediction on species distributions. Therefore, the EDC model applied with appropriate reduced mechanisms has been used and considered as an efficient and accurate way that is comparable to the PDF-equilibrium method but gives more precise solutions of species [46, 48, 72, 80]. Fukumoto and Oganmi [72] used the EDC model combined with chemical equilibrium to reduce the chemical mechanism and accelerate the simulation. Nagai and Takagi [81] obtained the equilibrium composition by minimizing the Gibbs free energy. Rogg and Williams [71] used the four-step reduced mechanism derived from methane in Peters et al. [82] and applied it to wet CO laminar premixed flames. Later Collins et al. [83] got the three-steps mechanisms by removing the methane consumption reactions from Rogg and Williams [71]. Collins et al. [83] also derived other reduced reaction mechanism based on a recently published mechanism [84], which has been optimized and validated against H_2/CO combustion data. Frassoldati et al. [85] used a 34-step kinetic model to comparatively study the EDC model and ED model. It turned out that the ED

model gave unsatisfactory prediction for both temperature and species mass fraction while the EDC model gave better agreement with measurements. Hossain et al. [40] conducted a very thorough analysis with combustion models of PDF-equilibrium, PDF-laminar flamelet and ED model for the diffusion flames, namely CO/H₂/N₂, H₂/CO and CH₄/H₂ flames. The results have shown that both PDF-equilibrium and the non-equilibrium flamelet model provided close with good prediction of temperature while the flamelet model had the best prediction of species results.

2.5. Chemical reactor network

Computational fluid dynamics (CFD) has become a powerful and integral tool in fluid mechanics that can numerically solve and analyze problems involving reacting systems [33, 86-88]. Over the last a few decades, significant progress has been made using CFD to understand combustion processes and assist the combustor designs. Using CFD to resolve turbulent reacting flows with complete chemical kinetic mechanisms can be onerous from a computational point of view. Recently, researchers have developed detailed reaction mechanisms for the oxidation of natural gas blends, containing more than two hundred species and more than a thousand reactions [89-91]. It will cost extremely large processing units for simulations as the calculation involves n-dimensional ordinary differential equations (ODEs) to be [92]. In addition, actual emission standards no longer allow ignoring a detailed kinetics analysis especially concerning NO_x and CO emissions in a combustor design [93]. Relatively small amounts of NO_x, a family of air polluting chemical compounds, have become one of the most important factors to evaluate the performance of combustors and engines. Therefore, detailed mechanisms toward a better understanding of turbulent combustion processes and emissions formation are essential for the continuing demands to reduce pollutant emissions. However, it is usually not accurate enough for NO_x investigation using most CFD tools such as Fluent, since the formation of NO_x is usually solved based on simple

chemical kinetic mechanism [94]. It is also not practical to include the complete gas reaction mechanisms that include hundreds of species and reactions in CFD modeling, since the computational time will be significantly required.

An intelligently designed chemical reactor network (CRN) model, which is defined to represent flow, mixing and reaction characteristics in the combustion process and predict pollutant emissions with detailed chemistry, can solve the problem. To speed up the time-consuming process and accurately predict, the CRN study provides a new perspective for computational modeling of turbulent combustion systems. It is also helpful to get critical relationships between chemical kinetics mechanisms and the complicated flow fields. These relationships provide a quick and useful way to evaluate the emission trends and the effects of parameters of interest. Generated from CFD results, the reactive flow field is split into a series of homogeneous zones as several small ideal reactors and a CRN is created by connecting ideal reactors with flow rates. Once connected, the network with elemental reactors can identify the flow, mixing and reaction characteristic with a detailed gas-phase reaction mechanism [95]. By decomposing a combustor into small reactors that are connected with feedback of species diffusion, it is possible to achieve more accurate predictions of NO_x using detailed reaction mechanisms with less computational time. It is also helpful to get critical relationships of chemical kinetics mechanisms with detailed reaction paths analysis and to explain the mechanism of flame and pollutants formation.

The concept of modeling the combustor by representing idealized reactor elements, such as perfectly stirred reactor (PSR), plug flow reactor (PFR) and non-reactant mixer (MIX) was firstly introduced by Bragg [96]. The networks are not necessarily limited to be composed by complicated reactor models and reaction paths. Some simple reactor models are found mostly useful in the network analysis of combustion systems. Rutar et al. [97] modeled the NO_x emissions of a jet

stirred reaction by using a simple two or three idealized reactor scheme. Similar investigations were also conducted by Schlegel et al. [98] and Feitelberg et al. [99], which provides efficient and useful results to evaluate the emission trends inside the burner with the detailed chemical kinetics mechanisms included. However, constructing such a reactor network is rather empirical and slight changes in combustor operating conditions often lead to a new reactor network configuration with a different number of reactors and connectivity.

Therefore, evaluating the structure of the flame with simplified kinetic schemes in CFD simulation first and then using CRN to post-process CFD results and implement detailed reaction mechanism have become a more useful procedure and been employed by many researchers [32, 100-103]. To numerically investigate and implement CRN theory, research has been conducted with different computational resources. A computer program designated as Combustion Reaction Equilibrium and Kinetics (CREK) has been developed by Wormech [104] and Pratt et al. [105, 106]. In CREK, the PSR is implemented by balancing the Arrhenius terms of net production of species by convection removal of that species from PSR control volume [32]. Nowadays, several similar-functional chemical reactor codes have become available, such as CHEMKIN, ASPEN, CHEMCAD, Pro/II. Codes like CHEMKIN show great ability to link the flow elements to a network yet are also able to handle the large chemical kinetic mechanisms. A complete chemical kinetics for syngas combustion model usually contains hundreds of species and reactions. Such a detailed chemical model is too big for many combustion simulations. In addition, the modeling methods of chemical reactions can strongly affect the turbulence-chemistry interactions results [107]. Therefore, efficient yet accurate numerical simulation of processes occurring in combustors such as fuel mixing, turbulent flow, ignition behavior and pollutant formation is challenging. To

effectively reduce the computational time without losing numerical accuracy, the reduced chemical kinetic reaction mechanisms is a practical way.

However, it is not easy to extract meaningful information and reactions since the chemistry of combustion process involves huge number of parameters from species and reactions. Noticeably, sensitivity analysis can be used for mechanism reduction that is, finding a smaller model that produces similar predictions for some of the variables (i.e., species concentration and temperature). Rabitz et al. [108] conducted a sensitivity analysis through the interpretation of sensitivity coefficients in reaction-diffusion system. Tomlin [109] compared several numerical methods for the calculation of local sensitivity and discussed sensitivity analysis as one of the mathematical tools applied in combustion chemistry. Turányi [110] analyzed and studied reaction kinetics problems using sensitivity method as one important tool. Turányi [111] also conducted the sensitivity analysis with different models and revealed chemical process of homogeneous hydrogen explosion and remixed hydrogen-air flame, using a new program package KINALC (an extension of CHEMKIN). Moreover, many researchers have further conducted their study of reduced reaction mechanism coupled with the CRN approach to reduce the computational burden. Novosselov [32] applied CRN approaches based on a CFD study with an eight-step global mechanism to analyze the effect of equivalence ratio on NO_x and CO emissions for a lean premixed gas turbine combustor. Russo et al. [93] efficiently assessed micro gas turbine emissions using a low computational effort CRN approach based on simplified CFD analysis with a kinetic scheme called “methane-air-2step”.

The main challenge in the work of reduced reaction mechanism is how to simplify the system and get the reduced mechanism and to what degree that a simplified mechanism can reasonably approximate the full mechanism. Based on the review of previous research and study, the reduced

reaction mechanism will be created based on the sensitivity analysis of CRN model and in CFD simulation, the reduced reactions will be applied in the EDC model and compared with the results from PDF method.

Chapter 3. Numerical methodology

3.1. Governing equations

To study the combustion, emission and mixing characteristics, flow field variables like velocity, temperature, mixture fraction, and species mass fraction have been solved using CFD. The software ANSYS Fluent [112] is employed to perform the simulations. The flow quantities are calculated using the Reynolds-Averaged Navier-Stokes (RANS) and energy transport equations. The continuity equation and conservation of momentum are:

$$\frac{\partial \rho}{\partial t} + \vec{\nabla} \cdot (\rho \vec{v}) = 0 \quad (3.1)$$

$$\frac{\partial}{\partial t} (\rho \vec{v}) + \vec{\nabla} \cdot (\rho \vec{v} \vec{v}) = -\vec{\nabla} p + \mu \vec{\nabla}^2 \vec{v} + \rho \vec{g} \quad (3.2)$$

where ρ is density, p is pressure, \vec{g} is the gravitational vector and μ is the dynamic viscosity of the fluid. The energy equation is given by:

$$\frac{\partial}{\partial t} (\rho E) + \vec{\nabla} \cdot [\vec{v} (\rho E + p)] = \vec{\nabla} \cdot k_{eff} \nabla T + \nabla \cdot (\vec{\tau}_{eff} \cdot \vec{v}) \quad (3.3)$$

where E is total energy, k_{eff} represents the effective conductivity and the second term on the right hand side is the viscous heating.

3.2. Turbulence models

3.2.1. The RANS-based models

Five RANS-based turbulence models are evaluated in the simulations of the non-premixed flame in the bluff-body burner. The two-equation turbulence models consist of a transport equation for the turbulent kinetic energy k and the dissipation rate ϵ . The aim is to determine the suitability of these models, and the five models are shown in Table 3.1.

Table 3.1 Overview of the tested turbulence models

Turbulent Models	Reference
The Standard k- ε model	Jones and Launer [113]
The Modified k- ε model	Christo and Dally [114]
The RNG k- ε model	Yakhot and Orszag [115]
The Realizable k- model	Shih et al. [116]
The RSM model	Gibson and Launder [117, 118]

3.2.2. The standard k- ε model

The standard k- ε turbulence model is valid only for fully turbulent flows and the effects of molecular viscosity are negligible. The k and ε are calculated from two additional transport equations:

$$\frac{\partial}{\partial t}(\rho k) + \bar{\nabla} \cdot (\rho k \bar{v}) = \bar{\nabla} \cdot \left[\left(\mu + \frac{\mu_t}{\sigma_k} \right) \bar{\nabla} k \right] + G_k + G_b - \rho \varepsilon \quad (3.4)$$

$$\frac{\partial}{\partial t}(\rho \varepsilon) + \bar{\nabla} \cdot (\rho \varepsilon \bar{v}) = \bar{\nabla} \cdot \left[\left(\mu + \frac{\mu_t}{\sigma_k} \right) \bar{\nabla} \varepsilon \right] + C_{1\varepsilon} \frac{\varepsilon}{k} (G_k + C_{3\varepsilon} G_b) - C_{2\varepsilon} \rho \frac{\varepsilon^2}{k} \quad (3.5)$$

where G_k and G_b represent the generation of turbulence kinetic energy due to the mean velocity gradients and buoyancy. σ_k and σ_ε are the turbulent Prandtl numbers for k and ε . For the model constants, the default values are used, i.e., $C_{1\varepsilon} = 1.44$, $C_{2\varepsilon} = 1.92$, $C_\mu = 0.09$, $\sigma_k = 1.0$ and $\sigma_\varepsilon = 1.3$. These default values have been determined from experiments for fundamental turbulent shear flows including homogeneous shear flows and decaying isotropic grid turbulence [113]. According to the results of Dally et al. [17], the modified standard k- ε model changes the $C_{1\varepsilon}$ coefficient in Eq. (3.5) from 1.44 to 1.60.

3.2.3. The RNG k - ε model

The “renormalization group” (RNG) k - ε model uses an effective viscosity to better represent low-Reynolds-number effects and near-wall effects. It is derived from the Navier-Stokes equations using a statistical technique, which results in some constants different from those in the standard k - ε model [23]. The RNG model has an additional term in the ε equation that improves the accuracy for rapidly strained flows. The RNG theory also provides an analytical formula for turbulent Prandtl numbers, while the standard k - ε model employs user-specified constant values. Equations (3.5) and (3.6) are modified through the viscosity terms on the right hand and R_ε is added to the dissipation rate equation to model rapidly strained flows:

$$\frac{\partial}{\partial t}(\rho k) + \bar{\nabla} \cdot (\rho k \bar{v}) = \bar{\nabla} \cdot (\alpha_k \mu_{eff} \bar{\nabla} k) + G_k + G_b - \rho \varepsilon - Y_M + S_k \quad (3.6)$$

$$\frac{\partial}{\partial t}(\rho \varepsilon) + \bar{\nabla} \cdot (\rho \varepsilon \bar{v}) = \bar{\nabla} \cdot (\alpha_\varepsilon \mu_{eff} \bar{\nabla} \varepsilon) + C_{1\varepsilon} \frac{\varepsilon}{k} (G_k + C_{3\varepsilon} G_b) - C_{2\varepsilon} \rho \frac{\varepsilon^2}{k} - R_\varepsilon \quad (3.7)$$

The inverse effective Prandtl numbers α_k and α_ε are calculated using the RNG theory. Constants are derived explicitly in the RNG model which is different from the standard method, i.e. $C_{1\varepsilon} = 1.42$, $C_{2\varepsilon} = 1.68$.

3.2.4. The realizable k - ε model

The realizable model satisfies certain mathematical constraints on the Reynolds-stresses, consistent with the physics of turbulent flow. The realizable k - ε model contains an alternative formulation for the turbulent viscosity. A modified transport equation for ε has been derived from an exact equation for the transport of the mean-square vorticity fluctuation. The transport equation for k is the same as the standard k - ε model. The realizable model improves the transport equation for ε in the following:

$$\frac{\partial}{\partial t}(\rho\varepsilon) + \bar{\nabla} \cdot (\rho\varepsilon\bar{v}) = \bar{\nabla} \cdot \left[\left(\mu + \frac{\mu_t}{\sigma_k} \right) \bar{\nabla} \varepsilon \right] + \rho C_1 S \varepsilon - \rho C_2 \frac{\varepsilon^2}{k + \sqrt{\nu \varepsilon}} + C_{1\varepsilon} \frac{\varepsilon}{k} C_{3\varepsilon} G_b \quad (3.8)$$

where S is the strain rate and ν is the kinematic viscosity. The model constants are summarized by Shih et al. [116] through experimental and numerical study, i.e., $C_{1\varepsilon} = 1.44$, $C_2 = 1.9$, $\sigma_k = 1.0$ and $\sigma_\varepsilon = 1.2$.

Both the realizable and RNG k - ε models have shown substantial improvements over the standard k - ε model where the flow features include strong streamline curvature, vortices and rotation. Initial studies have shown that the realizable model provides the best performance of all the k - ε model versions for several validations of separated flows and flows with complex features [23]. One weakness of the standard k - ε model and other “non-realizable” k - ε models are the modeled equation for the dissipation rate ε due to the lack of strain rate term and thus the prediction of the spreading rate for axisymmetric jets is unexpectedly poor for these models due to the modeled equation to represent dissipation rate [116].

3.2.5. The Reynolds stress model (RSM)

The RSM without the isotropic eddy-viscosity hypothesis closes the RANS equations by solving transport equations for the Reynolds stresses together with an equation for the dissipation rate, which means five additional transport equations are required in 2D flows. The equations will not be shown here but can be found in Gibson and Launder [117, 118].

Since the RSM accounts for the effects of streamline curvature, swirl, rotation, and rapid changes in strain rate in a more rigorous manner than the one-equation and two-equation models, it has greater potential to give accurate predictions for complex flows. However, RSM might not always yield results that are clearly superior to the simpler models in all classes of flows to warrant the additional computational expense.

3.2.6. The LES model

In contrast to the RANS methodology, the spatial filtering of the instantaneous equations employed in LES explicitly considers the three-dimensional, unsteady characteristics of turbulent motion [119]. The LES model characterizes turbulent flow by large and small eddies, where the size of the largest eddies needs to be comparable to the length of the mean flow and the size of the smallest eddies are responsible for the dissipation of turbulence kinetic energy. The LES model resolves only large eddies and modeled small eddies based on the filter function that can efficiently filters out eddies with small and large scales. The filter variable ϕ , such as pressure, energy or species concentration, can be defined by:

$$\bar{\phi}(x) = \frac{1}{V} \int \phi(x') dx', x' \in v \quad (3.9)$$

where V is the volume of a computational cell and is defined from the spatial filter function:

$$G(x, x') = \begin{cases} 1/V & x' \in v \\ 0 & x' \text{ otherwise} \end{cases} \quad (3.10)$$

3.3. Combustion models

3.3.1. The non-premixed combustion model

Under certain assumptions, the thermochemical state of a fluid can be described by a conserved scalar, known as the mixture fraction f , which is the elemental mass fraction that originated from the fuel stream. In terms of atomic mass fractions, this scalar can be written as:

$$f = \frac{Y_i - Y_{i,O}}{Y_{i,F} - Y_{i,O}} \quad (3.11)$$

where Y_i is the atomic mass fraction of an element i . The subscript O denotes the state of the oxidizer and the subscript F represents the state of the fuel. Mixture fraction simplifies the combustion to a mixing problem and describes the mixing between the fuel jet and the surrounding

oxidizer [25]. Possible reactants, products and intermediates have been specified in the model and are calculated mainly through the minimization of Gibbs free energy with the set of equations and algorithms from S.B. Pope [78].

With the use of the conserved scalar mixture fraction, the species equations are reduced to a single equation, whereby the summation of the species mixture fractions is 1. In this study, the equations for the Favre mean (density-averaged) mixture fraction \bar{f} and the variance of the mixture fraction $\overline{f'^2}$, respectively are [33]:

$$\frac{\partial}{\partial t}(\rho\bar{f}) + \nabla \cdot (\rho\bar{v}\bar{f}) = \nabla \cdot \left(\frac{\mu_t}{\sigma_t} \nabla \bar{f} \right) \quad (3.12)$$

$$\frac{\partial}{\partial t}(\rho\overline{f'^2}) + \nabla \cdot (\rho\bar{v}\overline{f'^2}) = \nabla \cdot \left(\frac{\mu_t}{\sigma_t} \nabla \overline{f'^2} \right) + C_g \mu_t (\nabla \bar{f})^2 - C_d \rho \frac{\varepsilon}{k} \overline{f'^2} \quad (3.13)$$

and $f' = f - \bar{f}$. The constants σ_t , C_g and C_d are the recommended value of 0.85, 2.86 and 2.0 from Jones and Whitelaw [33]. The mixture fraction variance describes turbulence-chemistry interactions, and using the assumption of chemical equilibrium, all thermochemical scalars (species fractions, density, and temperature) are uniquely related to the mixture fraction. For the low temperature region, where $T \leq 400$ K, mixture fraction value is either close to 0 or 1, indicating that the region has massive excess air or no air and the reactants barely react. For the average temperature value that is around 1000K, the assumption of equilibrium is valid because the characteristic Damköhler number (Da) as the ratio of flow time over reaction time is around 55 that is much larger than unity. It indicates that the time required to complete reaction is much shorter than the diffusion time in the turbulent flame and mixing is the controlling step in this problem[33]. A pre-assumed PDF look up table is constructed and used to determine different mean scalars, including species mass fraction and temperature, based on \bar{f} and $\overline{f'^2}$, and the total

enthalpy H [37]. With the non-premixed combustion model, the total enthalpy from the energy equation becomes:

$$\frac{\partial}{\partial t}(\rho H) + \vec{\nabla} \cdot [\rho \vec{v} H] = \vec{\nabla} \cdot \left(\frac{k_t}{c_p} \nabla H \right) + S_H \quad (3.14)$$

where the conduction and species diffusion terms are combined to give the first term on the right side, while the second term comes from the viscous dissipation. The total enthalpy H is defined as:

$$H = \sum_j Y_j H_j \quad (3.15)$$

where Y_j is the mass fraction of species j and H_j is the corresponding enthalpy as:

$$H_j = \int_{T_{ref,j}}^T c_{p,j} dT + h_j^0(T_{ref,j}) \quad (3.16)$$

An assumed shape probability density function table for the two thermochemical variables is created by a non-premixed combustion model and associated species. Using non-premixed combustion with the PDF approach, the thermochemical scalars like temperature and species mass fraction are related to mixture fraction. The PDF of f is written mathematically as [73]:

$$p(f) \Delta f = \lim_{T \rightarrow \infty} \frac{1}{T} \sum_i \tau_i \quad (3.17)$$

where T is the time scale and τ_i is the amount of time that f spends in the small range Δf . The function $p(f)$ is used to describe the instantaneous fluctuations of the mixture fraction in the turbulent flow. The mathematical function shown in Eq. (3.17) approximates the actual PDF shapes that have been observed experimentally [73]. The function $p(f)$ can also be used to compute averaged values of variables that depend on the mixture fraction. The species mass fractions and temperature are calculated using the relationship:

$$\overline{\Psi_i} = \int_0^1 p(f) \Psi_i(f) df \quad (3.18)$$

where Ψ_i represents the instantaneous values of mass fraction and temperature.

The volumetric analysis of the syngas fuel is 27.5% CO, 32.3% H₂ and 40.2% N₂, and is modeled to be consistent with the benchmark experiments of Correa and Gulati [16]. The syngas fuel has a relatively high stoichiometric mixture fraction ($f_{st} = 0.323$). The stoichiometric mixture fraction is the mixture fraction when chemical reactions occur at the stoichiometric ratio:

$$f_{st} = \frac{\Phi}{\Phi + r_{st}} \quad (3.19)$$

where r is the stoichiometric air-to-fuel mass ratio and Φ is the equivalence ratio, defined as the ratio of fuel-to-oxidizer mass ratio to the stoichiometric fuel-to-oxidizer mass ratio. Mathematically,

$$r_{st} = \left(\frac{m_O}{m_F} \right)_{st} \quad (3.20)$$

and

$$\Phi = \frac{m_F / m_O}{(m_F / m_O)_{st}} \quad (3.21)$$

where m is mass and the subscript st stands for stoichiometric conditions.

The zero-dimension mathematically predicted temperature profile along the mixture fraction f based on Eq. (3.18) is plotted to compare with the numerically calculated results of the 2D bluff-body flame by CFD non-premixed combustion models, as shown in Figure 3.1. The solid line shows the mathematical curve of the temperature profile along the mixture fraction, where temperature reaches the maximum value when $f = f_{st}$ for complete combustion. Scatter plots also show a similar trend of the temperature distribution along the mixture fraction, except that the maximum temperature is lower than the mathematical profile. Such a deviation of maximum values might be because of two factors. First, the mathematical function is too ideal and is different

from actual CFD results since dimensions of the actual burner are added. Second, modeling turbulence is not taken into account in a zero-order mathematical model.

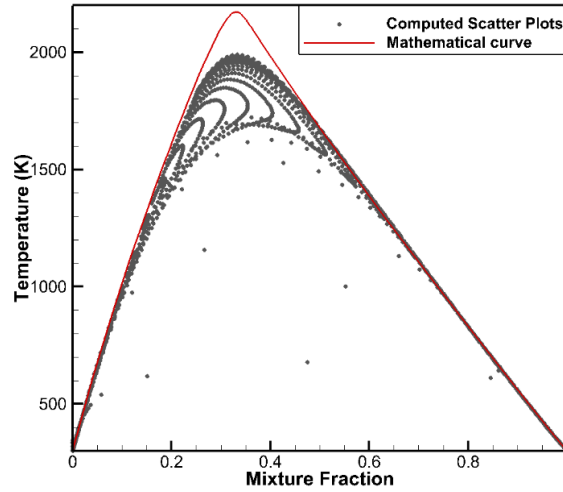


Figure 3.1 Temperature profiles of PDF function and CFD results based on the non-premixed combustion models

3.3.2. Reduced chemical mechanisms: the eddy dissipation concept (EDC) model

As a turbulence-chemistry interaction model, the EDC model can incorporate detailed chemical mechanisms into turbulent reacting flows [73]. The eddy dissipation concept (EDC) model assumes that combustion occurs in small structures called the fine scales of the turbulent flow, which is considered as a perfectly stirred reactor [92]. The fraction length of the fine scales ζ^* is modeled as:

$$\zeta^* = C_\zeta \left(\frac{\nu \mathcal{E}}{k^2} \right)^{1/4} \quad (3.22)$$

where C_ζ is volume fraction constant with the default value of 2.1337 [73].

In the EDC model, species are assumed to react in the fine structures over a fine time scale defined as:

$$\tau^* = C_\tau \left(\frac{\nu}{\varepsilon} \right)^{1/2} \quad (3.23)$$

where C_τ is a time scale constant equal to 0.4082 [73].

With the use of the EDC model, the conservation equation of chemical species has been changed with the source term S_i specified. The conservation equation of chemical species mass fraction is:

$$\frac{\partial}{\partial t}(\rho Y_i) + \nabla \cdot (\rho \bar{\nu} Y_i) = -\nabla \cdot \bar{J}_i + R_i \quad (3.24)$$

where J_i is the diffusion flux of species i , which arises due to the gradients of concentration and temperature. By default, ANSYS Fluent uses Fick's law (also called the dilute approximation) to model mass diffusion [73]. The term R_i is the net rate of production of species i and is modeled as:

$$R_i = \frac{\rho (\xi^*)^2}{\tau^* [1 - (\xi^*)^3]} (Y_i^* - Y_i) \quad (3.25)$$

where Y_i^* is the fine-scale species mass fraction after reacting over the time scale τ^* in the EDC model shown in Eq. (3.23).

The reaction-rate coefficient (κ) of each reaction step is prescribed in terms of the Arrhenius parameters:

$$\kappa = AT^b \exp\left(\frac{-E_A}{RT}\right) \quad (3.26)$$

where A is the pre-exponential factor, b is temperature exponent, E_A is activation energy and R is the gas constant.

3.4. Discretization schemes

The segregated pressure-based Navier-Stokes (PBNS) solver is used, which applies the projection method, where conservation of mass is rewritten in terms of pressure and pressure

becomes a primitive variable [120]. The PBNS solver is an effective way to solve incompressible flow, which is applicable for the flow in current study since local speed is subsonic with Mach number much less than 1 and the pressure change in the system is small. The semi-implicit method for pressure linked equations (SIMPLE) is applied for pressure-velocity coupling, where the momentum equations are solved with guessed pressure field p^* and p^* is used to solve the velocity field v^* . Correction terms are used to make the final velocity field satisfy continuity, which are implemented in the pressure and velocity fields as:

$$\bar{v} = \bar{v}^* + \bar{v}' \quad (3.27)$$

$$p = p^* + p' \quad (3.28)$$

where \bar{v}' and p' are correction terms. The relationship between the correction terms is expressed as:

$$\bar{v}' = -\frac{1}{A_p} \sum_l A_l \bar{v}' - \frac{1}{A_p} \nabla p' \Big|_p \quad (3.29)$$

where A_l and A_p are coefficients included in the momentum equations, and subscripts l and p represent velocity node and neighbor point in the discretized momentum equation. Combining the discretized continuity equation to corrected velocity Eq. (3.29) produces the pressure-correction equation:

$$\nabla \left[\frac{\rho}{A_p} \nabla p' \right] \Big|_p = [\nabla(\rho \bar{v}^*)]_p + [\nabla(\rho \bar{v}')]_p \quad (3.30)$$

The corrected pressure can be found using Eq. (3.30), which can be substituted into Eq. (3.29) to get the velocity field correction term. The velocity and pressure fields can be solved using Eq. (3.27) and (3.28) after the correction terms are found [121].

For the gradient and spatial discretization, least squares cell based (LSCB) and second-order upwind are exploited for diffusion terms, energy terms and mixture fraction terms. Second-order

upwind uses Taylor series expansions of the upstream cell centered-solution about the cell centroid to calculate the solutions at the faces of each cell. The convergence criteria for continuity, momentum and energy are that the normalized residuals reduce to 10^{-10} . For LES model, bounded second-order implicit is used for the transient formulation. The Courant-Friedriches-Levy (CFL) number can be expressed as:

$$CFL = \frac{U \Delta t}{\Delta x} \quad (3.31)$$

where U is the maximum fluid velocity and Δx represents the average-minimum cell size.

To include radiative heat transfer effects in a combustor, the P-1 radiation model is used, which is based on formulating radiation intensity into an orthogonal series expansion of spherical harmonics [122, 123]. It is further assumed that the radiation behaves as a gray body. The P-1 model has been found to provide good predictions in optically thick media, such as combustion gases [124], and further details can also be found in [125-127].

Chapter 4. CFD modeling techniques development and optimization

Majority of this chapter is produced from [70] and [128] with permission from Journal of Energy Resources Technology:

- Chen, L. and Battaglia, F., 2016, “The Effects of Fuel Mixtures in Nonpremixed Combustion for a Bluff-Body Flame” *Journal of Energy Resources Technology*, 138(2), p.022204.
- Chen, L. and Battaglia, F., 2017, “The Effects of Inlet Turbulence Intensity and Computational Domain on a Nonpremixed Bluff-Body Flame,” *Journal of Energy Resources Technology*, 139(2), p. 022205.

4.1. Introduction

The objective of the current study is to examine the effects of turbulence models and the operating conditions on the non-premixed turbulent combustion characteristics and simulation accuracy. Previous numerical works on modeling the bluff-body flames were introduced in section 2.1. It is worth noting that a comparative study of turbulence models is necessary to conduct since the turbulence modeling techniques in previous studies of non-premixed combustion are not consistent [17, 22-25].

The 2D schematic of the bluff-body flame is shown in Figure 4.1, where the bluff body burner has an outer diameter $D_B = 38.1$ mm with a concentric fuel jet diameter $D_j = 3.18$ mm. A non-premixed turbulent jet flame composed of 27.5% CO/32.3% H₂/40.2% N₂ syngas mixture was analyzed in the experiment of Correa and Gulati [16]. The fuel and air streams enter through the burner at the left side of the domain with uniform velocities using the experimental conditions [16] and atmospheric pressure is specified at the exit (right side of domain). The fuel and air jet velocities are 80.0 m/s and 6.5 m/s, respectively. Temperature is 300 K for both fuel and air streams.

The mixture fraction based on Eq. (3.11) is 1 for the fuel inlet and 0 for air inlet. Standard wall functions and no-slip boundary conditions are applied at the surfaces of the bluff body and walls, and the surfaces are assumed adiabatic. The domain numerically modeled is shown as the shaded region in Figure 4.1. The centerline about the X-axis is specified as an axisymmetric boundary. A detailed description of the experimental technique employed for the measurement of temperature and species concentrations by a laser Raman scattering system has been reported in Correa and Gulati [16]. In this chapter, a comparative study between RANS and LES methods, five RANS-based turbulence models will be conducted and evaluated with the experiments of Correa and Gulati [16], who measured the major species of the non-premixed flame of 27.5%CO/32.3% H_2 /40.2% N_2 and air.

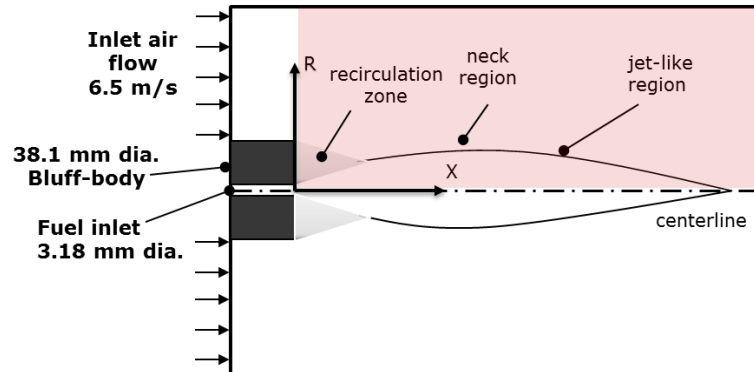


Figure 4.1 Schematic of the bluff-body burner

4.2. RANS vs. LES method

To begin, a comparative study between the RANS and LES approach has been conducted since computational cost is considered as one of the primary problems. The computational cost involved with the LES method is normally orders of magnitudes higher than the steady RANS calculations in terms of memory (RAM) and CPU time. Based on the performance of these methods and the

major focus of the bluff body flame study, this section will be used to determine which approach would be better and can be employed in the following study.

Compared with the RANS approach, one major advantage of the LES method is that the instantaneous nature of fluctuations with the enormous range of scales can be resolved. Therefore, the detailed transition behavior of the turbulent flame can be captured by using the LES model. Figure 4.2 shows the computed instantaneous temperature fields at different times, which demonstrates the propagation of this diffusion flame, and the time-dependent nature of the flame and LES calculation. In Figure 4.2, the solid line corresponds to the location of the stoichiometric mixture fraction, which denotes where the chemical reactions occur at the stoichiometric ratio of $f_{st}=0.323$, corresponding to a quasi-equilibrium of the flame with the turbulence. On the stoichiometric surface, temperature reaches a much higher value than other flame regions. From the recirculation zone to the neck zone, higher temperatures occur on the fuel-rich side of the stoichiometric surface while the jet-like region (downstream) shows higher temperatures on the fuel-lean side of the stoichiometric surface due to more entrainment of air into the flame zone.

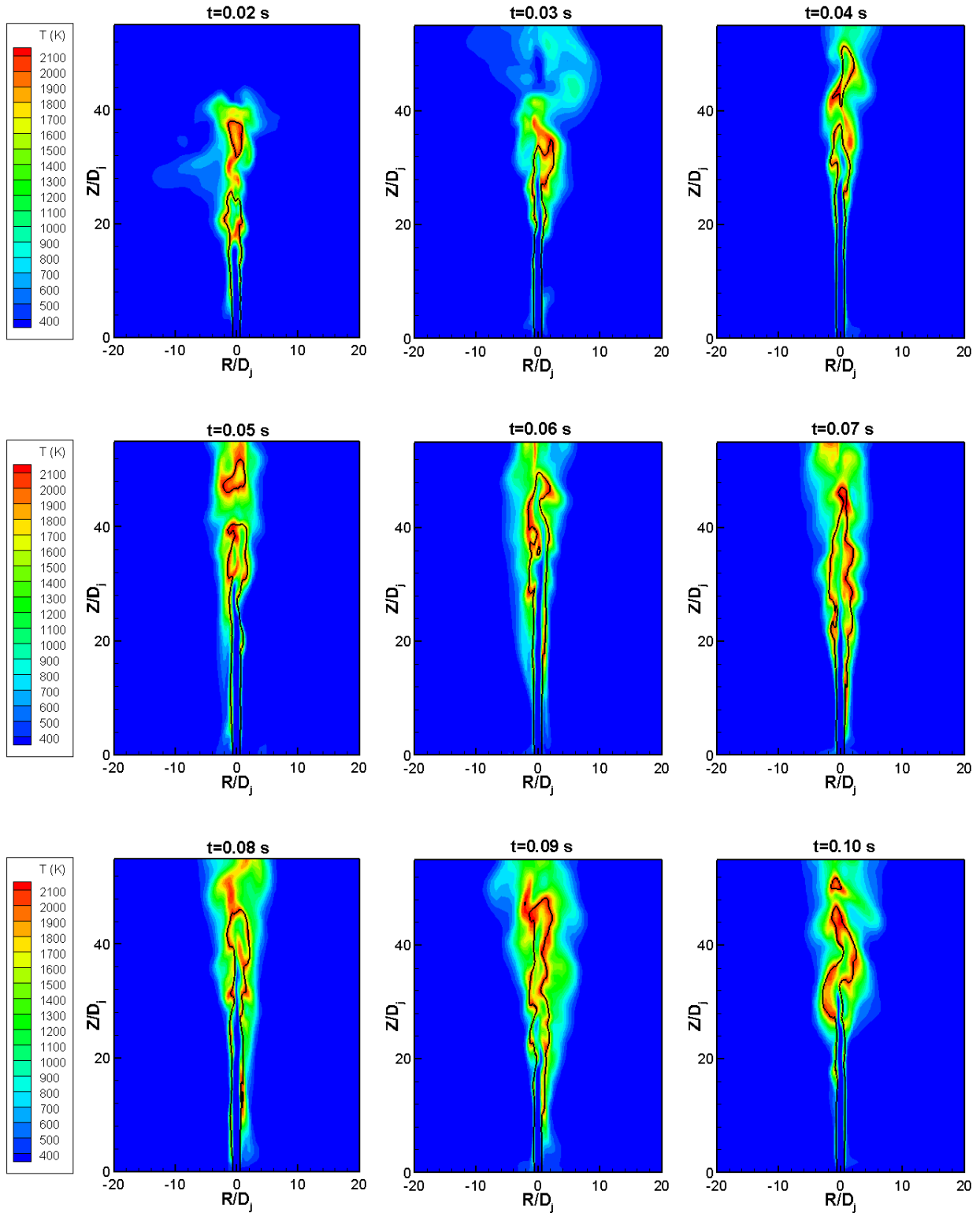


Figure 4.2 Instantaneous images from 3D LES for temperature; black line is the location of the stoichiometric mixture fraction

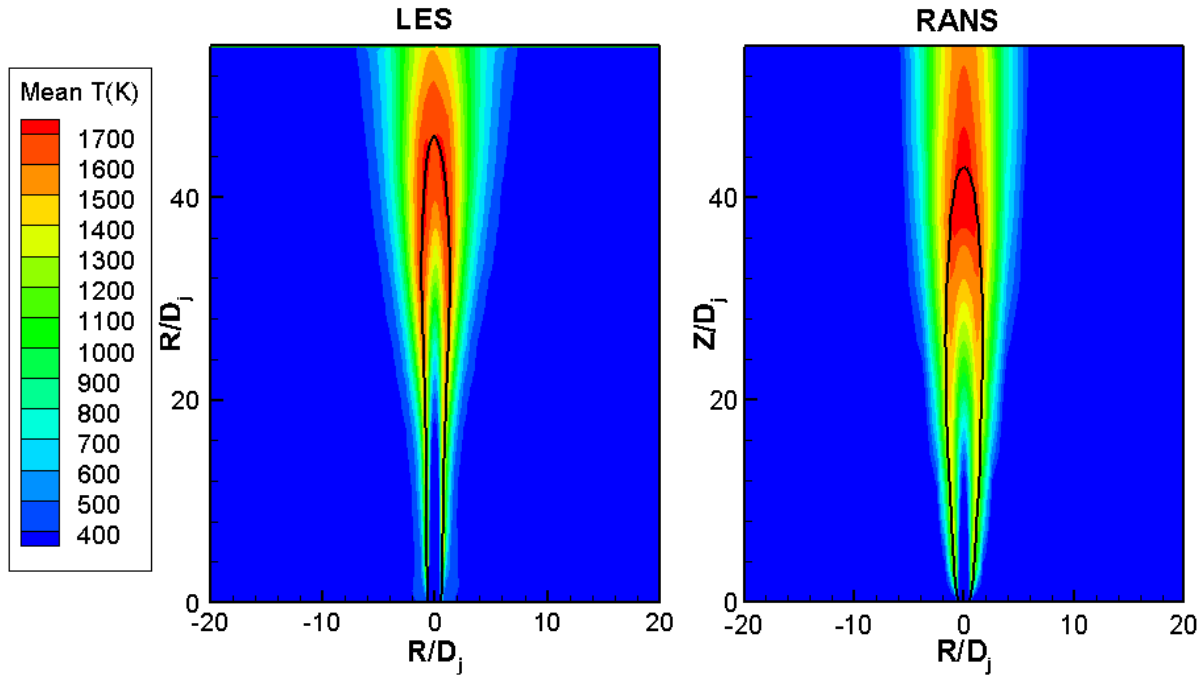


Figure 4.3 Temperature comparison between the time and space averaged results of LES and RANS

Since the experimental results are provided with mean values by Correa and Gulati [36], the LES results are time and space-averaged and compared with the RANS results. The averaging in time and space gives the temperature results of the LES and the RANS methods in Figure 4.3. Solid line corresponds to the location where the mean mixture fraction value equals to the stoichiometric mixture. The averaged LES results reveal very smooth temperature contours and a smooth profile of mean mixture fraction. Comparing the instantaneous temperatures in Figure 4.2 and the averaged temperatures from the LES results in Figure 4.3, the instantaneous temperatures show a wide scale and some entrainment of fresh air into the flame zone. In Figure 4.3, the average temperatures from the LES model are very close to the temperatures from the RANS method. The similarity of the temperature fields in Figure 4.3 indicates that the problem can reach a quasi-steady mode, and there are no more reasons to distrust the RANS model, since there is insufficient impact from instantaneous results to the mean flow. Taking into account that the LES model needs

computational time orders of magnitudes longer than the RANS method, and that the RANS approach can capture the mean flow features fairly well, the RANS approach is considered more appropriate in the following study.

In the RANS temperature field, similar to the LES, a solid line was added at the location of stoichiometric mixture fraction, shown in Figure 4.3. Based on the averaged results of LES and RANS in Figure 4.3, both temperature and the stoichiometric mixture profile are perfectly symmetric to the centerline of the flame, which indicates that this problem can be simply solved using an axisymmetric model rather than the full 3D model. Therefore, an axisymmetric model based on the RANS method is adopted and employed in the following study.

4.3. Grid resolution study

A grid resolution study is conducted, including 3 non-uniform but rectilinear meshes: 75 (axial) \times 60 (radial), 150 (axial) \times 120 (radial), 300 (axial) \times 240 (radial) and one uniform mesh with 150 (axial) \times 120 (radial) cells, shown in Figure 4.4. The realizable k- ϵ model was used for the grid resolution study. In the axial and radial coordinate directions, the mesh spacing grows according to a geometric progression with a modest expansion ratio (3% in X-direction, 5% in R-direction). The grid lines are concentrated in the high shear region downstream of the bluff body.

Figure 4.5 compares CFD results of the 4 grid resolutions with the experimental data at $X/D_j=10$ (left sides in the figures) and $X/D_j=20$ (right sides). From Figure 4.5 (a), the predicted results of the radial mixture fraction distributions varied little among the different grid resolutions. Figure 4.5 (b) shows the radial temperature profiles at $X/D_j=10$ and 20. Again, it is noted that the variations in the temperature distributions using different meshing schemes are very small. Therefore, it can be concluded that the spatial discretization error is small enough to allow the underlying mathematical models to be evaluated.

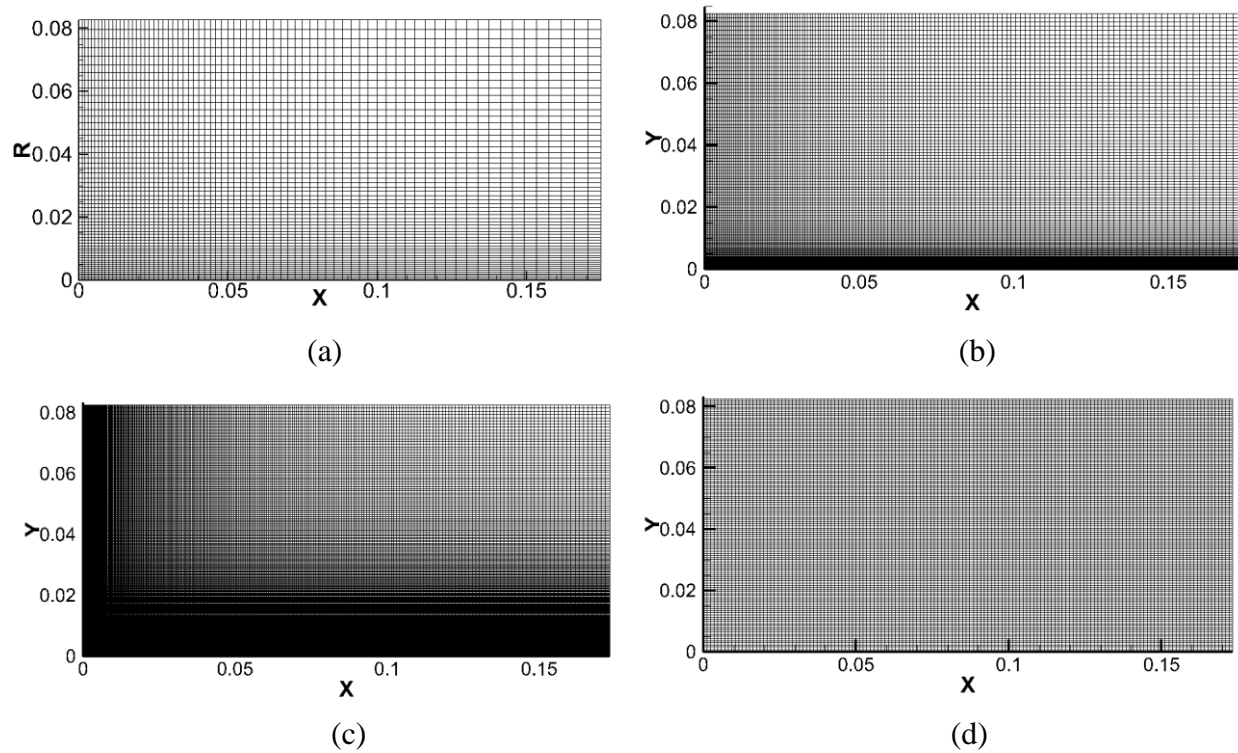


Figure 4.4 Grid cells comparison for the (a) nonuniform rectilinear 75 (axial) \times 60 (radial), (b) nonuniform rectilinear 150 (axial) \times 120 (radial), (c) nonuniform rectilinear 300 (axial) \times 240 (radial) and (d) uniform 150 (axial) \times 120 (radial) cells

The numerical uncertainty due to discretization is estimated by analyzing the grid convergence index (GCI) [129]. The GCI values of the predicted mixture fraction are 3.1% and 2.7% for coarse-medium and medium-fine grids, respectively. From the comparison of grid resolutions, it is obvious that the geometry of the bluff body flame can be sufficiently resolved with the non-uniform rectilinear 75 (axial) \times 60 (radial) mesh to predict the mixture fraction and temperature accurately. To save computational expense, the non-uniform 75 \times 60 mesh is used for the remainder of the study.

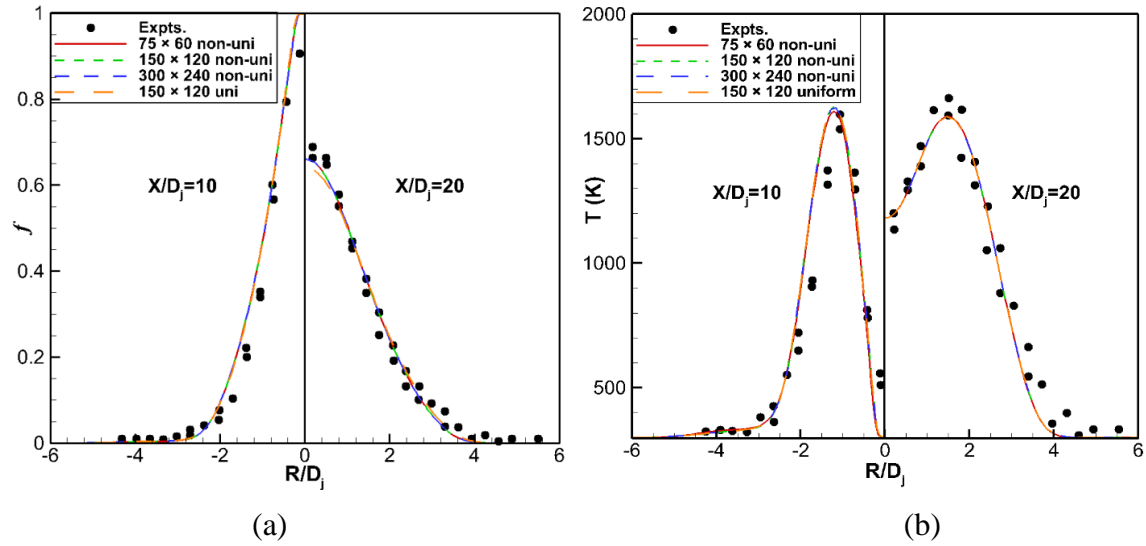


Figure 4.5 Radial profiles at $X/D_j = 10$ and 20 comparing grid resolutions: (a) mixture fraction; (b) temperature

4.4. Comparative study of turbulence models

Figure 4.6 (a) shows the radial mixture fraction profiles (left axis) and radial temperature profiles (right axis) at $X/D_j = 20$. Experimental results are shown as triangles (mixture fraction) and squares (temperature) in Figure 4.6 (a). The realizable $k-\epsilon$ model and RSM model have similar radial temperature and mixture fraction profiles, shown as dash dot and short dash lines. They also follow the distributions of the experimental temperature and mixture fraction quite well along the radial distance. The standard $k-\epsilon$ and the RNG $k-\epsilon$ model also share similar radial profiles, however, the two models do not show good agreements with the experiments, where $R/D_j \leq 1.5$. As mentioned previously, the RNG $k-\epsilon$ model improves the standard $k-\epsilon$ in terms of low Reynolds number flows. However, for the high Reynolds number flow presented in Figure 4.6, the profiles from the RNG $k-\epsilon$ model verify that the model is not appropriate. The RNG $k-\epsilon$ model cannot predict the flame characteristics well, especially near the burner inlet. The same situation happens

for the modified $k-\epsilon$ model. This is consistent with the content mentioned above that “non-realizable” $k-\epsilon$ models have weaknesses when predicting axisymmetric jet flows [116].

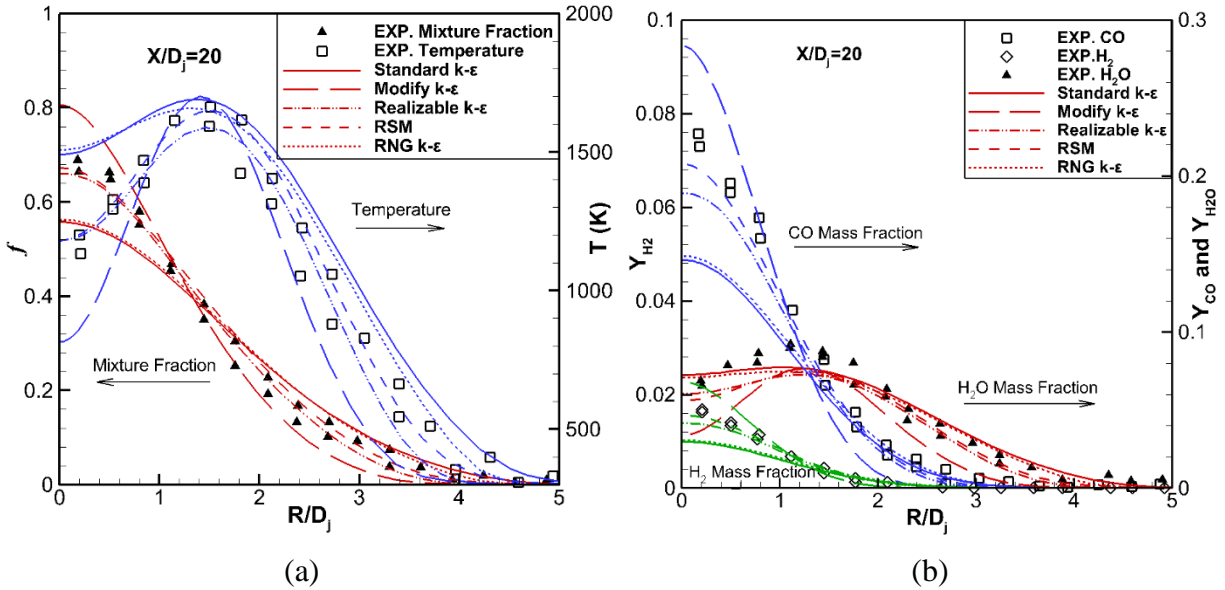
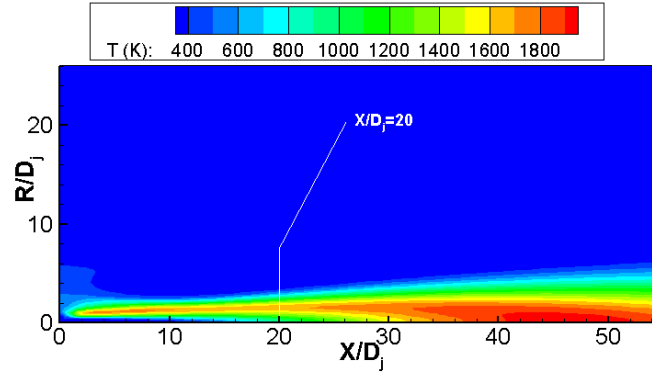
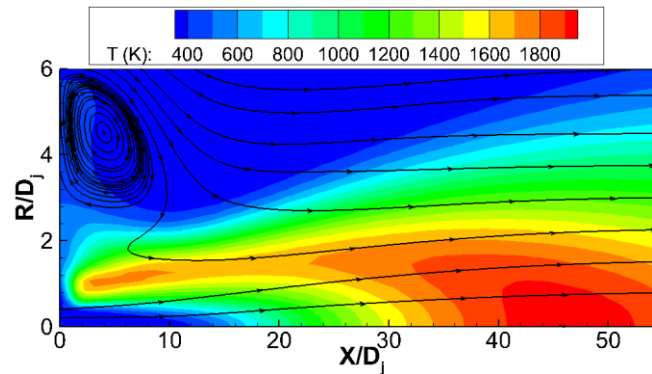


Figure 4.6 Radial profiles at at $X/D_j = 20$: (a) temperature and mixture fraction profiles; (b) mass fraction profiles of CO, H_2 and H_2O species

Figure 4.6 (b) shows the radial mass fraction profiles of CO, H_2 and H_2O at $X/D_j = 20$. Similar to the results shown in Figure 4.6 (a), the RSM model and realizable $k-\epsilon$ model have similar radial species mass fraction distributions and also have good agreement with experimental data. Although the standard and RNG $k-\epsilon$ models are similar in the radial mass fraction profiles, they under-predict the flame species distributions. In addition, Figure 4.6 (b) shows that the H_2 mass fraction is much lower than the CO mass fraction, while the original composition of syngas at the fuel-side inlet is 32.3% H_2 /27.5%CO/40.2% N_2 . One reason is that hydrogen has relatively low molecular weight; the other reason is that the lower flammability limit (LFL) of H_2 is much lower than CO, which produces hydrogen in the bluff-body burner and is oxidized quickly by air.



(a)



(b)

Figure 4.7 Temperature contours of CFD predictions of the Correa and Gulati flame: (a) temperature contours in full axisymmetric domain and (b) temperature contour with streamlines in enlarged scale

For the comparative study of turbulence models with results shown in Figure 4.6, the realizable $k-\epsilon$ and the RSM models are suitable for non-premixed syngas flames. Contours of temperature in full axisymmetric domain and the enlarged view with streamlines are shown in Figure 4.7 (a) and (b). The contour with streamlines calculated using the realizable $k-\epsilon$ model reveal the complex nature of the non-premixed syngas flame in Figure 4.7 (b). The flame structure in the burner is non-dimensionalized to the fuel jet diameter D_j . The region shown in Figure 4.7 (b) is scaled and only shown portion of the burner to 6 times D_j in the radial direction, to focus on the flow close to the bluff body. The streamlines show the recirculation zone behind the bluff-body wall. Since the realizable $k-\epsilon$ and RSM models account for the effects of streamline curvature, swirl, rotation, and

rapid changes in strain rate, they have shown good predictive capabilities for the flame characteristics. The realizable k - ϵ model will be used in all remaining simulations to study the effects of hydrogen and diluents, in order to avoid the additional computational expense of the Reynolds stress model [25], and to concentrate on the study of turbulence–chemistry interactions.

4.5. Effects of inlet turbulence intensity and computational domain

In the current study, numerical investigations will show the effects of inlet turbulence intensity levels and computational domains (2D axisymmetric or full 3D domain; with or without the bluff-body) on the non-premixed turbulent combustion characteristics and simulation accuracy. This work will demonstrate the importance of accurately modeling the inlet boundary and the influence of the computational domain for predicting the non-premixed bluff-body flame, which has been debated in previous studies [16, 17, 40, 54, 55]. Based on the validation work, further insight into the effects of inlet turbulence intensity and computational domains and the appropriate modeling of the boundary condition will be evaluated and provided.

Numerical simulations of the flow, mixing and temperature fields are compared and validated with experiments of Correa and Gulati [16] for a non-premixed flame. A schematic of the burner that includes and excludes the bluff-body is shown in Figure 4.8. The domain size immediately downstream of the bluff body has a length L of 174.9 mm and radius R_o of 75 mm. The bluff-body has a diameter $D_b = 38.1$ mm and length $L_b = 115.5$ mm with a volumetric blockage ratio of 5% [16], and separates the fuel and air streams before they enter the burner so the two streams react and mix at the same location. Syngas fuel of 27.5% CO, 32.3% H₂ and 40.2% N₂ enters the system through the central jet of diameter $D_j = 3.18$ mm with an average velocity of 80 m/s. The air stream enters as a co-annular flow with an average velocity of 6.5 m/s [16]. There are some uncertainties in the specification of inlet condition as experimental inlet data are not available. However uniform

velocities are specified for the fuel and air streams based on the experimental conditions and numerical work from Correa and Gulati [16], and will be further discussed in Section 4.6. The remaining boundary conditions are the same as described in Section 4.1.

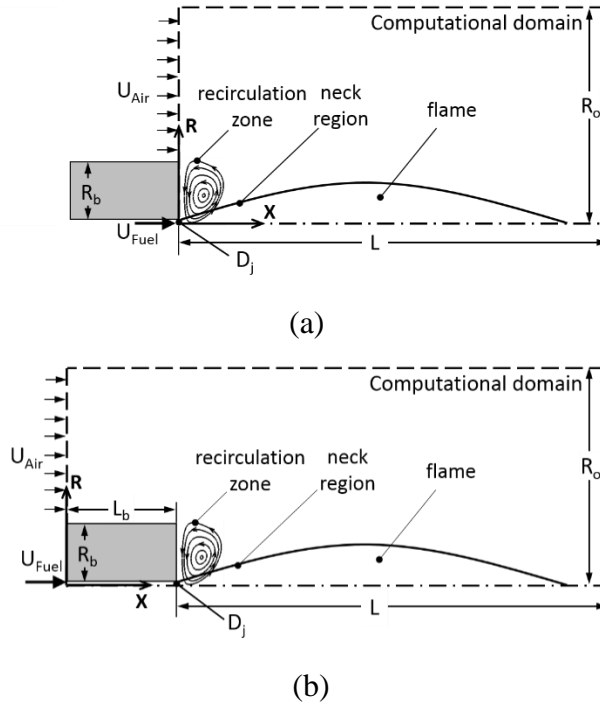


Figure 4.8 Schematic of bluff-body burner: (a) no bluff-body in the computational domain (NoBB); (b) bluff-body included in the computational domain (BB). The origin is at the centerline of the inlet for each domain.

4.5.1. Inlet turbulence intensity

It is important to define the transported turbulence quantities to accurately represent the boundary profile and the development of the flow at the inlet from experimental data or empirical formulas. The inlet turbulence parameters are specified using:

$$k_{in,F} = \frac{3}{2} (IU_{in,F})^2 \quad (4.1)$$

$$\varepsilon_{in,F} = \frac{C_\mu^{3/4} k_{in,F}^{3/2}}{\lambda D_{H,F}} \quad (4.2)$$

where $U_{in,F}$ is the fuel inlet velocity. The length scale $\lambda D_{H,F}$ is prescribed as $0.07D_{H,F}$, where $D_{H,F}$ is the hydraulic diameter of the fuel inlet, equal to D_j . The empirical constant C_μ specified in the turbulence model is 0.09 based on recommendations [55]. Different from previous studies of boundary conditions [16, 17, 40, 41], in the present work, the turbulence intensity at the inlet is estimated using the empirical correlation for channel flows developed by Durst et al. [130], which is valid for Reynolds numbers ranging from 3000 to 13800. The turbulence intensity is:

$$I = \frac{u'}{U} = 0.13 \left(\text{Re}_{D_{H,F}} \right)^{-1/8} \quad (4.3)$$

where u' is the root-mean-square of the axial velocity fluctuation and U is the mean axial velocity along the radial direction. In the present study, $I = 4\%$ is calculated based on a Reynolds number $\text{Re} = 12,846$, using $U_{in,F}$ and the mixture properties of the syngas mixture. Simulations can be sensitive to $k_{in,F}$ and $\varepsilon_{in,F}$ and subsequently influence the accuracy of the predictions. The inlet turbulence intensity of $I = 4\%$ is compared to $I = 1\%$ that was assumed by Hossain [40]. Four cases including both 2D axisymmetric and 3D simulations for $I = 1\%$ and 4% are investigated to test the effects of inlet turbulence intensity when the bluff-body is not included in the computational domain. Additional cases for the axisymmetric domain are tested with $I = 1\%$ and 4% to examine the effects when the bluff-body is included in the domain.

4.5.2. Effects of inlet turbulence intensity levels (no bluff-body)

The non-premixed bluff-body burner was modeled using the modified standard k- ε turbulence model. The standard k- ε model is known for its shortcomings of over-predictions of the decay rate and the spreading rate of round jets [25]. The modified standard k- ε turbulence model is improved by changing the constant coefficient $C_{1\varepsilon}$ suggested by Christo and Dally [114] and the turbulence intensity level in this study to simulate the flow, mixing and temperature distributions of the flame. Four cases including both 2D axisymmetric and 3D simulations with numerical parameter of

turbulence intensity I of 1% and 4% are investigated here to assess the effects of inlet turbulence intensity when the bluff-body is not included in the computational domain.

Figure 4.9 (a) shows the mixture fraction profiles along the centerline of the 4 cases simulated and the experimental results of Correa and Gulati [16]. The 2D axisymmetric and 3D domains are shown as blue and red lines of different styles, respectively, and experimental results are shown as symbols [16]. In Figure 4.9 (a), the 3D simulation with $I = 4\%$ shows the best agreement with the experiments and the 2D axisymmetric simulation overpredicts the mixture fraction at the centerline. This observation is consistent with Shih et al. [116] who reported that the prediction of axisymmetric jets was relatively poor compared to 3D jets for the $k-\varepsilon$ turbulence model due to the underestimation of dissipation. Comparing the mixture fraction profiles for the 2D axisymmetric and 3D simulations with $I = 1\%$, the mixture fraction does not decay until the axial distance exceeds $X/D_j = 15$, which significantly deviates from the experiments. Changing the turbulence intensity from 1% to 4% greatly improves the mixture fraction predictions for both 2D axisymmetric and 3D cases. Therefore, the centerline mixing distribution is sensitive to the turbulence intensity [38] and defining the turbulence intensity using Eq. (4.3) improves predictions when the bluff-body is not included in the domain.

Figure 4.9 (b) shows the radial profiles of mixture fraction (left axis) and temperature (right axis) at $X/D_j = 20$. Experimental results are shown as triangles for mixture fraction and squares for temperature. There are two sets of data shown for the experiments and the small variance in Raman-scattering measurements is because the variables were monitored on both sides of the flame; thus both sets of data are shown in Figure 4.9 (b). The predictions are presented as various lines for the 2D axisymmetric and 3D simulations. It is clear that the 3D simulation with $I = 4\%$ shows the best predictions compared with experiments, which is consistent with the conclusions

for Figure 4.9 (a). Upon further examining Figure 4.9 (b), the 2D axisymmetric simulations work reasonably well for numerical predictions of radial mixture fraction and temperature. However, the choice of turbulence intensity affects the results and gives different predictions near the centerline ($R/D_j \sim 0$) when the computational domain is defined immediately downstream of the bluff body.

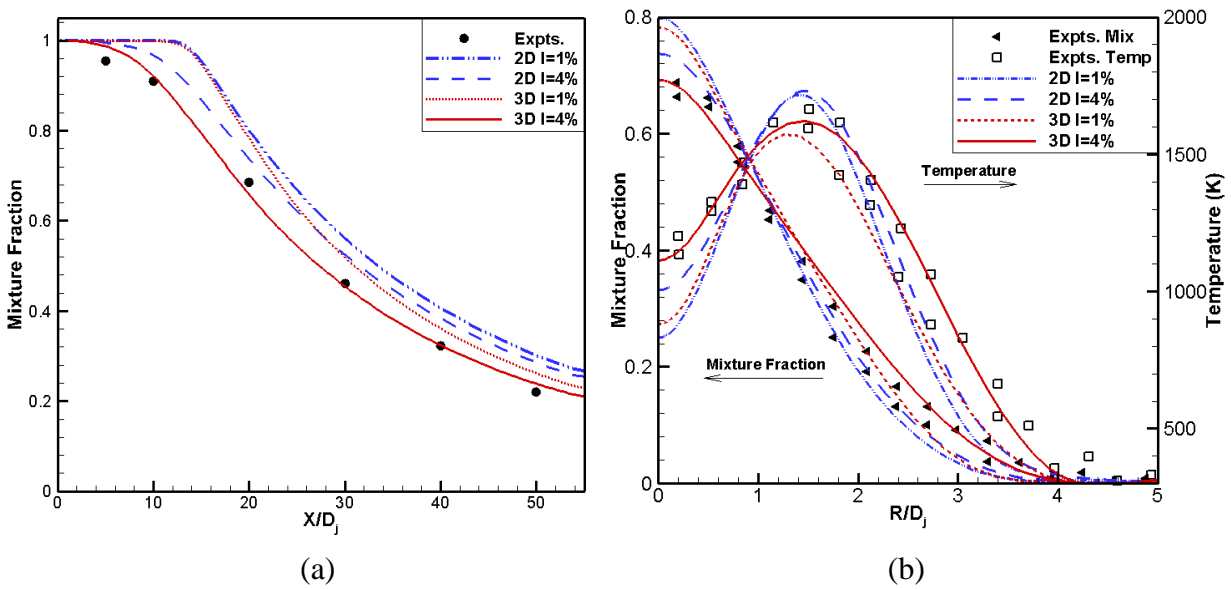


Figure 4.9 (a) centerline profiles of mixture fraction; (b) radial profiles of mixture fraction and temperature at $X/D_j=20$

Figure 4.10 shows the velocity and strain rate distributions along the centerline. The two variables are useful parameters to investigate the jet flame structure. Analyzing profiles of mixture fraction, velocity distribution (axial and radial) and strain rate provides a better understanding for the effects of turbulence intensity and geometry on mixing and fluid dynamics in the reaction zone. In Figure 4.10 (a), the effects of I on the centerline velocity magnitude are very similar to that observed with the mixture fraction profile in Figure 4.9 (a). When $I = 1\%$, the magnitude remains constant at 80 m/s until the axial distance exceeds $X/D_j = 15$, which is similar to the mixture

fraction distribution for the cases with $I = 1\%$, shown in Figure 4.9 (a). The consistent trends indicate that the turbulence intensity of 1% neglects the velocity fluctuations, yielding an unphysical prediction of the flow at the inlet and therefore overpredicts mixture fraction and velocity magnitude near the centerline.

Figure 4.10 (b) shows the profiles of strain rate distributions along the centerline for 2D axisymmetric and 3D cases with $I = 1$ and 4%. The mixing rate can be characterized by the scalar dissipation rate, which is related to the strain rate and provides a crucial measure of the mixing rate and flame characteristic [70, 131]. The cases with $I = 1\%$ have significant changes and higher maximum strain rate compared with $I = 4\%$. Strain rate does not change much from $X/D_j = 0$ to 10 with $I = 1\%$, which means the mixing along the radial direction near the inlet of the burner has been suppressed because the inlet turbulence intensity underpredicts the velocity fluctuation. However, from $X/D_j = 10$ to 20, strain rate for the cases with $I = 1\%$ increases significantly and is higher than for $I = 4\%$. The relationship between strain rate and combustion characteristics, like mixture fraction and temperature, have been reported [132, 133] that increasing strain rate decreases temperature but increases mixture fraction. Figure 4.10 (b) shows the difference in strain rate due to inlet turbulence intensity and emphasizes the importance when the bluff-body is not included in the computational domain.

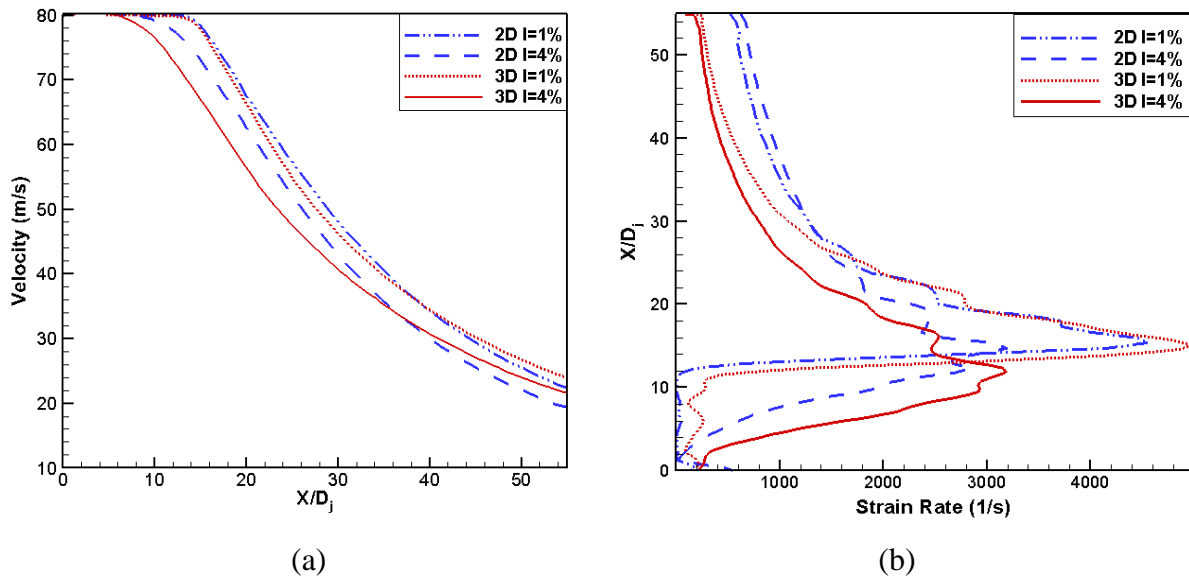


Figure 4.10 Centerline profiles for $I = 1$ and 4% (NoBB): (a) velocity magnitude; (b) strain rate

4.6. Effects of the bluff-body addition

To further assess the inlet velocity profile and the inlet turbulence intensity, a comparison is pursued to assess computational domain effects with the bluff-body included (BB) and excluded (NoBB) in the 2D axisymmetric domain with $I = 1\%$ and 4% . Figure 4.11 depicts the mixture fraction comparisons at the centerline and shows the cases without and with the bluff body using various lines. The two cases labeled ‘NoBB’ are the same results from the 2D cases shown in Figure 4.9 and Figure 4.10 and repeated here for direct comparison. In Figure 4.11, the results with the bluff-body in the computational region improve, showing better agreement with experimental results. Moreover, for the computational domain with the bluff-body, the two cases with different inlet turbulence intensities predict identical mixture fraction profiles. These results suggest that the inlet turbulence intensity is less important when the bluff body is included in the computational domain. A plausible explanation is that the length of the bluff body passage gives the fuel and air

streams time to develop, which makes the initial assumption of the velocity fluctuation and the turbulence intensity less influential on the mixing and combustion characteristics.

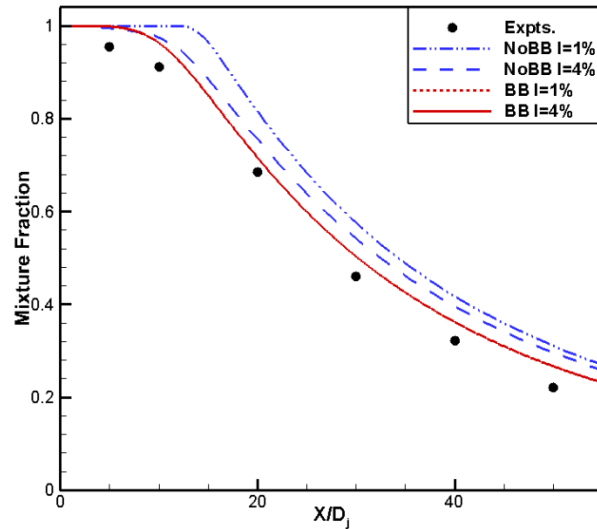


Figure 4.11 Mixture fraction profiles along the centerline comparing experiments [16] and 2D axisymmetric simulations without and with the bluff body

Figure 4.12 compares the radial profiles of mixture and the radial profiles of temperature at $X/D_j = 10$ and 20 . Similar to previous findings in Figure 4.11, the radial profiles demonstrate that the results with the bluff-body in the computational domain better predict mixture fraction and temperature when compared with experiments and are indistinguishable irrespective of inlet turbulence intensity.

To better understand the effects of the computational domain with the bluff-body, profiles of the axial velocity are shown in Figure 4.13 at locations of 0.06 m, 0.08 m and 0.115 m (exit of the BB) for $I = 1\%$. The locations are marked and shown in Figure 4.14. The axial velocity profiles are virtually identical, suggesting that the velocity field is fully developed. According to the turbulence correlation for the location x_{fd} where flow becomes fully-developed in a pipe, $x_{fd} = 4.4 Re^{-1/6} D_j$, the flow should become fully developed at approximately 0.068 m

downstream of the bluff-body entrance. The profiles shown in Figure 4.15 agree with the correlation and further substantiate the findings that the bluff-body not only stabilizes the flame but creates a fully-developed fuel velocity when it mixes with air.

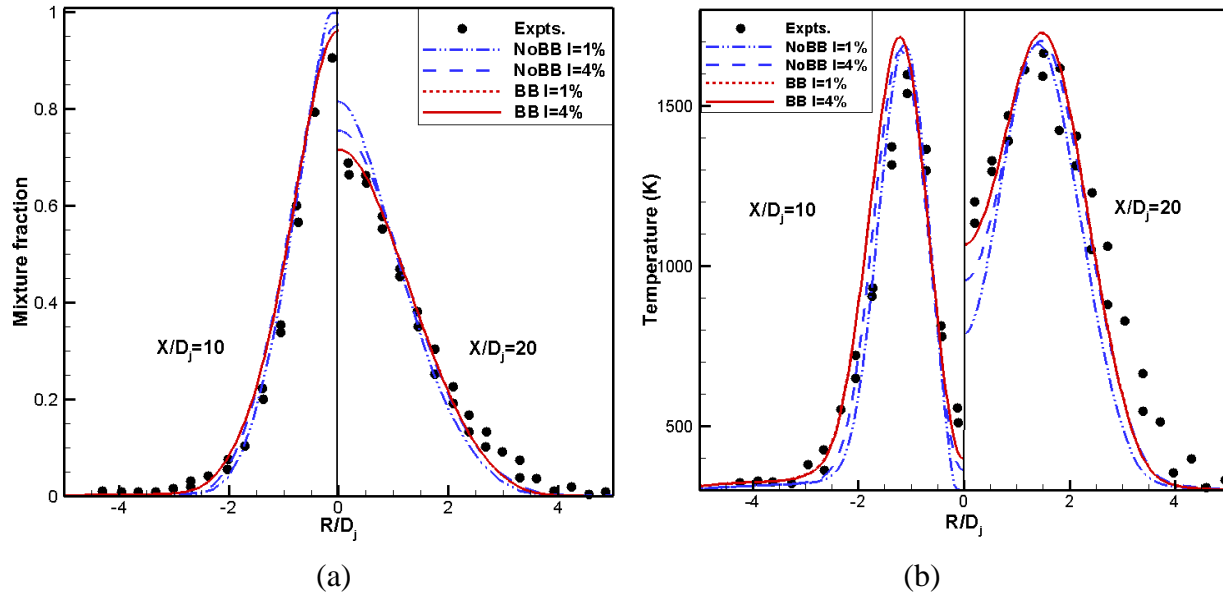


Figure 4.12 Radial profiles at $X/D_j = 10$ and 20 comparing experiments [16] and 2D axisymmetric simulations without and with the bluff body: (a) mixture fraction; (b) temperature

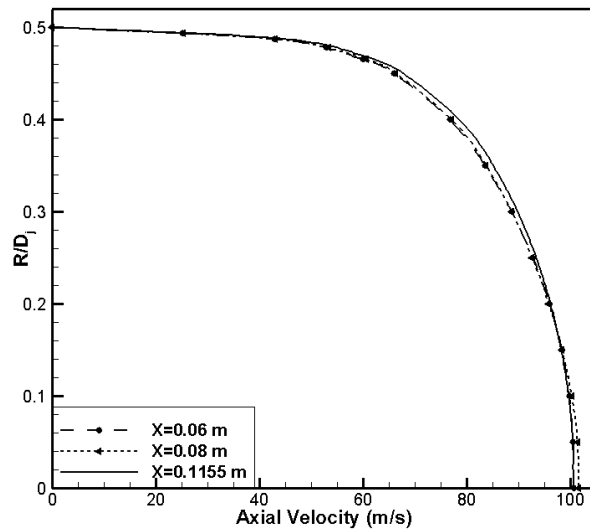


Figure 4.13 Axial velocity profiles at different axial locations within the bluff-body when $I = 1\%$

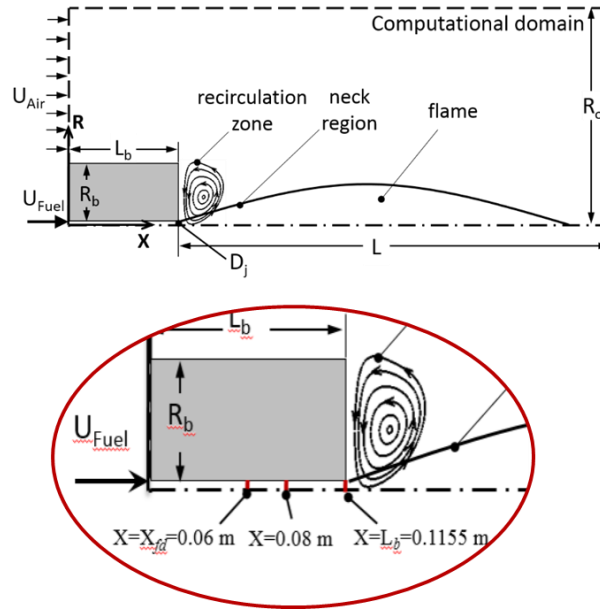


Figure 4.14 Axial positions for the profile shown in Figure 4.13

Establishing that the flow is fully-developed at the bluff-body exit, the turbulence intensity can be further assessed to compare and better understand the results when specifying I at the inlet. Figure 4.15 presents u/U at the end of the bluff-body, which is the location that corresponds to the inlet for the cases without the bluff-body. The profiles for the NoBB cases are uniform because the inlet velocity profile is uniform, as discussed in Section 4.4. The profiles for the BB cases are nonuniform based on the velocity field that develops at the exit of the bluff body, as shown in Figure 4.15. Figure 4.15 elucidates that the BB profiles are almost identical although the initial inlet turbulence intensities are different, and is consistent with previous findings shown in Figure 4.11 to Figure 4.12 whereby the addition of the bluff-body diminishes the differences irrespective of inlet turbulence intensities. With the addition of the bluff-body, the turbulence intensity at the bluff-body exit is not uniformly distributed as assumed in the cases without the bluff-body. With the bluff-body, turbulence intensity increases in the radial direction with more turbulence fluctuations and radial flow interactions. The turbulence intensity of the BB cases near the core of

the flame (i.e., near the centerline) is very close to 4%, which is the inlet turbulence intensity calculated using Eq. (4.3) [130] for the simulations without the bluff-body.

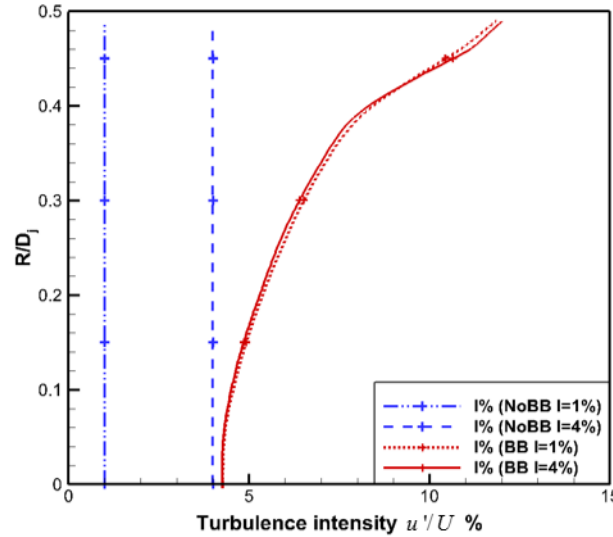


Figure 4.15 Turbulence intensity profiles at the end of the bluff-body

An additional simulation was performed using the 2D axisymmetric domain without the bluff-body but specifying the full-developed axial velocity profile at $x = 0.115$ m (shown in Figure 4.14) with $I = 4\%$. The results from this simulation were compared to the results of the 2D axisymmetric domain with the bluff-body included. The profiles for centerline and radial mixture fraction, and radial temperature were very similar (although not shown herein), demonstrating that if the velocity profile at the bluff-body exit is known, it can be used to obtain very good results without the need to explicitly model the bluff-body. However, à priori knowledge of the velocity profile at the bluff-body exit is not readily available for most problems of interest without experimental measurements. Thus, there is an advantage to model the bluff-body, even in only two dimensions, for more accurate results.

To further investigate the predictive accuracy modeling the bluff-body, Figure 4.16 shows the mixture fraction and temperature contours of the NoBB (upper) and BB (lower) cases. The contours with $I = 1\%$ and 4% are spliced to compare the differences. In Figure 4.16, for the results without the bluff body, the peak values do not align at the centerline. However, in the bottom two contours in Figure 4.16, the mixture fraction and temperature for $I = 1\%$ and 4% align perfectly when the bluff body is included. These results are consistent with previous statements that differences diminish regardless of inlet turbulence because the existence of the entrance region with the bluff body gives time for the gas streams to develop before they mix and combust.

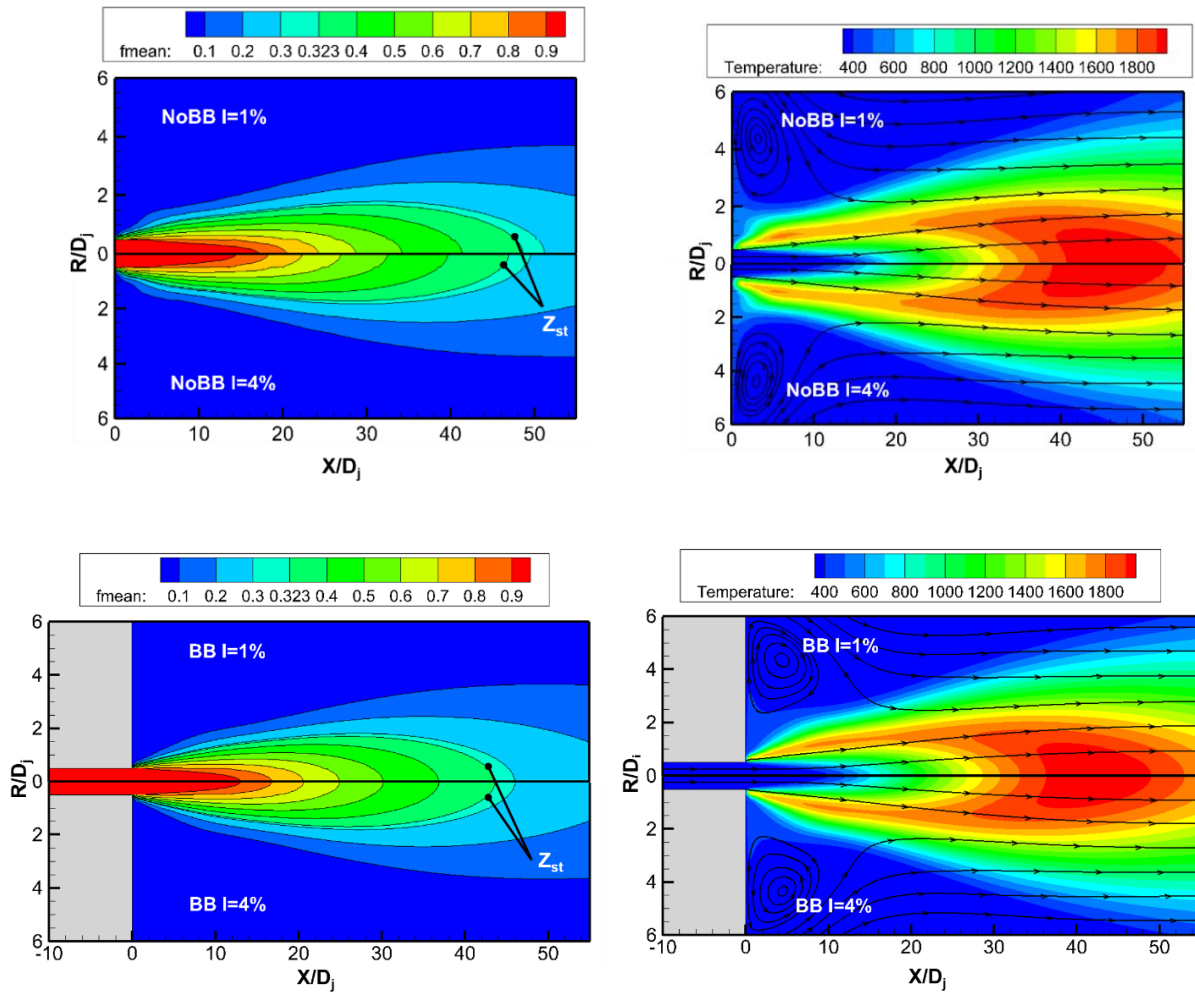


Figure 4.16 Comparison of mixture fraction (left) and temperature (right) when $I = 1\%$ and 4% for NoBB cases (upper) and BB cases (lower)

Table 4.1 Summary of the relative errors and CPU time

Computational domain	I (%)	Error (%)	CPU time (s)
Bluff body excluded in the 2D axisymmetric domain	$I = 1\%$	18.5	128
	$I = 4\%$	13.5	122
Bluff body excluded in the 3D domain	$I = 1\%$	11.3	4080
	$I = 4\%$	1.4	4085
Bluff body included in the 2D axisymmetric domain	$I = 1\%$	7.5	214
	$I = 4\%$	7.5	210

In addition, the streamlines have been superimposed with the temperature contours in Figure 4.16. In Figure 4.16, a recirculation zone forms downstream of the bluff body. It is well known that the recirculation zone has a dominant effect on the flame stabilization in the bluff-body combustor [59]. It also has significant influence on the reaction zone, which can be related to the high OH concentration region [59]. In both figures, the streamlines have similar distributions and shapes in the recirculation zone.

Table 4.1 compares the relative error and CPU time for all tested cases in the present work. The relative error has been calculated based on the experimental data of centerline mixture fraction of the combustor and the CPU times are for 1,000 iterations. In Table 4.1 for the 2D and 3D cases without the bluff body, the use of the inlet turbulence intensity based on Eq. (4.3) has greatly improved the results and the relative errors decrease. Also, the 3D cases have smaller relative errors compared to the 2D cases without the bluff body; however, the computational time needed for 3D cases is much longer than the 2D cases. The addition of the bluff body in the computational region for the 2D axisymmetric cases improves the predictions with smaller errors compared to ‘NoBB’ cases and requires less CPU compared to the 3D cases. Therefore, it is recommended to model the bluff body in the 2D axisymmetric domain, which reduces numerical error, saves computational time and is independent of inlet turbulence intensity. However, reasonable results,

although not as accurate near the jet centerline ($r = 0$) can be achieved using the 2D axisymmetric domain provided that the inlet turbulence intensity is defined using Eq. (4.3) to incorporate physical characteristics of the flow.

4.7. Conclusions

A comparative study of turbulence models and operating conditions has been conducted in this chapter to generate the best turbulence modeling technique for the non-premixed turbulent combustion. To begin, the modeling methods of RANS and LES have been tested and compared. The results have found that LES model shows some interesting propagation of the diffusion flame but the time-averaged results reveal very smooth temperature profile close to RANS results. Since the LES model needs much longer computational time than the RANS method, and that the RANS approach can capture the mean flow features fairly well, the RANS approach is determined more suitable in the following study. Then, a study of five RANS-based turbulent models was conducted to assess the models and compare with the experimental results from Correa and Gulati [16] for a non-premixed 32.3% H_2 /27.5% CO /40.2% N_2 syngas flame. Results show that since the realizable k - ϵ model and RSM model account for the effects of streamline curvature, swirl, rotation, and rapid changes in strain rate, they have shown good prediction of the flame characteristics in the non-premixed syngas flame, such as mixture fraction, temperature and mass fraction of species.

A numerical study on the effects of inlet turbulence intensity and computational domains (2D axisymmetric or 3D; bluff body included or not) on the non-premixed turbulent combustion characteristics was also conducted. Extensive measurements of the flow, mixing and temperature fields were compared and validated with Correa and Gulati flame. It was found that 3D simulations with $I = 4\%$, based on a published empirical correlation by Durst et al. [130] gave the best agreement with experimental results along centerline and radial distance when the bluff body was

not modeled in the computational domain. Therefore, it was concluded that the inlet turbulence intensity in the fuel-jet has a substantial impact on the axial decay of mixture fraction and temperature, velocity, and strain rate when the bluff body is not modeled. Thus, the conclusions [16, 39, 55] that the flow is relatively insensitive to the inlet velocity and turbulence intensity profiles are misleading when the computational domain is modeled without the bluff-body. Furthermore, the results are very reasonable using a 2D axisymmetric domain with uniform inlet velocity profile if the turbulence intensity is correctly specified.

It was also found that the addition of the bluff body improves the 2D axisymmetric predictions, which agree better with experimental data. Also, the addition of the bluff body diminished differences caused by specifying inlet turbulence intensities, which made the numerical predictions indistinguishable, irrespective of inlet initial values. This is because the length of the bluff body allows the fuel and air streams to fully develop before they mix and combust. By comparing the relative errors and computational time of all cases, 3D modeling is not a practical since the computational time is much longer than the 2D cases. The inclusion of the bluff body in the 2D axisymmetric domain is appropriate since it can maintain numerical accuracy and eliminate differences caused by initial inlet parameters, without incurring longer computational times.

Chapter 5. Turbulent combustion application in the other bluff-body flame

5.1. Introduction

The CFD approach has been used in previous chapters to efficiently simulate the bluff body flames and provide fundamental insights to understand the flow, temperature and species characteristics. In the present work, the established CFD model is applied to another bluff-body flame from Dally et al. [134] to test its predictive performance and capability. The non-dimensional computational domain is shown in Figure 5.1 and the dimensions of the bluff-body burners from Correa and Gulati [16] and Dally et al. [134] are compared in Table 5.1. Both bluff-body burners have been non-dimensionalized based on their fuel jet diameters D_j that is the diameter of the bluff-body opening. Roquemore et al. [135] have mentioned that bluff-body flames, either fuel-jet dominant or coflow-air dominant, mainly depend on the velocities of each stream as well as the ratio of the bluff-body radius (R_b) to the central fuel-jet diameter D_j . Therefore, in the present work, as shown in Table 5.1, the bluff-body flame from Dally et al. [134] burner with different bluff-body to jet ratio from Correa and Gulati burner [16] will be studied. Additionally, Table 5.1 also summarizes the detail syngas fuel compositions (in terms of volume fraction) and the velocities of the streams for the experimental operating conditions.

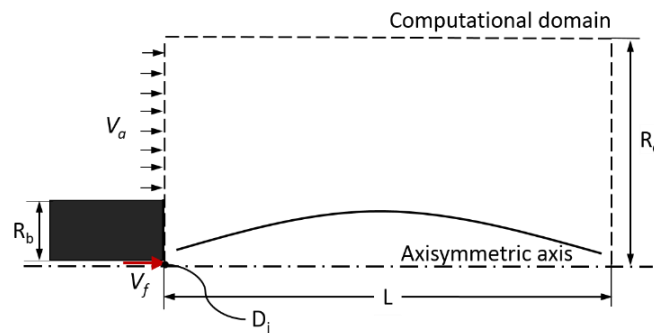


Figure 5.1 Schematic of CFD simulation of bluff-body flame

Table 5.1 Experimental bluff-body flames studied in this paper

Flame	D_j (mm)	R_b	L	R_o	Fuel	V_f/V_a	I (%)
Correa et al. [16]	3.18	$6D_j$	$117D_j$	$23.6D_j$	27.5% CO/32.2% H ₂ /40.2% N ₂	80/6.5	4.0%
Dally et al. [134]	3.6	$6.9D_j$	$187.5D_j$	$35.3D_j$	50% CH ₄ /50% H ₂	118/40	4.8%

5.2. Experimental setup and uncertainty estimation

Based on the measurement technique in the work of Dally et al. [134], each measurements with variables like mixture fraction and temperature along the axial and radial directions have been stored in the database from the University of Sydney [136]. However, quantifying the accuracy of the averaged data is very difficult [134]. Three types of errors exist in the measurements, including random, systematic and interference error [134], which can be caused by electronic noise, drift in the calibration and interference resources, respectively. To eliminate the errors as much as possible, the experiment has made more than 600 times measurements for a single data point with database available [136]. In the present study, the error bar for each experimental data is presented with the calculations of different experimental uncertainty estimate method to represent the variability of the mean values and to help understand the predictive performance of the CFD model.

5.2.1. Uncertainty estimation method

5.2.1.1. Standard deviation

The standard deviation is a measure that is generally used to quantify the amount of variation or dispersion of a set of data and can serve as a measure of uncertainty [137]. Given the statistical results of a single sample of n measurements, the relationship between standard deviation and mean is:

$$\sigma = \sqrt{\frac{\sum_{i=1}^n (X_i - \bar{X})^2}{n-1}} \quad (5.1)$$

where \bar{X} is the mean value under n instantaneous measurements.

5.2.1.2. 95% Confidence Interval

Different from the standard deviation method, the 95% confidence interval represents the variance of the mean value \bar{X} . It is thus an estimate of the lack of repeatability caused by random errors. The uncertainty can be represented as:

$$P = Z_{\alpha/2} \cdot \frac{\sigma}{\sqrt{n}} = Z_{\alpha/2} \cdot \sqrt{\frac{\sum (X_i - \bar{X})^2}{n(n-1)}} \quad (5.2)$$

where Z represents the critical value for the 95% confidence level that equals to 1.96. The 95% confidence estimate is interpreted as the experiment being 95% confident that the true mean value of the bias error, if known, would fall within $\pm P$.

5.2.1.3. ASME measurement uncertainty

In 1991, Journal of Fluids Engineering (JFE) and Journal of Heat Transfer (JHT) [138, 139] adopted a statement on the experimental uncertainty by Coleman and Steele [140, 141] as the principle guideline to determine the measurements uncertainty. The principle guideline suggests that the presentation of the experimental data uncertainties should include the following information:

1. The uncertainty, U .

The $\pm U$ interval is the estimated uncertainty, which lies the relationship with the bias limit B_r and the precision limit P_r as

$$U_r = \sqrt{B_r^2 + P_r^2} \quad (5.3)$$

Figure 5.2 shows a schematic to illustrate the relationship between the bias limit component β and precision limit component ε at the k and $k+1$ measurements. Since the bias component β is the distance from the mean value to the true value while the precision error represents the difference between the measurement to the mean value.

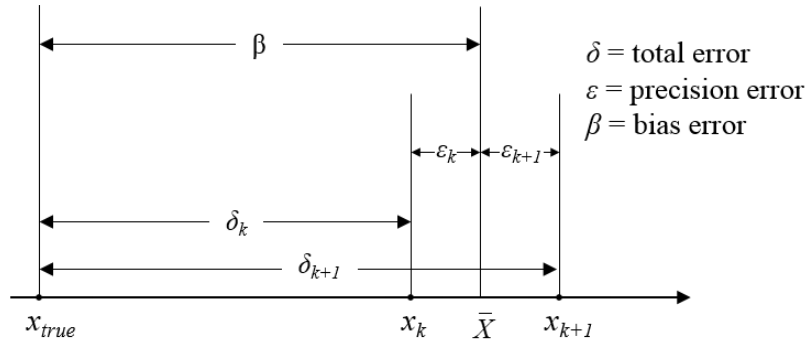


Figure 5.2 Errors in the measurement of a variable x

2. The precision limit, P_r .

If n measurements at the same test condition are obtained, the precision limit P_r should be associated with:

$$P_r = t\sigma_r \quad (5.4)$$

where t is determined with $n-1$ degrees of freedom and is taken as 2 for $n \geq 10$ and σ_r is the standard deviation of the sample of n results, shown in Eq. (5.1). Therefore, the precision limit that should be associated with the mean result is given by:

$$P_{\bar{r}} = \frac{P_r}{n} \quad (5.5)$$

The uncertainty $U_{\bar{r}}$ associated with the mean value \bar{r} should be:

$$U_{\bar{r}}^2 = B_r^2 + (2\sigma_r / \sqrt{n})^2 \quad (5.6)$$

3. The bias limit, B_r .

The bias limit is an estimate of the magnitude of the fixed, constant error, which is the difference between the true value and the mean value. If a variable r is a function of other variables, such as $r = r(X_1, X_2, X_i, \dots, X_j)$, where X_i is the measurement of one other variable, the uncertainty propagation equation of the bias limit is:

$$B_r^2 = \sum_{i=1}^j \theta_i^2 B_i^2 + \sum_{i=1}^j \sum_{k=i+1}^{j-1} \theta_i \theta_k B_{ik}^2 \quad (5.7)$$

and

$$\theta_i = \frac{\partial r}{\partial X_i} \quad (5.8)$$

Take mixture fraction, as an example. Based on the definition and relationship for mixture fraction, mixture fraction can be further derived as:

$$f = \frac{\frac{2(Z_C - Z_{C,o})}{W_c} + \frac{(Z_H - Z_{H,o})}{2W_H} - \frac{2(Z_O - Z_{O,o})}{W_o}}{\frac{2(Z_{C,F} - Z_{c,o})}{W_c} + \frac{(Z_{H,F} - Z_{H,o})}{2W_H} - \frac{2(Z_{O,F} - Z_{O,o})}{W_O}} \quad (5.9)$$

which makes the bias limit:

$$B_f^2 = \theta_C^2 B_C^2 + \theta_H^2 B_H^2 + \theta_O^2 B_O^2 \quad (5.10)$$

where $\theta_C = \frac{\partial f}{\partial X_C}$; $\theta_H = \frac{\partial f}{\partial X_H}$; $\theta_O = \frac{\partial f}{\partial X_O}$ and $B_{ik} = 0$ due to the negligible cross-impact between the measured species.

Dally et al. [134] listed the error estimate of the measured species concentration associated with systematic errors, from which the bias limit of the mixture fraction can be further calculated. In reacting flows, local species compositions are required to extract temperature or density from

the Rayleigh measurements (through the ideal-gas law). Since temperature is a function of mixture fraction, the uncertainty of temperature U_T becomes:

$$U_T^2 = B_T^2 + P_T^2 = \sum_{i=1}^j \theta_f^2 B_f^2 + \frac{t^2 \sigma_T^2}{N} \quad (5.11)$$

5.2.2. Results of uncertainty estimate

Figure 5.3 shows the mean mixture fraction profiles at various axial locations (X/D_j) from the experimental measurements with the uncertainties estimated using standard deviation, 95% interval and ASME guideline methods. Apparently, standard deviation shows that the uncertainty is much larger compared to the other methods. The ASME guideline yields results close to the 95% interval method. Figure 5.4 shows the mean temperature profiles from the experimental measurements with the uncertainties. Similar to Figure 5.3, standard deviation has a much larger uncertainty than the other two methods. Mathematically, the difference between the standard deviation and the 95% confidence interval is the ratio of $\frac{Z_{\alpha/2}}{\sqrt{n}} = \frac{1.96}{\sqrt{n}}$ and when the sample size n gets larger, the difference between the two methods gets larger. The temperature uncertainties using the ASME guideline are close to the 95% confidence interval when R is from 0 to 10 mm but is larger when R exceeds 20 mm.

A specific position of experimental data is randomly chosen at the axial location of $X/D_j=12.5$ and radial location of $R=17.2$ mm, which is circled in red in Figure 5.4 (last column of images). More than 600 instantaneous measurements at this single position are plotted in Figure 5.5. The corresponding uncertainty values calculated by the three methods are also plotted in Figure 5.5 to show the range of the variability at this single point. In Figure 5.5, the range from standard deviation method rules out the extreme large or small values as well as sudden significant changes, which does not necessarily represent the uncertainty but represents the normal range of the

measurements. The range provided by the 95% confidence interval method shows a very small range that does not capture a majority of the data, which makes the approach not very appropriate to represent the range of variability during the measurements. Therefore, based on the results shown from Figure 5.3 to Figure 5.5, the method from ASME is adopted and the uncertainty results will be employed to help understand the predictive performance of the CFD model.

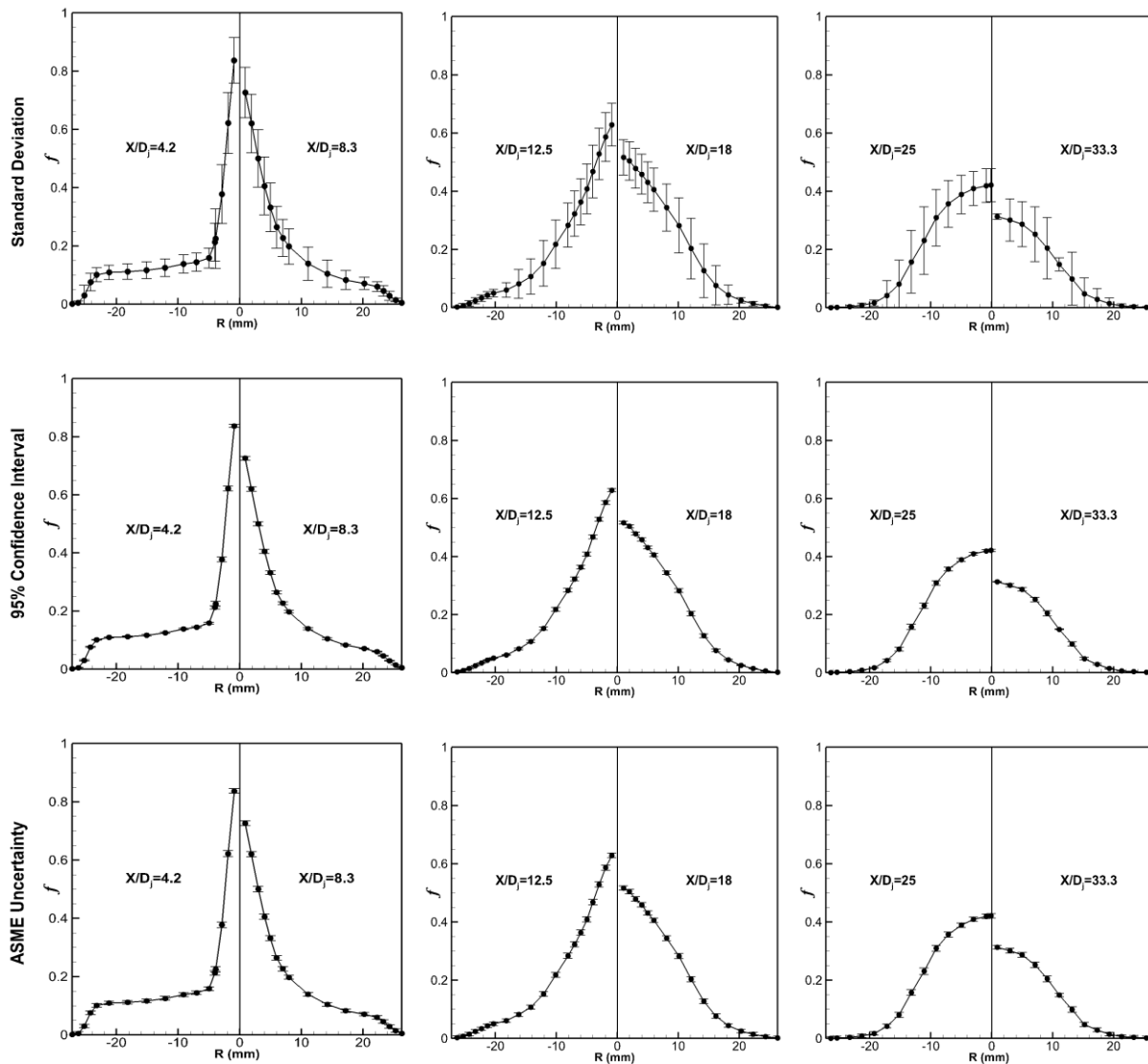


Figure 5.3 Radial profiles of mean mixture fraction from experimental measurements and estimated uncertainty using (top) standard deviation, (middle) 95% confidence interval and (bottom) ASME guideline

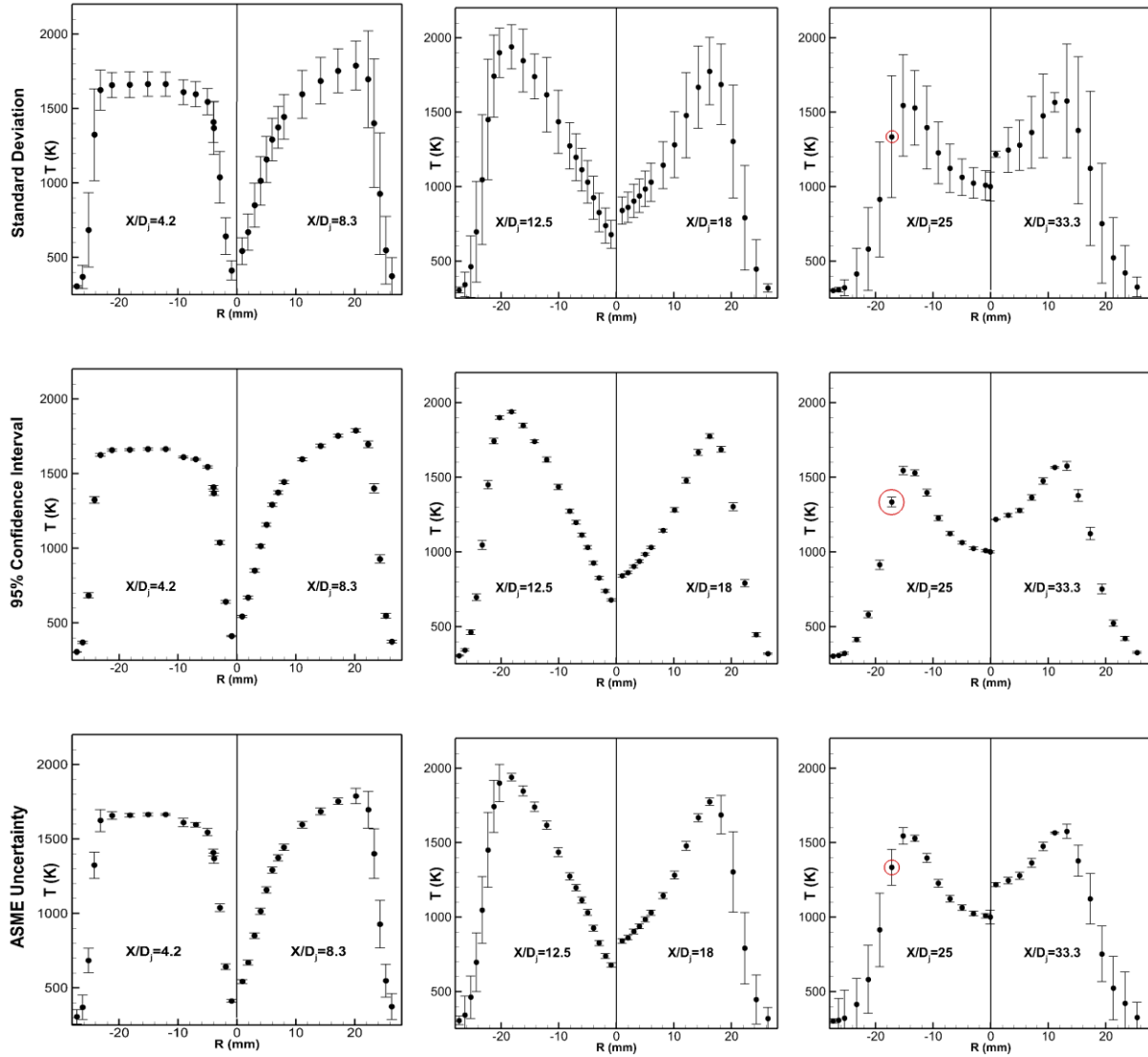


Figure 5.4 Radial profiles of mean temperature from experimental measurements and estimated uncertainty using (top) standard deviation, (middle) 95% confidence interval and (bottom) ASME guideline

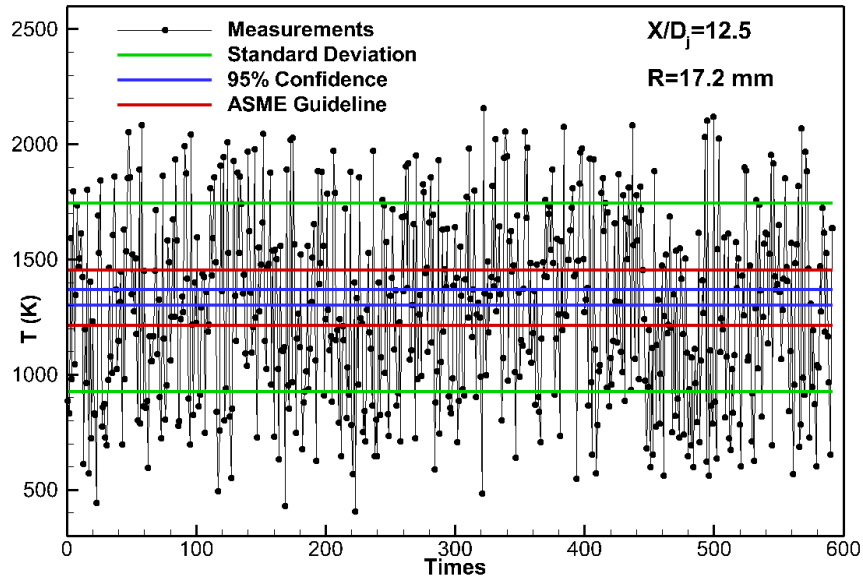


Figure 5.5 Instantaneous measurement data of temperature at $X/D_j=12.5$, $R=17.2$ mm with the uncertainties estimated using standard deviation (green line), 96% confidence interval (blue line) and ASME guideline (red line)

5.3. CFD results for the Dally et al. flame

In the current study, the bluff-body is not included in the computational domain because the fuel characteristics are specified at the inlets. The flow field data are collected by Masri et al. [18] and the velocity profile at inlet is plotted in Figure 5.6, which indicates that the flow is neither a uniform nor a fully developed. Based on the experimental measurements, as part of the CFD study, an equation was developed to represent the velocity inlet boundary condition (shown as data fit in Figure 5.6 and implemented as a user-defined function in Fluent).

Figure 5.7 (a) shows the CFD results of temperature in the full axisymmetric domain and Figure 5.7 (b) shows the enlarged contour of temperature with flow streamlines. In Figure 5.7 (a), different from the temperature results of Correa and Gulati flame, temperature reaches a maximum in the recirculation zone and flame center downstream. The reason for high temperatures in the recirculation region is that the annular co-flow has a higher velocity compared to the condition of

Correa and Gulati flame, which enhances the mixing between fuel and air. Axial positions are marked in Figure 5.7 (a), indicating that the experimental radial profiles will be extracted at these locations and compared with the CFD results in Figure 5.8 and Figure 5.9.

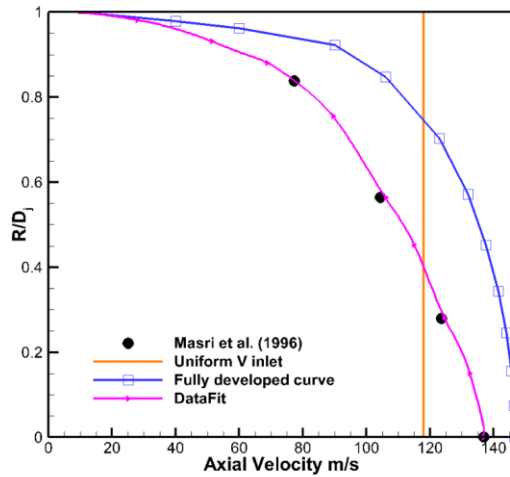
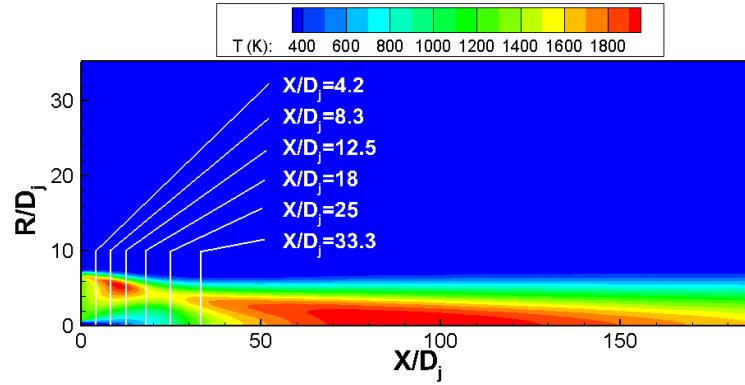
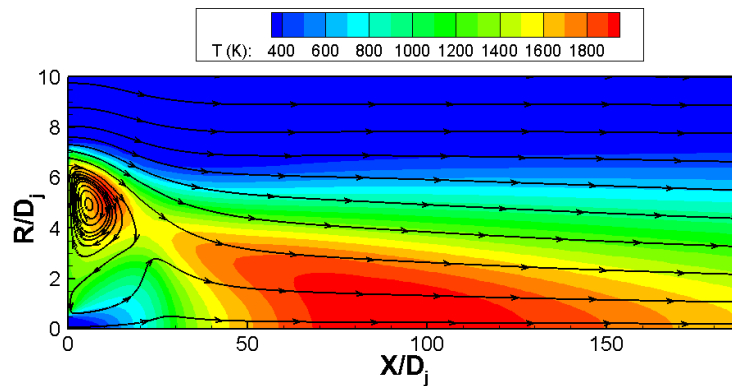


Figure 5.6 Initial jet flow field measured by Masri et al. [18]

Figure 5.8 shows the radial profiles of mixture fraction at multiple axial locations of $X/D_j=4.2$, 8.3, 12.5, 18, 25 and 33.3. Points with error bars are the experimental results from Dally et al. [17] and solid lines are CFD results. Based on the comparison shown in Figure 5.8, CFD results have very good agreement with the experimental data. In Figure 5.8 (from left to right), maximum mixture fraction at the centerline decreases along the axial location. Mixture fraction has a much higher value near the centerline where R is around zero and decreases along the radial direction, which means that fuel is consumed with more entrainment of air. It should be noted that at $X/D_j=4.2$ and 8.3, the bluff body creates a more uniform region of flow immediately downstream; thus, the mixture fraction profile is relatively constant. The reason for the uniform flow can be attributed to the annular co-flow velocity, which is six times greater than the case for Correa and Gulati [16].



(a)



(b)

Figure 5.7 Temperature contours of CFD predictions of the Dally et al. flame: (a) temperature contours in full axisymmetric domain and (b) temperature contour with streamlines in enlarged scale

Figure 5.9 shows the radial profile of temperature at the same set of axial locations. Similar to Figure 5.8, CFD results show good agreement with experimental results. The maximum temperature in the radial profiles corresponds to the recirculation region shown in the temperature contour in Figure 5.7. The highest temperature in each radial profile happens when the mixture fraction is around the stoichiometric mixture fraction $f_{st}=0.056$. Therefore, the current work demonstrates good performance of the established CFD model in different bluff-body flames. The work of Dally et al. flame provides valuable information for the study of chemical reaction network in the following chapter.

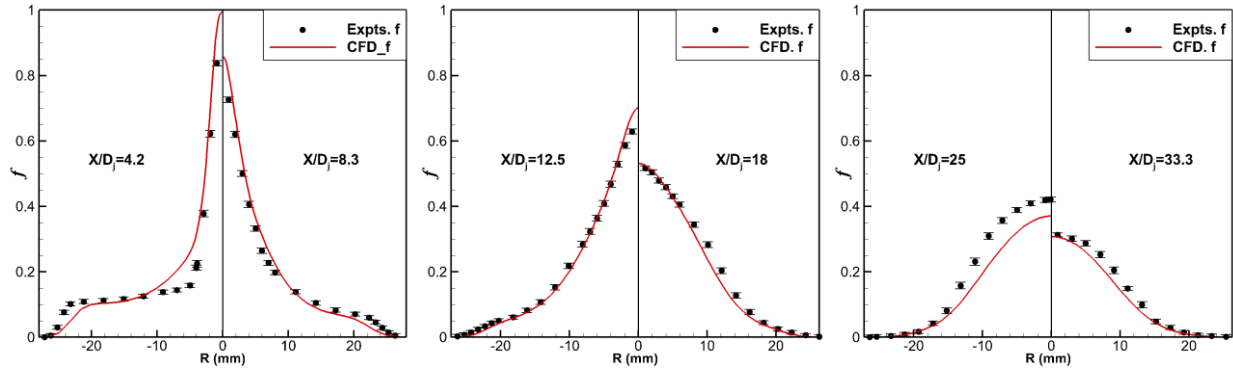


Figure 5.8 Radial profiles of mixture fraction from experimental measurements and CFD results

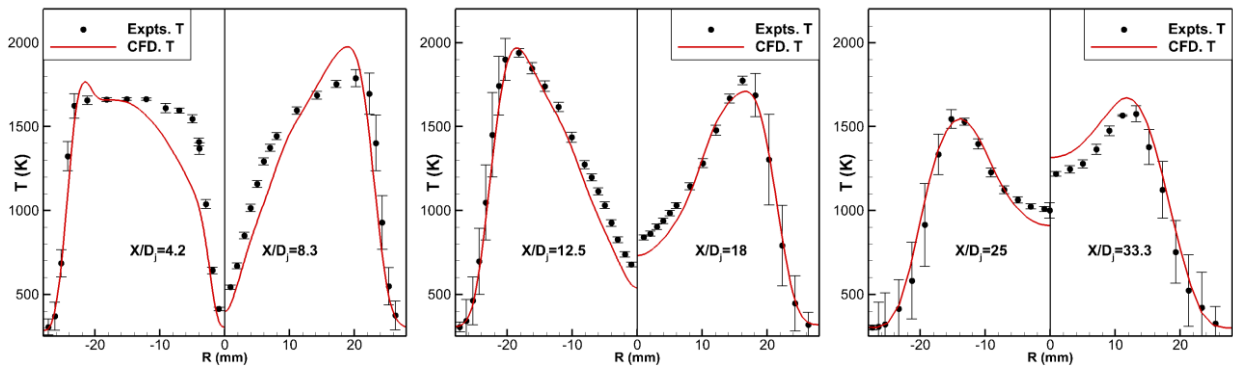


Figure 5.9 Radial profiles of mean temperature from experimental measurements and estimated uncertainty using three different method

5.4. NO_x prediction

NO_x is an important pollutant emission and is defined as the sum of NO and NO₂. The PDF-equilibrium is not suitable for slow chemistry (NO_x calculations) since the chemical equilibrium is immediately established at the molecular level once the reactants are mixed. Therefore, the post-processor NO_x model is used to predict the NO mass fraction and the NO_x formation does not have an important effect on the flow field and combustion characteristics. Since NO is considered as the most important species for many types of flames [142], the thermal NO formation mechanism extended from the Zeldovich mechanism is mainly employed as the mechanism of highly temperature-dependent reactions. The thermal NO formation mechanism is:





The net rate of formation of NO via the above three reactions is:

$$\frac{d[\text{NO}]}{dt} = \kappa_{f,1}[\text{O}][\text{N}_2] + \kappa_{f,2}[\text{N}][\text{O}_2] + \kappa_{f,3}[\text{N}][\text{OH}] - \kappa_{r,1}[\text{NO}][\text{N}] - \kappa_{r,2}[\text{NO}][\text{O}] - \kappa_{r,3}[\text{NO}][\text{H}] \quad (5.15)$$

where $\kappa_{f,1}$, $\kappa_{f,2}$, and $\kappa_{f,3}$ are the rate coefficients for the forward reaction and $\kappa_{r,1}$, $\kappa_{r,2}$ and $\kappa_{r,3}$ are the reverse rate coefficients. The rate coefficient for the reactions have been measured in numerous experimental studies [143-145] and have been further evaluated by Baulch et al [146] and Hasson and Salimian [147]. The rate coefficients for Eq. (5.12) – (5.14) are given below based on the evaluation from Hasson and Salimian [147]: $\kappa_{f,1} = 1.8 \times 10^8 e^{-38370/T}$, $\kappa_{r,1} = 3.8 \times 10^7 e^{-425/T}$, $\kappa_{f,2} = 1.8 \times 10^4 T e^{-4680/T}$, $\kappa_{r,2} = 3.81 \times 10^3 T e^{-20820/T}$, $\kappa_{f,3} = 7.1 \times 10^7 e^{-450/T}$, $\kappa_{r,3} = 1.7 \times 10^8 e^{-24560/T}$.

Units of rate coefficients are $\text{m}^3/\text{gmol}\cdot\text{s}$. Assuming a quasi-steady for concentration of nitrogen atoms and the reaction in Eq. 5.12 as the rate-limiting step, the NO formation rate can be further derived:

$$\frac{d[\text{NO}]}{dt} = 2\kappa_{f,1}[\text{O}][\text{N}_2] \cdot \left(1 - \frac{\kappa_{r,1}\kappa_{r,2}[\text{NO}]^2}{\kappa_{f,1}[\text{N}_2]\kappa_{f,2}[\text{O}_2]} \right) / \left(1 + \frac{\kappa_{r,1}[\text{NO}]}{\kappa_{f,2}[\text{O}_2] + \kappa_{f,3}[\text{OH}]} \right) \quad (5.16)$$

Therefore, the NO formation can be decoupled from combustion simulations for temperature, species, O atoms and OH radicals. The prompt NO formation rate is described by the following equations [148]:

$$\frac{d[\text{NO}]}{dt} = \kappa_c \kappa_{prompt} [\text{O}_2]^\alpha [\text{N}_2] [\text{fuel}] e^{-E_a/RT} \quad (5.17)$$

where κ_c is a correction factor that depends on the fuel type and fuel air ratio and α is the order of reaction.

To determine the O radical concentration, the partial equilibrium approach calculation is assumed by accounting for third-body reactions in the O₂ dissociation process:



The concentration of O radical can be calculated as [149]:

$$[\text{O}] = 36.64T^{1/2}[\text{O}_2]^{1/2} e^{-27123/T} \quad (5.19)$$

where the concentration unit is gmol/m³ and the third body M could be H₂, H₂O, CH₄, CO, CO₂ and inert molecule Ar. The concentration of OH is given with the partial equilibrium of O + H₂O ↔ 2OH from Baulch et al. [150] and Westbrook et al. [151]:

$$[\text{OH}] = 2.129 \times 10^2 T^{-0.57} e^{-4595/T} [\text{O}]^{1/2} [\text{H}_2\text{O}]^{1/2} \quad (5.20)$$

Figure 5.10 shows the scatter plots of NO from the experimental work and the solid line is the NO prediction from CFD. Each sub-figure corresponds to a different axial position, namely X/D_j=4.2, 8.3 and 12.5. Different from Figure 5.8 and Figure 5.9, both experimental results and CFD results of NO have been plotted along the mixture fraction. The peak NO happens when the mixture fraction is near the stoichiometric mixture fraction. Figure 5.10 shows similar shapes as temperature profiles along the mixture fraction in Figure 5.11, where temperature reaches maximum at the stoichiometric mixture fraction. The similar distribution demonstrates that NO distribution is highly dependent on temperature, which agrees with the theoretical correlation in Eq. (5.16).

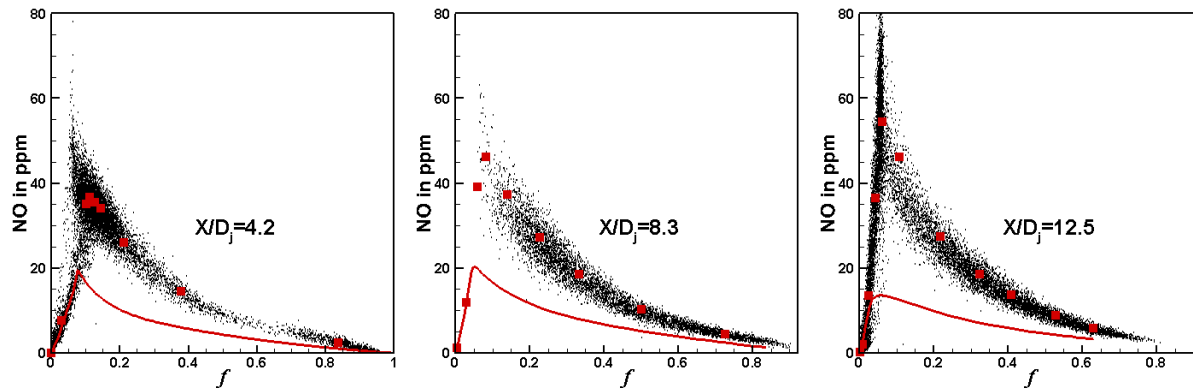


Figure 5.10 Scatter plots of NO from experimental database (black points: instantaneous value; red points: mean value) and solid profile of NO prediction from CFD model

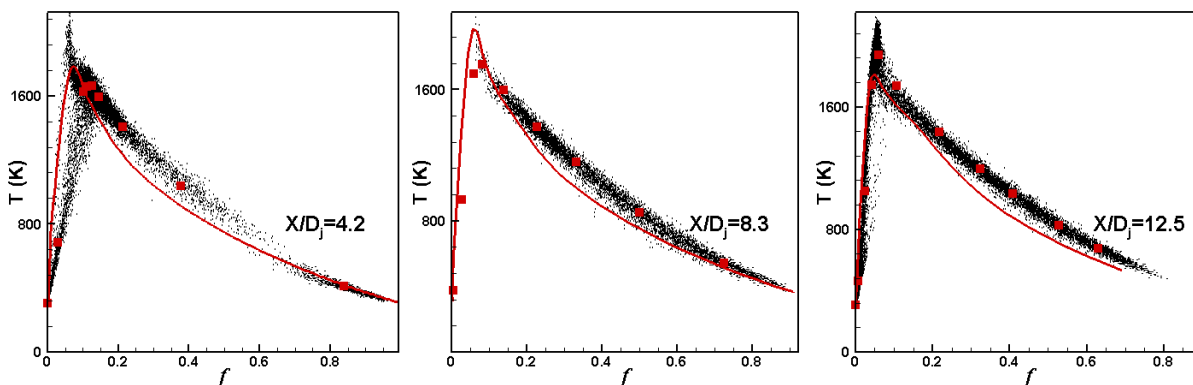


Figure 5.11 Scatter plots of temperature from experimental database (black points: instantaneous value; red points: mean value) and solid profile of temperature prediction from CFD model

5.5. Effects of fuel mixtures on NO emission

This section presents the effects of hydrogen compositions and nonflammable diluents mixtures on the combustion and NO emission characteristics for Correa and Gulati flame. Although there has been an extensive body of literature dealing with the study of syngas mixtures on effective NO_x reduction, most of these studies focused on reducing NO_x emission at the penalty of reduced flame temperature [30, 61-66]. Since numerical investigation is an efficient way to characterize the effects of syngas components on NO_x emission and flame temperature, a thorough

analysis of flame compositions and diluents mixture will be conducted based on the established and validated turbulence modeling technique.

In Table 5.2, cases 1 to 4 are tested with hydrogen composition changing from 22.3% to 52.3% and cases 2, 5 and 6 are applied to test with different diluents compositions. The syngas composition of case 2 is the syngas used in the experiments from Correa and Gulati [16]. Non-flammable N₂ and the total volume from the fuel side remain the same in the cases 1 to 4. Therefore, as H₂ increases, CO decreases in the syngas mixture.

Table 5.2 Fuel-side operating conditions (volumetric analysis)

Case	% H ₂	% CO	%N ₂	% CO ₂	% H ₂ O	f_{st}
1	22.3	37.5	40.2	0	0	0.346
2	32.3	27.5	40.2	0	0	0.323
3	42.3	17.5	40.2	0	0	0.291
4	52.3	7.5	40.2	0	0	0.259
5	32.3	27.5	30.2	10	0	0.345
6	32.3	27.5	30.2	0	10	0.317

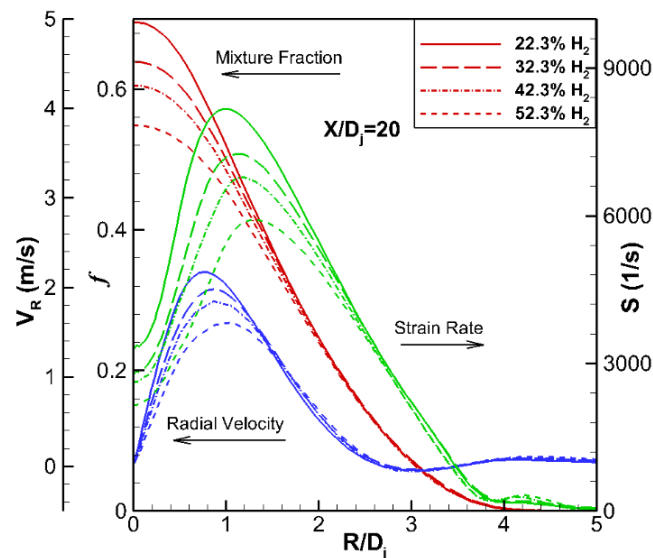


Figure 5.12 Radial profiles of mixture fraction, strain rate and radial velocity at $X/D_j = 20$

Figure 5.12 shows the radial profiles of mixture fraction and radial velocity with separate axes on the left, and strain rate using the right axis. The strain rate and radial velocity are useful parameters to investigate the jet flame structure. In Figure 5.12, the increase of hydrogen concentration decreases the mixture fraction substantially, approximately 20%. As mentioned in last section, hydrogen has a lower molecular weight and would be consumed quickly by the oxidizer due to its LFL and high flame speed. Therefore, mixture fraction decreases as a consequence when hydrogen composition increases in the fuel side.

The mixing rate can be characterized by the scalar dissipation rate, which is related to the strain rate [131]. Therefore, the strain rate shows a crucial measure of the mixing rate. The strain rate is defined as:

$$S = \sqrt{\frac{\partial v_x}{\partial X} \left(\frac{\partial v_x}{\partial X} + \frac{\partial v_x}{\partial X} \right) + \frac{\partial v_x}{\partial R} \left(\frac{\partial v_x}{\partial R} + \frac{\partial v_R}{\partial R} \right) + \frac{\partial v_R}{\partial X} \left(\frac{\partial v_R}{\partial X} + \frac{\partial v_x}{\partial R} \right) + \frac{\partial v_R}{\partial R} \left(\frac{\partial v_R}{\partial R} + \frac{\partial v_R}{\partial R} \right)} \quad (5.21)$$

As shown in Figure 5.12, the radial velocity and strain rate decreases. According to previous studies [152, 153], the variation of the stoichiometric mixture fraction f_{st} is attributed to the changing value of the strain rate. Table 5.2 shows the calculated stoichiometric mixture fraction with the changing hydrogen composition. From Table 5.2, the elevation of hydrogen concentration decreases f_{st} , which consequently results in the reduction of strain rate and radial velocity. Figure 5.12 and Table 5.2 indicate that hydrogen addition reduces the radial velocity, strain rate as well as mixing in the bluff-body burner due to the change of stoichiometric mixture fraction f_{st} .

Figure 5.13 shows the temperature and NO mass fraction distributions with varying mixture fraction at $X/D_j = 20$. The axis for temperature is on the left and NO mass fraction is on the opposite side. Both temperature and NO mass fraction achieve their maximum values near the stoichiometric mixture fraction f_{st} . Changing f_{st} by varying the dilution of the oxidizer and fuel streams shifts the location of the maxima. Many studies have been conducted based on the effects

of hydrogen addition on hydrocarbon flames and it was found that the relatively high concentration of hydrogen would cause an elevation of combustion temperature, which favors NO production [30]. However, previous studies [31, 61] also showed that the elevation of hydrogen could cause dramatic reduction in NO emission in n-heptane and H₂/air flames because soot formation did not exist and local mixing did not have a significant effect on the temperature increase.

In Figure 5.13, it can be seen that hydrogen addition does not contribute significantly to temperature changes, where the mean value is less than 5%. One possible explanation is that the increase of hydrogen raises the H₂O concentration and therefore temperature does not substantially increase due to the high specific heat of H₂O. The other possible reason is that although hydrogen addition might increase the burning temperature, the reduction of strain rate by hydrogen decreases the mixing intensity which obstructs the increase of temperatures.

Also different from previous studies of hydrogen addition on NO emission in methane/H₂ flames, hydrogen decreases NO mass fraction in Figure 5.13. Since temperature distribution does not change, the increase of steam generation and the decrease of strain rate become two major factors in NO emission reduction. Steam generated by hydrogen has a high specific heat which reduces thermal NO effectively. Hydrogen addition consequently decreases NO emission. In addition, according to Naha et al. [61], for the region where $\chi_{H_2} < 0.5$, NO_x characteristics are strongly affected by changes in equivalence ratio and strain rate, while in the second regime ($\chi_{H_2} > 0.5$), they exhibit a relatively weak dependence on equivalence ratio and strain rate. The reduction of NO emission with increasing hydrogen in Figure 5.13 is consistent with the decrease of strain rate in Figure 5.12, which demonstrates that NO emission is quite sensitive to strain rate. Therefore, the increase of hydrogen concentration decreases mixture fraction and strain rate as well as NO emission, but does not contribute to a substantial increase of temperature. These are different from

previous studies [29-31] of the combustion and pollutant emission characteristics on the CH₄/H₂ flames. In hydrocarbon flames, additional hydrogen increased the flame temperature by preventing soot formation, resulting in an increase in NO formation [31]. Unlike hydrocarbon flames, however, in the syngas flame, soot formation does not exist and therefore additional hydrogen does not show significant changes in the flame temperature. Since hydrogen contributes to a higher flame speed, a shorter, intense syngas flame is produced and, consequently reduces the residence time and NO formation [31].

The effects of nonflammable fuel-side diluents N₂, CO₂ and H₂O are shown in Figure 5.14. Three cases (case 2, 5 and 6) with different diluent compositions but the same fuel concentration are tested (see Table 5.2). The effectiveness of these tested diluents is characterized in terms of their ability to reduce NO mass fraction.

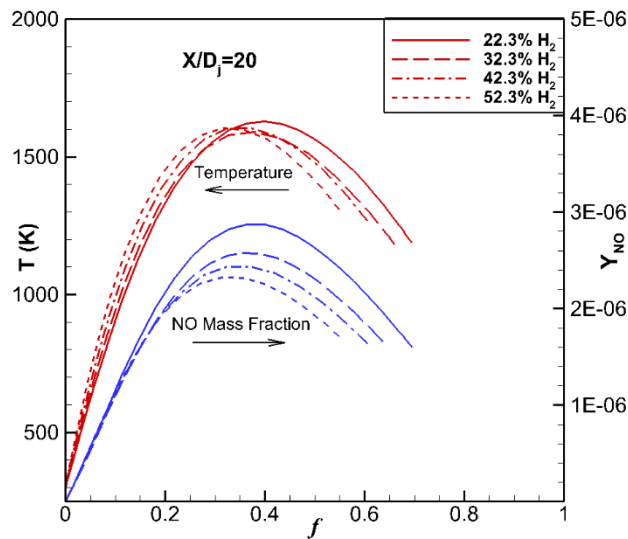


Figure 5.13 Profiles of temperature and NO mass fraction versus mixture fraction at $X/D_j = 20$

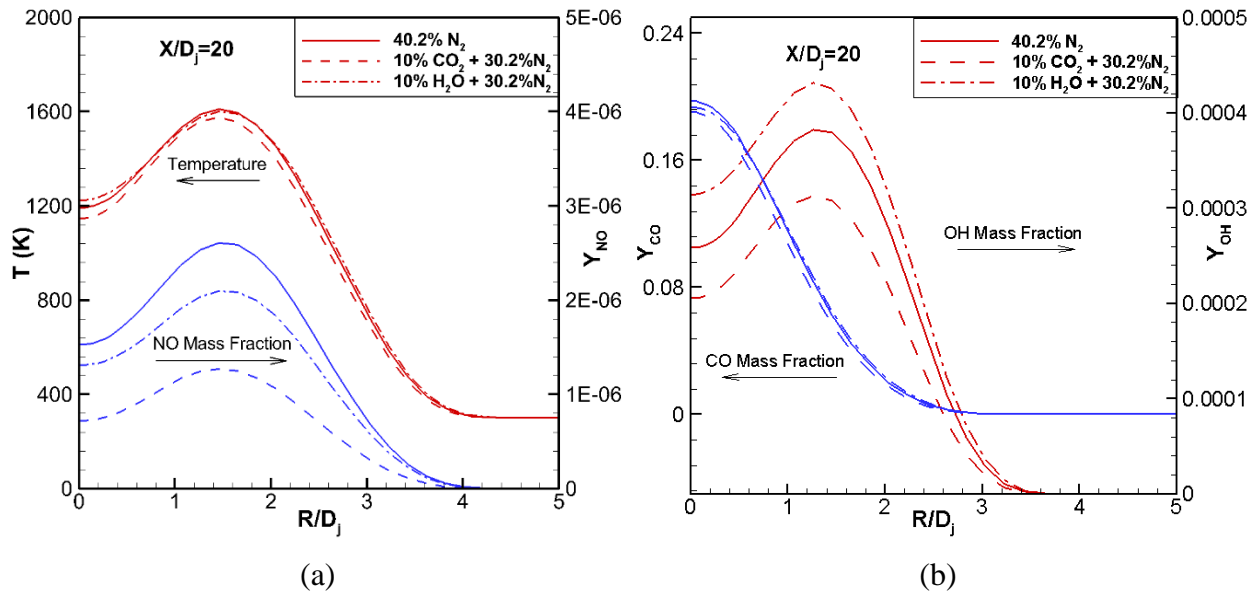


Figure 5.14 Radial profiles at $X/D_j = 20$: (a) temperature and NO mass fraction; (b) OH and CO mass fraction

Figure 5.14 (a) shows radial profiles of temperature (left axis) and NO mass fraction (right axis) of the three cases: 40.2% N_2 , 10% $CO_2 + 30.2\% N_2$ and 10% $H_2O + 30.2\% N_2$. Unlike Figure 5.13, the change of diluent mixtures does not change the location of the maxima for temperature and NO mass fraction because f_{st} is more dependent on the fuel and oxidizer mixtures. The compositions of diluents do not show their influence on radial temperature distribution to a great extent, though the temperature profile with the addition of CO_2 reduces slightly. However, they show significant changes of NO mass fraction in Figure 5.14. The addition of CO_2 shown as short dash line is the most effective to reduce NO emission, and H_2O addition shown as dash dot line is more effective than N_2 reactant. Thermal NO as one major part of NO_x generation is highly temperature dependent and recognized as the most relevant source when combusting syngas. Both radial NO distribution profiles and temperature achieve their maximum values at the same radial distance, around $R/D_j = 1.5$, which demonstrates NO is quite sensitive to temperature. However,

temperature profiles for three diluent mixtures have similar distribution and magnitude, which means that temperature is not the only main factor affects NO emission.

To illustrate the reasons of the effectiveness of CO₂ and H₂O to reduce NO emission, CO and OH radical mass fraction distributions along radial distance are plotted in Figure 5.14 (b). CO mass fraction profile uses left axis while OH radical distribution is on the opposite axis. CO is not a factor because its mass fraction does not change much for three diluents mixtures while OH is the main factor that OH radical is affected greatly by diluent compositions. According to Zhao et al. [154], the increase in the OH concentration could result in the increase in NO_x emission. CO₂ diluent shows the lowest value of reduction of OH radical, which makes CO₂ the most effective diluent to reduce NO emission in three tested cases. Although H₂O addition increases OH radical, it greatly reduces O radical through the reaction $O + H_2O \leftrightarrow 2OH$, which slows down the rate-limiting step of NO generation in Eq. (5.12).

5.6. Conclusions

The CFD models have been applied in the other bluff-body flame, namely the Dally et al. flame. Due to the detailed information and database from the experimental measurements, experimental uncertainty estimate has been firstly conducted and discussed. The method from ASME has been found most suitable to estimate the experimental uncertainty. The radial profiles and comparison of mixture fraction and temperature with the experimental data have shown and demonstrated good performance of the established CFD model in different bluff-body flame. In this chapter, the profiles of NO emission along with the mixture fraction have shown that the CFD model captured close trend and distribution of NO from the experimental work. The profiles of NO have also shown similar trend as temperature profiles indicating strong correlation with temperature.

For the study of fuel and diluent mixtures, the influences of hydrogen addition and non-flammable diluents in syngas flames have been analyzed and studied. The effects of hydrogen addition with its composition changed from 22.3% to 52.3% were tested. Also, three different diluent mixtures: 40.2%N₂, 10%CO₂+30.2%N₂ and 10%H₂O+30.2%N₂ were tested to study the effects of non-flammable but fuel-side diluents on the flame and pollutant emission characteristics. The elevation of hydrogen decreased the mixture fraction, radial velocity and strain rate because of the changes of stoichiometric mixture fraction f_{st} . Temperature distribution remains quite stable in magnitude but the location of the maxima changed with increasing hydrogen. Due to the reduction of strain rate and elevation of generated steam, NO emission was decreased by hydrogen addition. Moreover, CO₂ addition in diluent mixtures was found the most effective to reduce NO emission. OH radical that favors NO_x emission could be reduced by adding fuel-side CO₂ diluent. Although H₂O provides the most OH radicals, it is also effective in reducing NO emission due to the reduction of O radical. Therefore, hydrogen could be used as one useful fuel addition to reduce the pollutant emission of NO in the non-premixed syngas flames. In addition, CO₂ and H₂O are effective diluents to reduce pollutant emission, which is important for industrial applications.

Chapter 6. Chemical reactor network analysis for combustion systems modeling

6.1. Introduction

The objective of the current study is to conduct a thorough analysis with other chemistry representation methods, including the study of the chemical reactor network and a set of reduced reaction mechanisms. The model of reactor network and method of reaction reduction have been generated and optimized in terms of accuracy, computational time as well as internal chemical kinetics in the bluff-body reactor. Previous work with the PDF method showed that the application of the PDF method in CFD can give accurate temperature and mixture fraction predictions with small computer time requirements. However, as mentioned in Chapter 2, a better understanding of chemical kinetics with accurate emissions formation is essential, which can hardly be provided based on a simple chemical mechanism of NO_x with the PDF equilibrium method [94]. The previous CFD study of NO (Section 5.4 and 5.5) has provided some valuable information; however, the NO was calculated by post-processing the results of temperature and species, which are not sufficiently accurate, as shown in Figure 5.10. In addition, solving the complete chemical kinetics mechanism using CFD is not practical since hundreds of species and reactions would be involved. Therefore, the current study is necessary to discuss other options of chemical modeling methods.

The CRN is constructed and generated based on the flow fields and flame patterns from CFD results to capture the chemical processes. Species and pollutants such as NO_x can be predicted using the detailed chemical kinetic reaction database of GRI-Mech 3.0 [91]. The development of the CRN includes three procedures:

- (a) Build a CRN structure based on the basic flow and combustion profiles in a CFD simulation.
- (b) Extract CFD information of each elemental reactor, such as volume and input flow rates based on CRN structure and feed the pre-processed CFD results into the reactors of the CRN model.

(c) Perform the actual chemical kinetic simulation of the detailed gas phase chemistry in the CRN model.

An example of the mapping and the network connections of a typical bluff-body burner is shown in Figure 6.1, which consists of recirculation, flame and post-flame zones. In Figure 6.1, the recirculation zone mixes fuel and air streams and directly connects to the flame zones with hot combusted gas. Each of the zones will be characterized by the physical properties of the flow and the flame behavior [155].

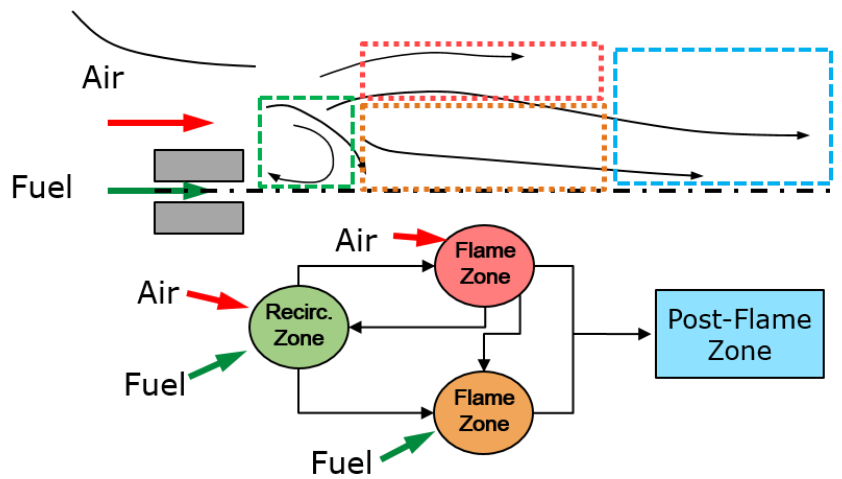


Figure 6.1 Schematic of a bluff body burner and its zones network [156]

6.2. Reactor models in CRN approach

The CRN method is based on dividing the combustion area into smaller regions where physical and chemical characteristic variations are small. Each region can be replaced by an elemental chemical reactor. The characteristic of each reactor and its connections with other reactors depend on the flow field. An elemental chemical reactor can be represented as perfectly stirred reactor

(PSR), post-flame reactor (PFR) and non-reactant mixer (MIX), depending on the flow and reaction behaviors.

6.2.1. Perfectly stirred reactor (PSR)

The perfectly stirred reactor is a zero-dimensional ideal reactor where mixing at the molecular scale is assumed to happen instantaneously compared to chemical reactions. Variables like temperature and species composition are assumed the same at the exit of the reactor, due to the assumption of perfect mixture of fuel and air inside the PSR [157]. In a PSR, the combustion process takes place in a control volume and substitute for a strong turbulent mixing intensity (Figure 6.2). The equations of species, mass and energy conservation are shown as:

- Species concentration: $Y_i = Y_{i,outlet}$ (6.1)

- Mass conservation: $\dot{\omega}_i MW_i V + \dot{m}(Y_{i,inlet} - Y_{i,outlet}) = 0$ (6.2)

- Energy conservation: $\frac{1}{\tau} \sum_{i=1}^N (Y_i h_i - Y_{i,inlet} h_{i,inlet}) + \sum_{i=1}^N \frac{h_i \dot{\omega}_i MW_i}{\rho} + \frac{\dot{Q}}{\rho V} = 0$ (6.3)

where $\dot{\omega}_i$ is the net chemical production rate of species i ; MW_i is the molecular weight of each species i ; V is the given volume of the PSR; \dot{m} is the mass flow rate; τ is the residence time with the function of $\tau = \rho V / \dot{m}$; h is the molar enthalpy and \dot{Q} is the net of energy generation.

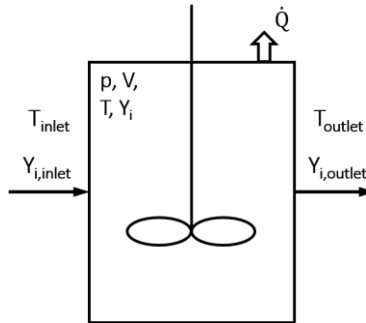


Figure 6.2 Perfectly stirred reactor and its parameters

6.2.2. Plug-flow reactor (PFR)

The plug-flow reactor is a reactor where the flow is assumed to move as a plug and the chemical reaction proceeds one-dimensionally (Figure 6.3). In this reactor, the flow properties change in the axial direction while remaining uniform in the radial direction [158]. Therefore, the mixing in the axial direction is assumed to be zero. The equations of species conservation and energy in the PFR are [157]:

- Position-dependent species mass concentration: $\rho u \frac{dY_i}{dx} = \dot{\omega}_i MW_i$ (6.4)

- Energy conservation: $\rho c_p u \frac{dT}{dx} + \sum_{i=1}^N h_i \dot{\omega}_i MW_i = 0$ (6.5)

where c_p is the specific heat defined as $c_p = \sum_{i=1}^N Y_i c_{p,i}$.

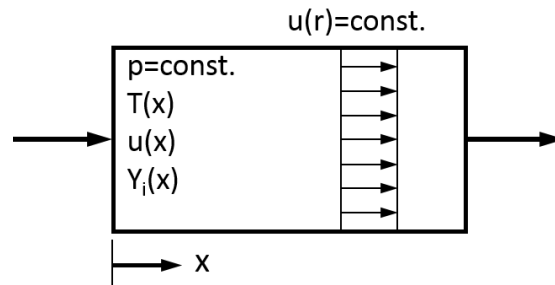


Figure 6.3 Plug-flow reactor and its parameters

6.2.3. Non-reactant mixer

The non-reactant mixer is a reactor where the entering streams are uniformly mixed without chemical reactions (Figure 6.4). Mass and energy conservation can be easily expressed as:

- Species mass concentration: $\dot{m}_3 = \dot{m}_1 + \dot{m}_2$ (6.6)

- Energy conservation: $\sum_{i=1}^N (\dot{m}_3 h_{i,3}) = \sum_{k=1}^N (\dot{m}_1 h_{k,1}) + \sum_{i=1}^N (\dot{m}_2 h_{i,2})$ (6.7)

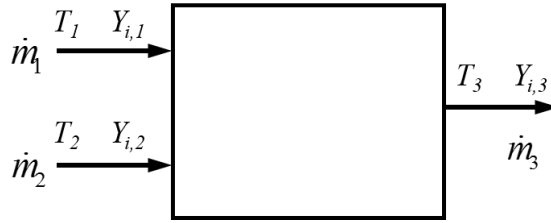


Figure 6.4 Non-reactant mixer and its parameters

6.3. CRN model for the non-premixed flames

With the validated CFD results of Correa and Gulati [16] flame and Dally et al. [134] flame, CRN model is created and compared with the CFD results at the exit of the flames. The element reactors in the CRN are designed and generated based on the CFD results of temperature and flow patterns calculated based on chemical equilibrium.

Figure 6.5 shows the contour of temperature and streamlines from the CFD results of the Correa and Gulati flame. Similar to Figure 4.7(b), the region of the contour is scaled to the fuel jet diameter D_j and enlarged along the radial direction to 6 times D_j . Since the CFD modeling of the bluff-body burner is conducted in a 2D axisymmetric domain, the 2D flame structure is symmetric to the centerline of the burner, and is mirrored to show the flame regions (upper half) and the streamlines (lower half). The design of the reactors is based on the flame structure, the flow pattern and entrainment of air and gas in the recirculation and flame region. The main flame region is specified based on the shape of the flame and the boundary is determined when the temperature gradient is close to 0. In the main flame region, three element CRN reactors, namely FLAME.1, FLAME.2 and FLAME.3 are specified to divided the main flame region to improve the predictive accuracy. The recirculation region named RECIR. is created based on the size of the recirculation of the flow.

The element named MIX represents the region where rest of the air enters into the system as a co-annual flow surrounding the bluff body (not shown in the figure). The element named

FLAME.4 represents a region that has both flame products from FLAME.3 and remaining air from MIX since the streamline becomes more horizontal with less change in the radial direction. Following the FLAME.4 is a POST-FLAME region, where the flow is assumed to move as a plug and the flow properties only change in axial direction while remaining uniform in the radial direction.

The CFD results of Dally et al. flame and the CRN reactor arrangements are shown and specified in Figure 6.6. Similar to the Correa and Gulati flame, a recirculation zone persists downstream of the bluff-body wall. Note that the size of each reactor region in Figure 6.6 is different from Figure 6.5 based on the flame characteristics. Regions for FLAME.1, FLAME.2 and FLAME.3 are specified based on the flame shape and the region named MIX that includes the remaining air entering into the system. FLAME.4 mixes the air from MIX and the products from FLAME.3. The region for POST-FLAME is specified as the last reactor in the system, where the flow is assumed to be more uniform in the axial direction.

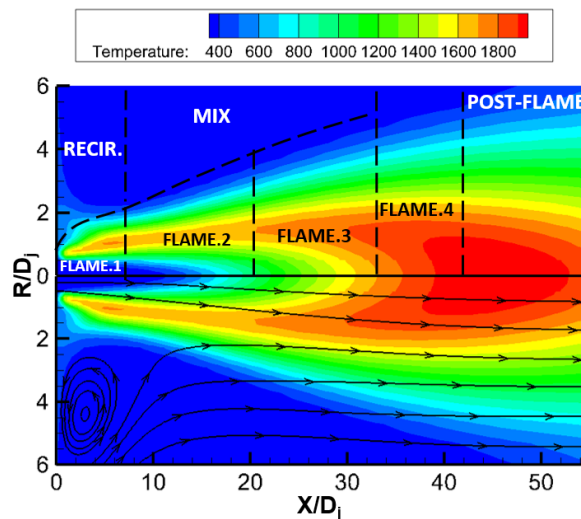


Figure 6.5 Temperature contours of CFD predictions of the Correa and Gulati flame; the upper half identifies key flame regions and the lower half shows the streamlines

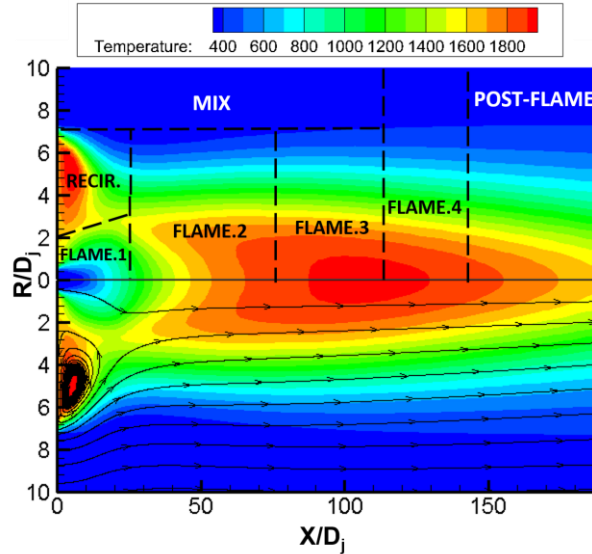


Figure 6.6 Temperature contours of CFD predictions of the Dally et al. flame; the upper half identifies key flame regions and the lower half shows the streamlines

The chemical reactor code, CHEMKIN [159] employing the detailed gaseous reaction mechanism GRI-Mech 3.0 [91] is used in present work of the reactor network development. Codes like CHEMKIN show great ability to link the flow elements to a network yet are also able to handle the large chemical kinetic mechanisms. Figure 6.7 shows the detailed reactors and the 8-element network with flow paths. Each elemental reactor and the corresponding network have been introduced in detail in Figure 6.5 and Figure 6.6. Figure 6.7 depicts the schematic framework of the CRN model. Fuel and a very small portion of air enters FLAME.1, while a larger portion of air enters the recirculation zone as the secondary air. In the RECIR. zone, the air stream changes the velocity direction and intensively mixes the air and some unburned fuel and products. The amount of extra air that does not come from the products in the RECIR. and FLAME. 2 zones but directly enter into the FLAME. 3 region has been specified. The mixed products from FLAME.1 and RECIR. enter the FLAME.2 zone and provide a better mixture of fuel and air with increased temperatures. Therefore, FLAME.2 reaches a higher temperature than FLAME.1 due to the heated

and mixed gases from RECIR, and up to 98% products from FLAME.2 enters into FLAME.3 to combust unburned products. A very small portion 2% of the products from FLAME.2 recycles back to RECIR. zone to adjust the species that can come back to RECIR. zone due to the recirculation of the flow [155]. The majority of air enters the MIX zone as cold excess air and then enters FLAME.4 to combust the remaining fuel or re-burned products. POST-FLAME follows the FLAME.4 zone with uniform concentration and velocity along the radial direction and gases exit the burner at the end of the POST-FLAME zone.

The CRN is modeled by adjusting the volumes of each flame region, temperature and input flow rates of each elementary reactor as well as the distribution of the flow between each reactor. With the arrangement of reactors shown in Figure 6.5 and Figure 6.6, the input flow rates and volume of each region can be easily calculated based on CFD results. Detailed information of volume and input flow rates and the flow splits in each reactor have been shown in Table 6.1, where the upper part is the information for the Correa and Gulati flame and lower part is the information for the Dally et al. flame. Regions like FLAME.1, RECIR, FLAME.2 and FLAME.3 have relatively smaller volumetric percentages due to the design of the PSR model where molecular-scale mixing is instantaneous compared to chemical reactions.

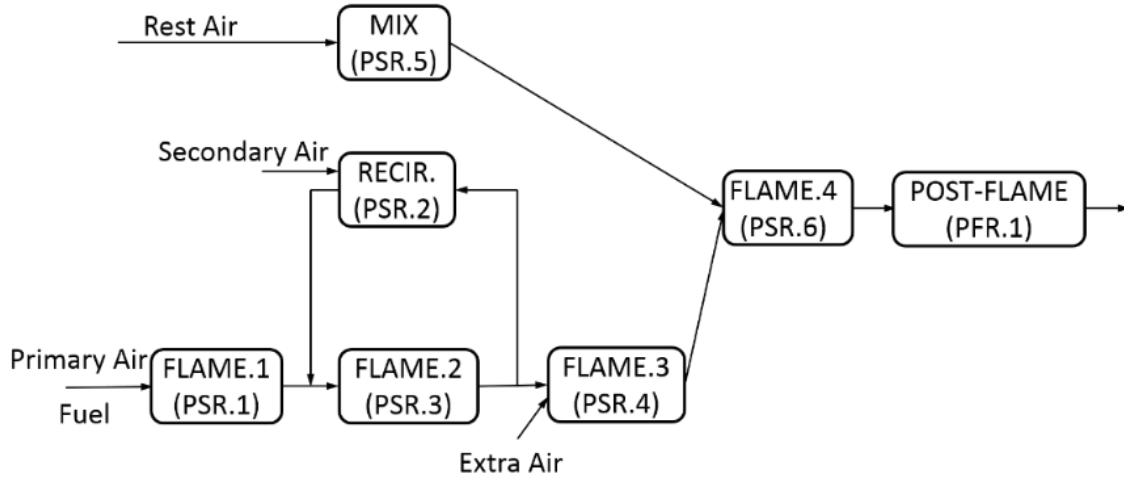


Figure 6.7 Schematic of the CRN model

Table 6.1 Volumetric inputs in the CRN models for Correa and Gulati and Dally et al. burners

	Element	FLAME.1	RECIR	FLAME.2	FLAME.3	MIX.	FLAME.4	POST-FLAME
Correa and Gulati Burner	Volume %	0.02	1.10	0.09	1.40	54.78	18.2	24.41
	Streams	Fuel + Primary air	Secondary air		Extra air	Remaining air		
	Flow rate cm ³ /s	Fuel: 635 Primary air: 100	24,650		27,078	55,708		
Dally et al. Burner	Element	FLAME.1	RECIR	FLAME.2	FLAME.3	MIX.	FLAME.4	POST-FLAME
	Volume %	0.01	0.09	0.10	0.31	55.47	21.35	22.67
	Streams	Fuel + Primary air	Secondary air		Extra air	Remaining air		
	Flow rate cm ³ /s	Fuel: 1201 Primary air: 100	159,541		196,245	249,250		

6.4. CRN Results of temperature and species

To test the performance and validate the CRN model, outputs like mean temperature and species mass fraction are compared between the CFD and the CRN results at the exit of the bluff-body burners, shown in Table 6.2. CRN results for each bluff-body flame closely match the CFD emission and temperature output with maximum relative errors as low as 5%.

Table 6.2 Temperature and main species at the exit of the bluff-body burners

Variables	Correa and Gulati flame	CRN	error %	Dally et al. flame	CRN	error %
T (K)	336.1	340.0	1.16	321.8	327.9	1.90
O ₂ %	20.67	20.67	0.005	20.81	20.82	0.05
N ₂ %	78.90	78.88	0.03	78.90	78.92	0.03
CO ₂ %	0.20	0.21	5.00	0.07	0.06	3.03
H ₂ O %	0.24	0.24	1.67	0.20	0.19	5.00

6.4.1. CRN results of the Correa and Gulati flame

Figure 6.8 shows the main combustion characteristics such as temperature, species and NO_x distribution for each elemental CRN reactor. Results of temperature are shown as a red line with the ordinate on the left side. Mole fraction percentages of CO₂ and H₂O and parts per million (ppm) of NO_x emission are shown on the right ordinate. In Figure 6.8, temperature greatly increases in FLAME.2 and FLAME.3 and reaches the highest value in FLAME.3. Although the bottom region of FLAME.4 has even higher temperatures based on the CFD predictions (see Figure 6.5), the design of FLAME.4 is to mix the remaining air and high temperature products, which has resulted in a lower temperature of FLAME.4 in the CRN analysis. The green line with triangles and blue line with diamonds show the mole fraction in percentage of H₂O and CO₂, respectively, and grey line with filled symbols is the pollutants NO_x distribution. In Figure 6.8, the main combustion products and NO_x show similar distribution trends to the temperature profile. H₂O% shows much higher values at the first flame region FLAME.1, which indicates that H₂ is first oxidized and quickly consumed in the beginning of combustion process. The NO_x distribution profile is a term to signify the sum of nitric oxide (NO) and nitrogen dioxide (NO₂). In Figure 6.8, NO_x increases with the increase of temperature in FLAME. 2 and FLAME.3. A significant reduction of NO_x in the MIX region occurs due to the addition of a large amount of unreacted (cold) co-annular air.

The values of NO_x then rise in the regions of FLAME.4 and POST-FLAME because of the slightly increased temperature and high concentration of NO_x from FLAME.3. Nitrous oxide (N_2O) exists as well but is not considered as a composition of NO_x , since it is an inert gas and has multiple industrial and medical applications. However, in the next section study, N_2O will be listed and shown together with NO_x to elaborate the relative reactions and the transformation of NO_x formation.

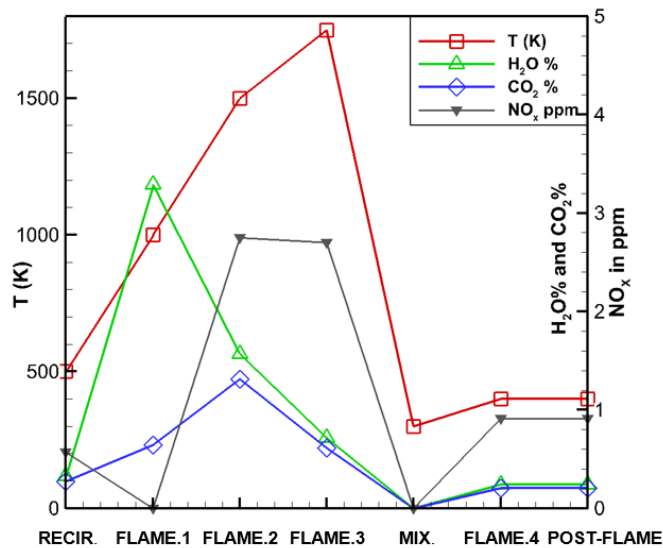


Figure 6.8 Main products transportation and pollutants distribution for Correa burner

6.4.2. CRN results of the Dally et al. flame

Figure 6.9 shows the main combustion products and NO_x distributions in the Dally et al. burner. Similar as Figure 6.8, temperature has been shown as red line in Figure 6.8 with the ordinate on the left side and other species have the ordinate shown on the right side. Different from Correa and Gulati burner, except for the high temperature regions of FLAME.2 and FLAME.3, the RECIR. region also shows a high temperature. The high temperature in the RECIR. zone is because air velocity in the Dally et al. flame is much larger than the Correa and Gulati flame, which makes the mixing downstream more intense with more fuel involved. The temperature of FLAME.4 greatly

reduces because a large amount of unreacted (cold) co-annular air has been added from MIX zone. Similar to Correa and Gulati flame, main products and NO_x pollutants increase with flame temperature. However, the values of $\text{CO}_2\%$ and $\text{H}_2\text{O}\%$ are smaller than Correa and Gulati flame, since much larger annular flow of air is involved in Dally et al. flame. Similar as Figure 6.8, NO_x increases with the increase of temperature. Comparing the CRN results for both burners, they share some commonalities because the nature of the bluff-body flames. However, there are still some differences due to the fuel composition, fuel-air velocity ratio and other experimental operating conditions.

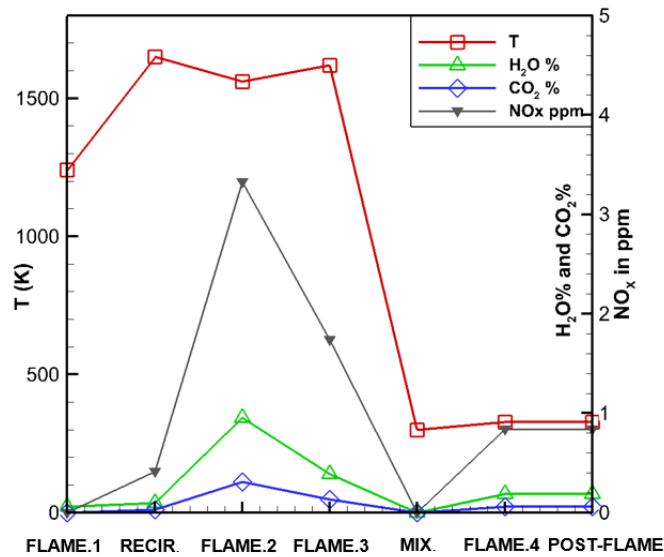


Figure 6.9 Main products transportation and pollutants distribution for Dally burner

6.5. Reactions of NO_x formation

The GRI-Mech 3.0 [91] includes more than 105 reactions that are involved in NO_x formation. In this section, the NO_x emission and 105 NO_x involved reactions are characterized by rate of production (ROP). The NO_x ROP is calculated from the NO_x emissions and the reactor residence time t , which can be written as $ROP_{\text{NO}_x} = d[\text{NO}_x]/dt$. Rate of production analysis can provide

complementary information on the direct contributions of individual reactions to species net production rates.

The distributions and ROP of NO_x composition (NO and NO_2) and N_2O are plotted in in Figure 6.10 for the Correa and Gulati flame. In Figure 6.10 (a), the distributions of NO , N_2O and NO_2 show similar trends as the total NO_x distribution in Figure 6.8, where the values are higher in FLAME.2 and FLAME.3 with increased temperature. The ROP profiles of NO , N_2O and NO_2 are plotted in Figure 6.10 (b) to show the rate change for each species. In the regions of RECIR, FLAME.2 and FLAME.4, the ROPs of some pollutant species sharply change, which means the rate of NO_x is significantly changed at high temperature or high concentration of N_2 since the formation of NO_x needs the breaking of the strong N_2 triple bond.

Therefore, in the regions where the absolute ROP values are relatively high, the reactions with large contributions to the ROP values for NO , NO_2 and N_2O have been listed and compared in Figure 6.11 and Figure 6.12. The plotted positions and corresponding species have also been marked in Figure 6.10 (b).

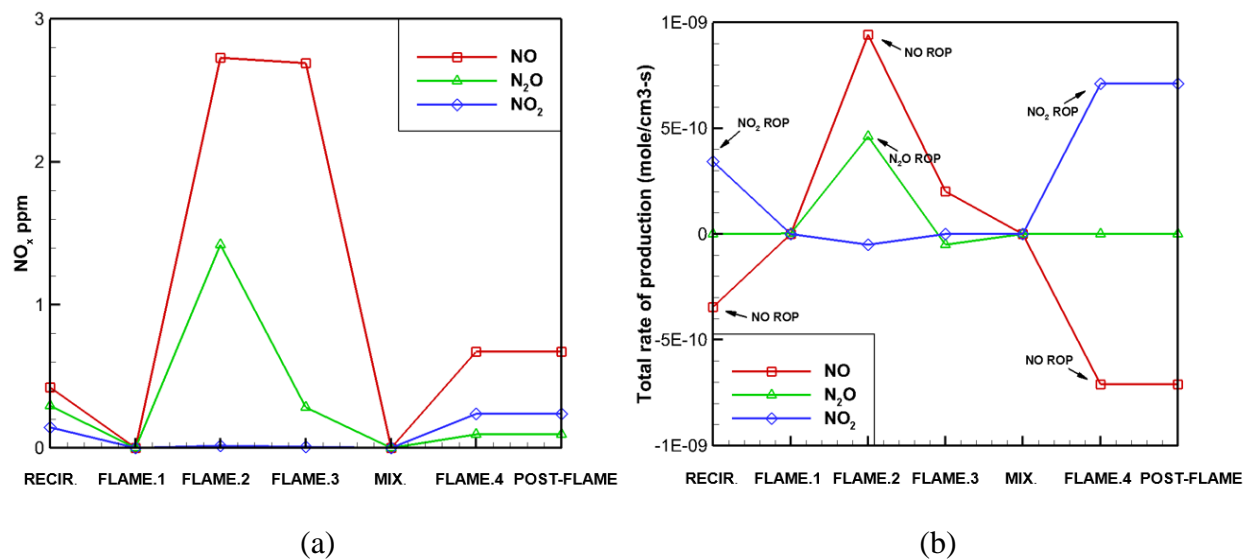
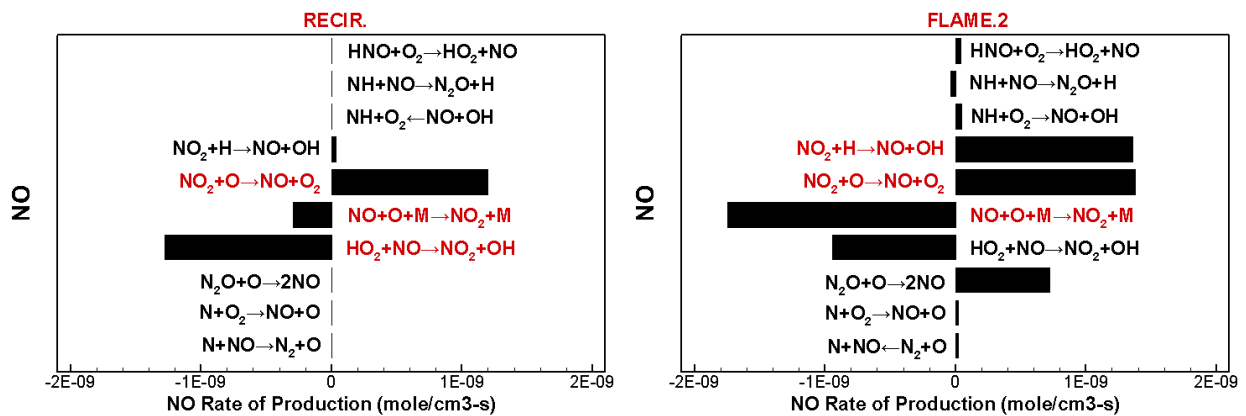


Figure 6.10 CRN distribution and rate of production for Dally flame: (a) distribution of NO , N_2O and NO_2 ; (b) total rate of production each species

Figure 6.11 shows the reactions that contribute to a significant increase or decrease of NO ROP. Clearly, in Figure 6.11, the reactions in the middle have shown more important contributions to the rate of production of NO product. The sign of ROP decides the direction of the reactions. For example, the positive sign of NO ROP indicates that NO is being produced and refers to the direction of the reaction generating NO. From the zone of RECIR. to FLAME.4, the change of the contributing reactions can be clearly observed. For example, comparing the results between RECIR. and FLAME.2, the ROP of reaction $\text{NO}_2 + \text{H} \rightarrow \text{NO} + \text{OH}$ increases significantly with more H radicals from the reactions of fuel H_2 . At high temperatures, usually above 1800 K, oxygen in the combustion air would disassociate into its atomic state and participate in the NO related reaction, which explains that the reactions involving atomic oxygen increase the corresponding ROP values in FLAME.2 (such as $\text{NO}_2 + \text{O} \rightarrow \text{NO} + \text{O}_2$ and $\text{NO} + \text{O} + \text{M} \rightarrow \text{NO}_2 + \text{M}$). In the reaction of $\text{NO} + \text{O} + \text{M} \rightarrow \text{NO}_2 + \text{M}$, nitrogen dioxide forms in the reaction with atomic oxygen as the three body reaction, where the third body M could be any inert molecule (such as Ar, N_2).



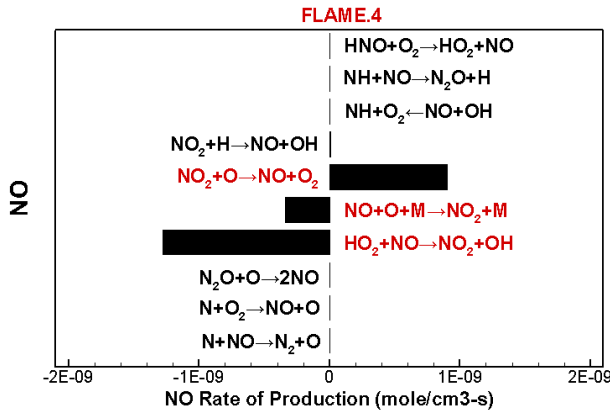


Figure 6.11 Reactions with high ROP of NO in the region of RECIR., FLAME.2 and FLAME.4

Figure 6.12 shows the reactions for NO₂ (top two figures) in the regions of RECIR. and FLAME.4 and reactions for N₂O (bottom figure) in FLAME.2. The major reaction of NO₂ formation is with the hydroperoxide radical HO₂, such that the reaction of HO₂ + NO → NO + OH presents high ROP values in Figure 6.12 and HO₂ is mainly produced through H + O₂ + M → HO₂ + M. The temperature range of this reaction is less than 1000 K, which explains why it has high ROP values in both RECIR. and FLAME. 4. For the formation of N₂O, the major reaction goes to N₂O + M ← N₂ + O + M. This reaction happens in the lean flame, which corresponds to the case where more excess air exists than needed for the stoichiometric reaction. The temperature range of this chemical reaction is less than 1700 K. In addition, N₂O contributes to NO emission by chemical reactions with radical O with the reaction shown in FLAME.2 in Figure 6.11, as N₂O + O → 2NO, but the ROP value is not the highest in FLAME.2.

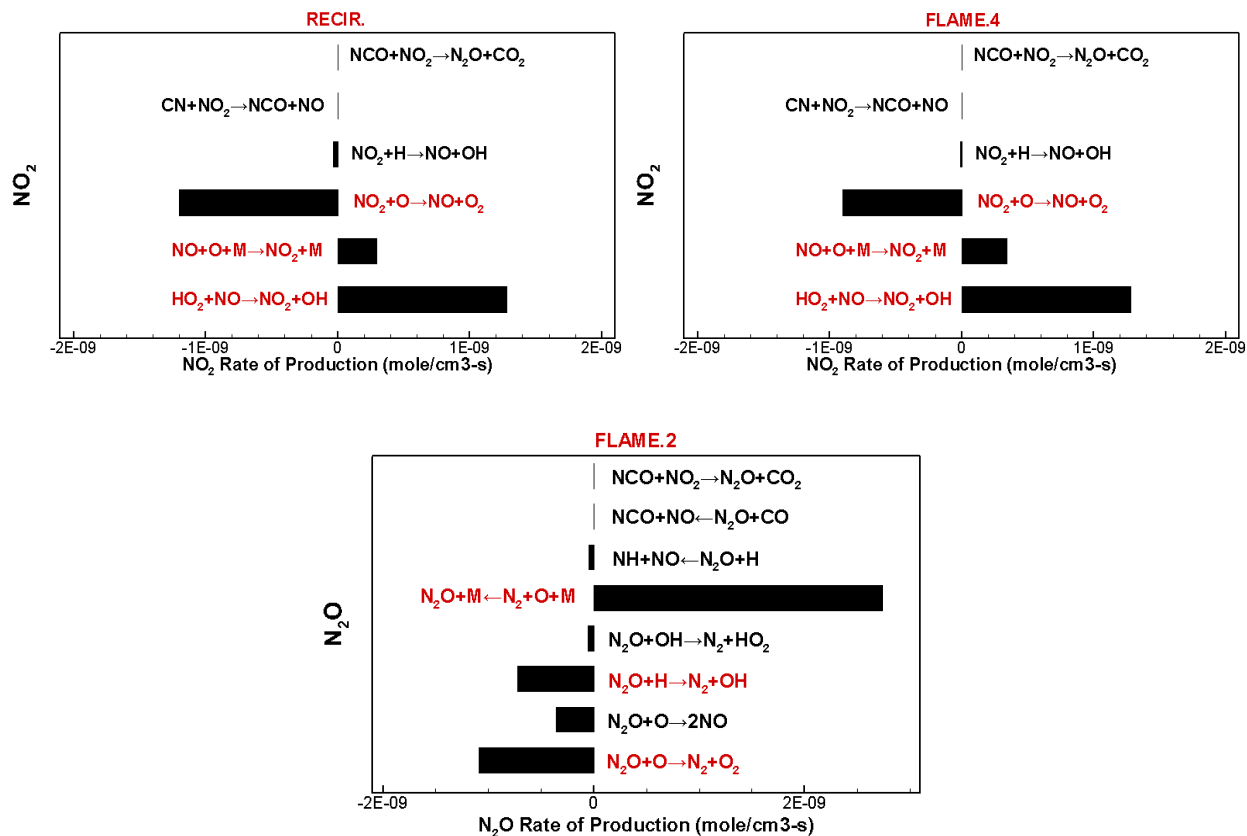


Figure 6.12 Reactions with high ROP of NO₂ (top figures) and N₂O (bottom) in the region of RECIR., FLAME.2 and FLAME.4

For the Dally et al. flame, the distribution and total rate of production values of NO, NO₂ and N₂O have been plotted in Figure 6.13. Similarly, NO and N₂O increases with the increase of temperature while NO₂ is much smaller in the NO_x. Figure 6.13 (b) shows the rate of production of three species found in FLAME.2 and FLAME.4, where the absolute ROP values are much higher than the rest. Therefore, the reactions that have high absolute ROP values of each species have been plotted in Figure 6.14 and Figure 6.15. Comparing with the results from Correa and Gulati flame, the reactions with high ROP are quite similar.

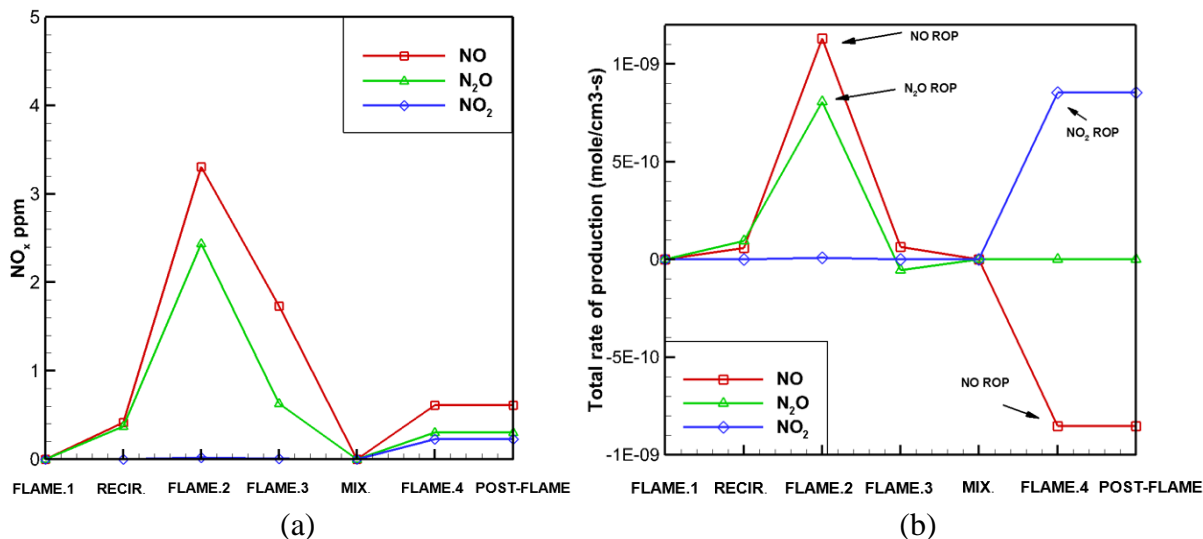


Figure 6.13 CRN distribution and rate of production for Correa and Gulati flame: (a) distribution of NO, N₂O and NO₂; (b) total rate of production each species

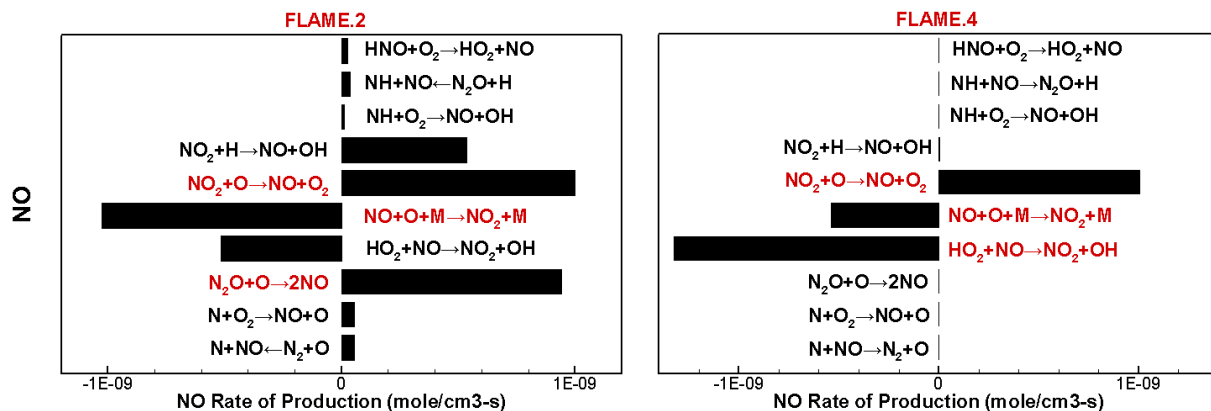


Figure 6.14 Reactions with high ROP of NO in the region of FLAME.2 and FLAME.4

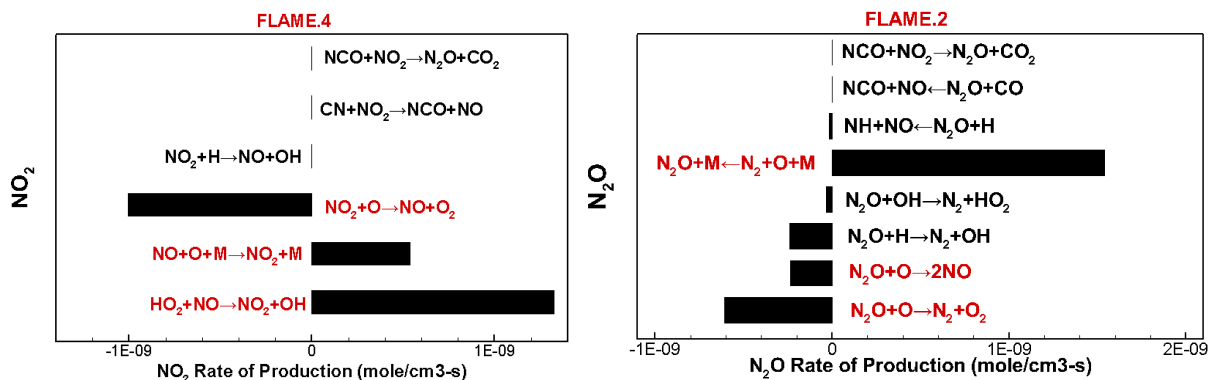


Figure 6.15 Reactions with high ROP of NO₂ (left) and N₂O (right) in the region of FLAME.2 and FLAME.4

6.6. Mechanism reduction based on sensitivity analysis of CRN

The objective of this section is to conduct a sensitivity analysis on the Correa and Gulati flame predictions and generate the reduced chemical mechanism from hundreds of species and reactions in GRI-Mech 3.0[91]. As mentioned in Section 2.5, sensitivity analysis can reveal which are the main control parameters and which are the indirect and influential parameters. A local sensitivity calculation can help to determine quantitatively the dependence of a solution (i.e., species concentration and temperature) on certain parameters (i.e., reaction rate coefficient) and reactions with high sensitivities can be considered to be identical to the rate limiting steps [111].

In this section, the sensitivity of species to the various reactions constants from the Arrhenius equations has been calculated. The normalized sensitivity coefficient can be expressed as

$$S_i = \frac{\partial \ln c_i}{\partial \ln \kappa_j} = \frac{\kappa_j}{c_i} \frac{\partial c_i}{\partial \kappa_j} \quad (6.8)$$

The normalized sensitivity coefficients represent the fraction change of species concentration c_i caused by rate coefficient κ_j , which can be referred to Eq. (3.31). i represents species and j represents the reactions.

The normalized sensitivity coefficients of fuels (H_2 and CO) and products (H_2O and CO_2) have been calculated among the detailed reactions in the GRI-Mech 3.0. A reaction is redundant if its absolute sensitivity coefficient is small with respect to each species of the reaction system [160]. According to the rate-limiting definition from Ray [161], a reaction is rate-limiting if the increase of its reaction rate coefficient causes a significant change in the overall species concentration.

Table 6.3 shows the sensitivity of H_2 concentration with respect to the rate coefficient. In the following results, reactions with high absolute sensitivities in the element-reactor zones are listed and considered as determinant steps. The positive or negative sign of the normalized sensitivity coefficient helps to decide the direction of the reactions. For example, for the H_2 sensitivity study

shown in Table 6.3, reactions with high negative sensitivity coefficient contribute to the consumption of H₂ such as reactions OH + H₂ → H + H₂O and O + H₂ → H + OH, while the high positive coefficient indicates that the reactions slow down the oxidation of H₂ such as the reaction H + HO₂ → O₂ + H₂. In the induction part of the reactions, the most important event is the accumulation of radicals [111]. Therefore, species are all sensitive to important radical reactions, with positive sensitivity coefficient for radical producing and negative sensitivity coefficient for radical consuming reactions. For example, for the H₂ sensitivity study shown in Table 6.3, reaction like H + O₂ → O + OH that consumes atomic hydrogen have shown high negative coefficient. The three-body reaction of H + O₂ + M → HO₂ + M with the third body of CO₂/N₂/Ar has negative coefficients in FLAME.3 and 4 zones meaning that the atomic hydrogen is consumed. It has positive values in RECIR. and FLAME. 2 zones, which indicates that the consumption of atomic hydrogen has been slowed down in these reactor zones.

Table 6.3 Sensitivity of H₂ with respect to the rate coefficients

Flame Zone	Reactions	Sensitivity coefficient
RECIR.	OH + H ₂ → H + H ₂ O	-0.603
	O + H ₂ → H + OH	-0.190
	H + O ₂ → O + OH	-0.163
	H + O ₂ + M ← HO ₂ + M	0.120
	H + HO ₂ → O ₂ + H ₂	0.124
FLAME.1	H + O ₂ → O + OH	-0.222
	H + HO ₂ → O ₂ + H ₂	0.150
FLAME.2	OH + H ₂ → H + H ₂ O	-0.535
	O + H ₂ → H + OH	-0.190
	H + O ₂ → O + OH	-0.187
	H + HO ₂ → O ₂ + H ₂	0.123
	H + O ₂ + M ← HO ₂ + M	0.117
FLAME.3	H + O ₂ + M → HO ₂ + M	-0.134
FLAME.4	H + O ₂ + M → HO ₂ + M	-0.136

Similarly, the sensitivity coefficients of CO, H₂O and CO₂ with respect to the rate coefficients are listed in Table 6.4 to Table 6.6 and the signs of the sensitivity coefficients are used to decide the directions of the related reactions. For instance, for the CO sensitivity study shown in Table 6.4, reaction of OH + CO → H + CO₂ has high negative coefficients in all the listed regions, indicating that this reaction contributes to the production of CO₂ from CO consumption. Similarly, in Table 6.5, reactions with high positive coefficients like OH + CO → H + CO₂ and HO₂ + CO → OH + CO₂ contribute to the generation of CO₂ while the negative coefficient from HCO + M → H + CO + M indicates that the consumption of CO has been slowed down.

The reason for the significance of these reactions is clear. For example, the reaction of H + O₂ → O + OH is the most important chain branching step in every combustion process where H is present. The other most important reaction that functions similar is the reaction O + H₂ → H + OH. Both of the aforementioned reactions convert O₂ and H₂ to two OH radicals and therefore accelerate combustion processes. In Table 6.3, several reactor zones have the same reaction with high absolute sensitivity coefficients, such as OH + H₂ → H + H₂O, O + H₂ → H + OH, H + O₂ → O + OH and H + O₂ + M ← HO₂ + M, indicating their importance in the combustion process. Noticeably, OH + H₂ → H + H₂O shows a high sensitivity value of H₂ in RECIR. and FLAME.2 since it is the main reaction for the conversion of H₂ to H₂O. This is also shown in Table 6.4 where OH + CO → H + CO₂ presents with high absolute sensitivity coefficients in the major flame and recirculation zones.

Table 6.4 Sensitivity of CO with respect to the rate coefficients

Reactions	Flame Zone	Sensitivity coefficient
OH + CO → H + CO ₂	RECIR.	-1.002
	FLAME.2	-0.924
	FLAME.3	-1.431
	FLAME.4	-1.431

Table 6.5 Sensitivity of CO₂ with respect to the rate coefficients

Flame Zone	Reactions	Sensitivity coefficient
FLAME. 1	$\text{OH} + \text{CO} \rightarrow \text{H} + \text{CO}_2$	0.716
	$\text{HO}_2 + \text{CO} \rightarrow \text{OH} + \text{CO}_2$	0.229
	$\text{HCO} + \text{M} \rightarrow \text{H} + \text{CO} + \text{M}$	-0.174

Table 6.6 Sensitivity of H₂O with respect to the rate coefficients

Flame Zone	Reactions	Sensitivity coefficient
FLAME. 1	$\text{H} + \text{O}_2 \rightarrow \text{O} + \text{OH}$	1.949
	$\text{H} + \text{HO}_2 \rightarrow \text{O}_2 + \text{H}_2$	-1.310
	$\text{H} + \text{HO}_2 \rightarrow 2\text{OH}$	1.227
	$\text{H} + \text{O}_2 + \text{M} \rightarrow \text{HO}_2 + \text{M}$	-0.632

Similarly, the normalized sensitivity of NO_x (NO and NO₂) is also investigated and shown in Table 6.7 and Table 6.8. It is obvious that the main reactions for the conversion of H₂ and CO to H₂O and CO₂ also shows high sensitivity coefficient in NO_x, since temperature and radicals from the main reactions can be influential to NO_x emission. Besides the main reaction of combustion such as $\text{H} + \text{O}_2 \rightarrow \text{O} + \text{OH}$ and $\text{H} + \text{O}_2 + \text{M} \rightarrow \text{HO}_2 + \text{M}$, several NO_x related reactions also show high sensitivity values, namely $\text{N}_2 + \text{O} \rightarrow \text{N} + \text{NO}$, $\text{N}_2\text{O} + \text{O} \rightarrow 2\text{NO}$, $\text{HO}_2 + \text{NO} \rightarrow \text{NO}_2 + \text{OH}$, $\text{NO}_2 + \text{O} \rightarrow \text{NO} + \text{O}_2$. Noticeably, the reaction of $\text{N}_2 + \text{O} \rightarrow \text{N} + \text{NO}$ is significant in FLAME.3 and FLAME.4, which is also the rate-limiting step of the Zeldovich mechanism of NO formation and is employed in Fluent to post-process NO emission in Section 5.4. In FLAME.1, NO is mainly generated through reactions of $\text{N}_2 + \text{O} \rightarrow \text{NO} + \text{N}$, $\text{N} + \text{O}_2 \rightarrow \text{NO} + \text{O}$, $\text{NO}_2 + \text{H} \rightarrow \text{NO} + \text{OH}$ from the rate of production results and is mainly consumed through $\text{HO}_2 + \text{NO} \rightarrow \text{NO}_2 + \text{OH}$. However, in FLAME.1, the overall rate of production of NO ($ROP_{NO} = d[\text{NO}]/dt = 2.94E^{-13}$ mol/cm³-s) is much larger than the overall rate of production of NO₂ ($ROP_{NO_2} = d[\text{NO}_2]/dt = 3.99E^{-15}$ mol/cm³-s), which indicates that the NO₂ generation reaction is much slower than the NO generation

reactions. Therefore, the reaction of $\text{HO}_2 + \text{NO} \rightarrow \text{NO}_2 + \text{OH}$ is the rate-limiting step for NO_2 production. The reaction $\text{N}_2\text{O} + \text{O} \rightarrow 2\text{NO}$ is the biggest contribution from N_2O to NO emission, as mentioned in Section 6.5. Some NO_x related reactions shown with high sensitivity coefficients also appear in the study of rate of production, showing great impact on NO_x emission.

Table 6.7 Sensitivity of NO with respect to the rate coefficients

Flame Zone	Reactions	Sensitivity coefficient
RECIR.	$\text{H} + \text{O}_2 + \text{M} \rightarrow \text{HO}_2 + \text{M}$	-0.494
	$\text{H} + \text{O}_2 \rightarrow \text{O} + \text{OH}$	-0.260
	$\text{OH} + \text{HO}_2 \rightarrow \text{O}_2 + \text{H}_2\text{O}$	0.167
FLAME.1	$\text{H} + \text{O}_2 + \text{M} \rightarrow \text{HO}_2 + \text{M}$	-1.647
	$\text{H} + \text{O}_2 \rightarrow \text{O} + \text{OH}$	5.764
FLAME.2	$\text{H} + \text{O}_2 + \text{M} \rightarrow \text{HO}_2 + \text{M}$	0.478
FLAME.3	$\text{H} + \text{O}_2 + \text{M} \rightarrow \text{HO}_2 + \text{M}$	-0.322
	$\text{N}_2 + \text{O} \rightarrow \text{N} + \text{NO}$	0.420
FLAME.4	$\text{H} + \text{O}_2 + \text{M} \rightarrow \text{HO}_2 + \text{M}$	-0.318
	$\text{OH} + \text{HO}_2 \rightarrow \text{O}_2 + \text{H}_2\text{O}$	0.156
	$\text{N}_2 + \text{O} \rightarrow \text{N} + \text{NO}$	0.422

Based on the sensitivity results of fuels and products, the concentration of major species are sensitive to the rate of reactions that are important for the radicals. The sensitivity study of H_2 and H_2O shown in Table 6.3 and Table 6.6 summarize the main reactions for H_2 combustion and the investigation of CO and CO_2 in Table 6.4 and Table 6.5 helps generate the reactions for CO combustion. In the next section, the reduced chemical mechanism of the flame will be built using the sensitivity analysis, and will be applied to the CFD model and compared with the previous PDF simulations from Section 4.5 to test its performance. The summarized main reactions for the flame are listed in Table 6.11 as a new reduced reaction mechanism. However, the main NO_x reactions are not included because Correa and Gulati flame does not have experimental data for

NO_x. Therefore, it is difficult to determine the predictive accuracy of NO_x for the current study. Extensive work will be performed in the future from sensitivity analysis to mechanism reduction for the Dally et al. flame to test the performance of main NO_x reactions and compare with the corresponding experimental results.

Table 6.8 Sensitivity of NO₂ with respect to the rate coefficients

Flame Zone	Reactions	Sensitivity coefficient
RECIR.	$\text{N}_2\text{O} + \text{O} \rightarrow 2\text{NO}$	0.700
	$\text{HO}_2 + \text{NO} \rightarrow \text{NO}_2 + \text{OH}$	0.602
	$\text{NO}_2 + \text{O} \leftarrow \text{NO} + \text{O}_2$	0.567
	$\text{H} + \text{O}_2 + \text{M} \rightarrow \text{HO}_2 + \text{M}$	-0.424
	$\text{H} + \text{O}_2 \rightarrow \text{O} + \text{OH}$	0.419
	$\text{N}_2\text{O} + \text{H} \rightarrow \text{N}_2 + \text{OH}$	-0.213
FLAME.1	$\text{HO}_2 + \text{NO} \rightarrow \text{NO}_2 + \text{OH}$	0.988
	$\text{H} + \text{O}_2 \rightarrow \text{O} + \text{OH}$	0.666
FLAME.2	$\text{H} + \text{O}_2 + \text{M} \rightarrow \text{HO}_2 + \text{M}$	0.478
	$\text{N}_2\text{O} + \text{O} \rightarrow 2\text{NO}$	0.702
	$\text{NO}_2 + \text{O} \leftarrow \text{NO} + \text{O}_2$	0.433
	$\text{HO}_2 + \text{NO} \rightarrow \text{NO}_2 + \text{OH}$	0.300
	$\text{N}_2\text{O} + \text{H} \rightarrow \text{N}_2 + \text{OH}$	0.214
	$\text{O} + \text{HO}_2 \rightarrow \text{OH} + \text{O}_2$	0.154
	$\text{H} + \text{O}_2 + \text{M} \rightarrow \text{HO}_2 + \text{M}$	-0.112
FLAME.3	$\text{H} + \text{O}_2 + \text{M} \rightarrow \text{HO}_2 + \text{M}$	-0.301
	$\text{N}_2 + \text{O} \rightarrow \text{N} + \text{NO}$	0.418
	$\text{N}_2\text{O} + \text{O} \rightarrow 2\text{NO}$	0.450
FLAME.4	$\text{H} + \text{O}_2 + \text{M} \rightarrow \text{HO}_2 + \text{M}$	-0.333
	$\text{H} + \text{O}_2 \rightarrow \text{O} + \text{OH}$	0.282
	$\text{N}_2 + \text{O} \rightarrow \text{N} + \text{NO}$	0.414
	$\text{N}_2\text{O} + \text{O} \rightarrow 2\text{NO}$	0.443
	$\text{HO}_2 + \text{NO} \leftarrow \text{NO}_2 + \text{OH}$	0.571
	$\text{NO}_2 + \text{O} \leftarrow \text{NO} + \text{O}_2$	0.411

6.7. CFD performance of reduced reaction mechanisms

In this section, several reduced reaction mechanisms are employed using CFD and compared with the previous simulations using the PDF method in order to test their performances in terms of accuracy and computational time. Two reduced mechanisms were extracted from published literature and are tested here. The third mechanism is developed based on the sensitivity analysis from Section 6.6.

6.7.1. 3-step mechanism

The 3-step reduced mechanism developed by Rogg and Williams [71] is employed for a H₂/CO/N₂ syngas flame. The set of reactions is shown in Table 6.9. The parameters A, b and E_A are used to calculate the reaction-rate coefficient (κ) based on Eq. (3.26) in Section 3.3.2.

Table 6.9 Overview of the 3-step reduced mechanism

No.	Reactions	A m ³ /kmol·s	b	E _A J/kmol
1	CO + H ₂ O ↔ CO ₂ + H ₂	2.8×10 ¹²	0	1.84×10 ⁶
2	2H + M ↔ H ₂ + M	6.4×10 ¹⁴	-1	0
3	O ₂ + 3H ₂ ↔ 2H + 2H ₂ O	1×10 ¹¹	0	1.02×10 ⁶

6.7.2. 8-step mechanism

A computer assisted reduction mechanism code (CARM) [79] was used by Collins et al. [83] to produce a more reasonable reduced set of mechanisms. Based on the zero-dimensional simulation of perfectly stirred reactors (PSR), a 6-step reduced reaction mechanism was formed from 119 reactions [83]. Based on this 6-step mechanism and 3-step reduced reactions, the 8-step mechanism was developed and shown in Table 6.10.

Table 6.10 Overview of the 8-step reduced mechanism

No.	Reactions	A m ³ /kmol-s	b	E _A J/kmol
1	CO + H ₂ O ↔ CO ₂ + H ₂	2.8×10 ¹²	0	1.8×10 ⁶
2	O + CO ↔ CO ₂	6.0×10 ⁸	0	1.3×10 ⁷
3	O + H ₂ → H + OH	38.7	2.7	2.62 × 10 ¹⁰
4	O ₂ + 3H ₂ ↔ 2H + 2H ₂ O	1.0×10 ¹¹	0	1.0×10 ⁶
5	H + O ₂ → O + OH	2.65 × 10 ¹³	-0.67	9.13 × 10 ¹⁰
6	2H + M ↔ H ₂ + M	6.4×10 ¹⁴	-1	0
7	OH + H ₂ → H + H ₂ O	2.16 × 10 ⁵	1.51	1.44 × 10 ¹⁰
8	H + 2NO ↔ N ₂ + O + OH	4.4×10 ¹¹	0	7.9×10 ⁷

6.7.3. 9-step mechanism

A new 9-step mechanism is generated based on the mechanism reduction work of the sensitivity analysis in Section 6.6. All reactions with high absolute sensitivity coefficients shown in Table 6.3 to Table 6.6 have been selected and included in the reduced mechanism. Since many reactions appeared multiple times in each species sensitivity analysis, the sum of all the reactions from the sensitivity analysis becomes a 9-step reaction mechanism. Table 6.11 shows the reactions of the 9-step reduced mechanism.

Table 6.11 Reduced reactions based on sensitivity analysis

No.	Reactions	A m ³ /kmol-s	b	E _A J/kmol
1	H + O ₂ → O + OH	2.65 × 10 ¹³	-0.67	9.13 × 10 ¹⁰
2	H + HO ₂ → O ₂ + H ₂	4.48 × 10 ¹⁴	0	4.47 × 10 ⁹
3	OH + H ₂ → H + H ₂ O	2.16 × 10 ⁵	1.51	1.44 × 10 ¹⁰
4	O + H ₂ → H + OH	38.7	2.7	2.62 × 10 ¹⁰
5	H + O ₂ + M → HO ₂ + M	2.60 × 10 ¹⁶	-1.24	0
6	OH + CO → H + CO ₂	4.76 × 10 ⁴	1.23	2.93 × 10 ⁸
7	HO ₂ + CO → OH + CO ₂	1.50 × 10 ¹¹	0	9.87 × 10 ¹⁰
8	HCO + M → H + CO + M	1.87 × 10 ¹⁴	-1	7.11 × 10 ¹⁰
9	H + HO ₂ → 2OH	0.84 × 10 ¹¹	0	2.66 × 10 ⁹

6.7.4. Comparison between reduced mechanisms and PDF method

Figure 6.16 shows the comparisons of temperature contours with the 3-step, 8-step, 9-step mechanisms and the PDF model. The contours are spliced with the PDF results to compare the differences. Clearly, the results from the reduced mechanisms show similar temperatures as the PDF method. However, for the comparison between the reduced mechanisms and the PDF results, temperature contour from 3-step model does not align with the PDF result in the flame neck region, which is an important area with available experimental data at $X/D_j=10$ and 20. For the 8-step and 9-step models, the alignment near the flame neck region gets better, but the temperature near the jet-flame region is higher than the PDF results, especially for the 8-step.

Figure 6.17 shows the results of temperature among the different models at $X/D_j=10, 20$, and are compared to the experiments [16]. Experimental data are shown as points and the PDF results are shown as solid lines. The reduced reaction mechanisms are shown as dash, dash-dot and dash-dot-dot lines for 3-step, 8-step and 9-step mechanism, respectively. In Figure 6.17 (a), the 3-step and 8-step mechanisms over-predict peak temperature with much larger values around 2000 K, whereas the experimental peak temperature is 1600 K. The newly developed 9-step mechanism also presents a higher maximum temperature than the experimental peak temperature but has some improvement over the 3-step and 8-step.

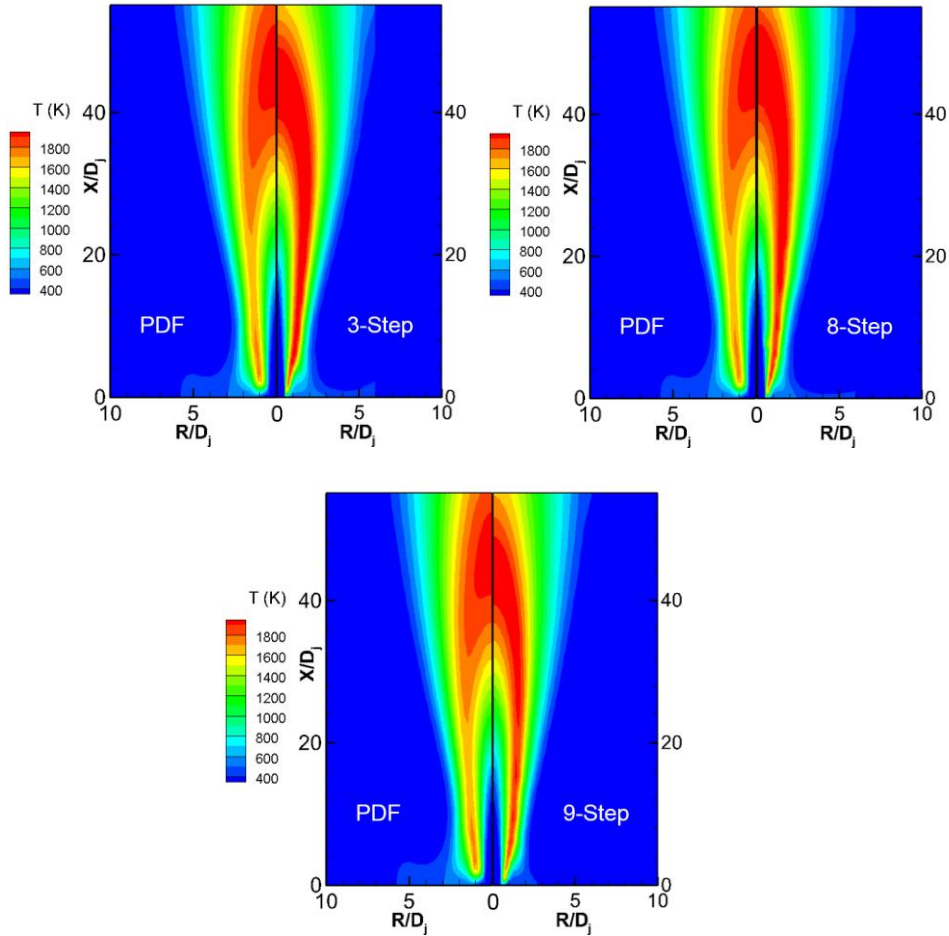


Figure 6.16 Temperature contour comparison with PDF method

Figure 6.18 shows the radial profiles of hydrogen and water at $X/D_j=20$, which includes the results from the three reduced reaction mechanism, the PDF method and the experimental results. Similar as the temperature profile in Figure 6.17, 3-step and 8-step mechanisms show very close profiles for hydrogen. Reduced mechanisms like the 3-step and 8-step under-predict the decay of H_2 along the radial distance. In the radial profile of hydrogen shown in Figure 6.18 (a), both PDF results and the 9-step results are close to the experimental results except for the value near the centerline (when $R/D_j \sim 0$). The decay of H_2 occurs as the fuel is consumed when it enters in the burner and the co-flow of air mixes with the fuel, decreasing the H_2 .

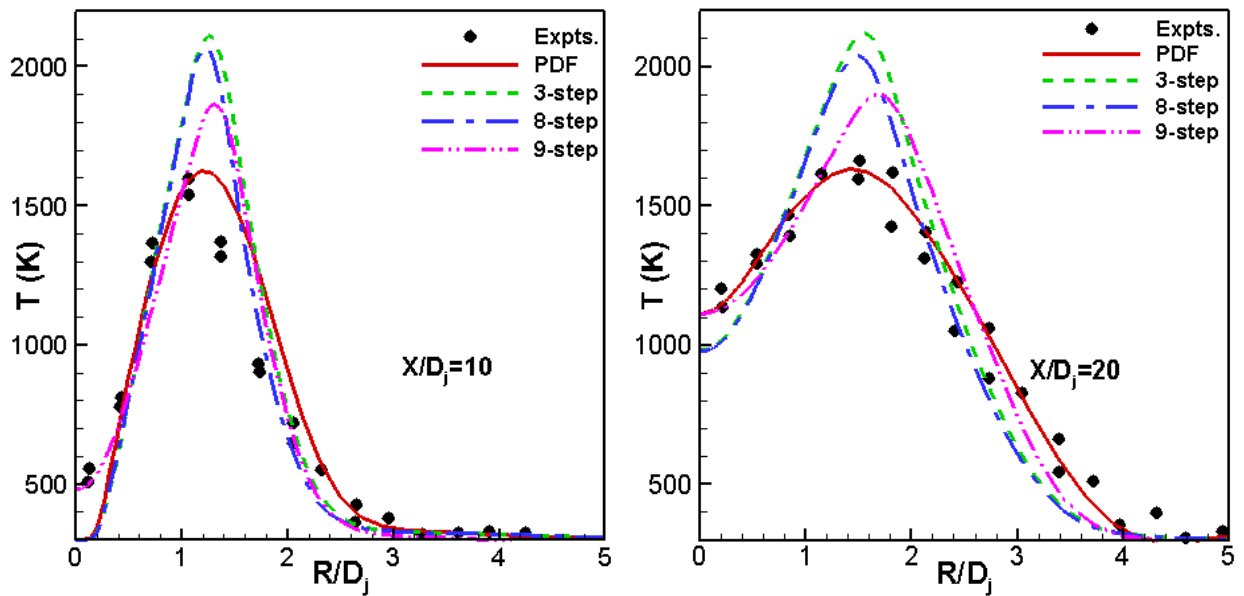


Figure 6.17 Radial temperature profiles at $X/D_j=10$ and $X/D_j=20$

Figure 6.18 (b) presents the radial profiles of H_2O and compares the numerical results with experimental data at $X/D_j=20$. In Figure 6.18 (b), the 9-step model represents the best predictive performance among all the models. Although the 9-step model has some deviation near the centerline, it gets the correct shape of the H_2O distribution and the predictions improve when radial distance increases. Previous simulation work reported in the literature [16, 38, 162] has identified that H_2O is always not satisfactorily predicted as other species. The predictions shown in Figure 6.18 (b) for H_2O improve greatly by using the 12-step model. A plausible reason for the improvement is that the reduced reaction mechanism (see Table 6.11) generated based on the sensitivity analysis of H_2 and H_2O helps provide a more complete set of reactions than the other reduced models.

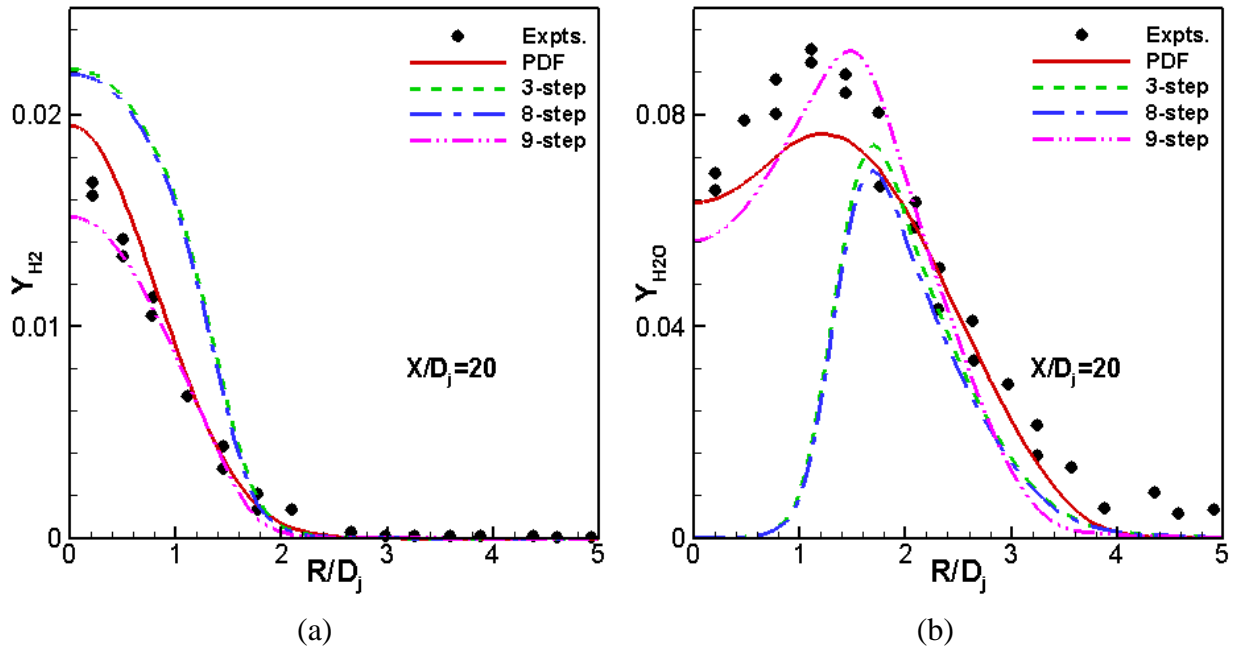


Figure 6.18 Radial profiles at $X/D_j=20$: (a) H_2 mass fraction; (b) H_2O mass fraction

Noticeably, the 3-step and 8-step models predict almost identical profiles of CO and H_2 mass fractions at both axial positions. Based on the mediocre performance of these two models, it shows that the addition of five reactions to the 3-step model does not have much improvement of the numerical results. In fact, the 9-step mechanism has shown to be a better reduced reaction model for syngas and further analysis of the model will be discussed next.

The scatter plot of temperature along the reaction time scale has been created for each computed cell under the 9-step mechanism and shown in Figure 6.19. The time scale of the reactions has been calculated based on Eq. (3.23) in the EDC model. Temperature maintains at 300 K when time exceeds 0.0004 s, which indicates the unreactive region with massive excess air. The fuel jet velocity at the centerline decays from initial value of 80m/s to 20 m/s from Figure 4.10 (a), while air velocity at the inlet is only 6.5 m/s. The minimum diffusion time is $\tau_{diff, \min} = L / V_{fuel, \max} = 0.0022s$ when the maximum fuel jet velocity is 80 m/s. The reaction time is

$\tau_{react}=4E-5$ s for most cell results. These time scales, taken together, the characteristic Damköhler number (Da) as the ratio of flow time over reaction time is 55, which is much larger than unity, indicating the validity of chemical equilibrium assumption.

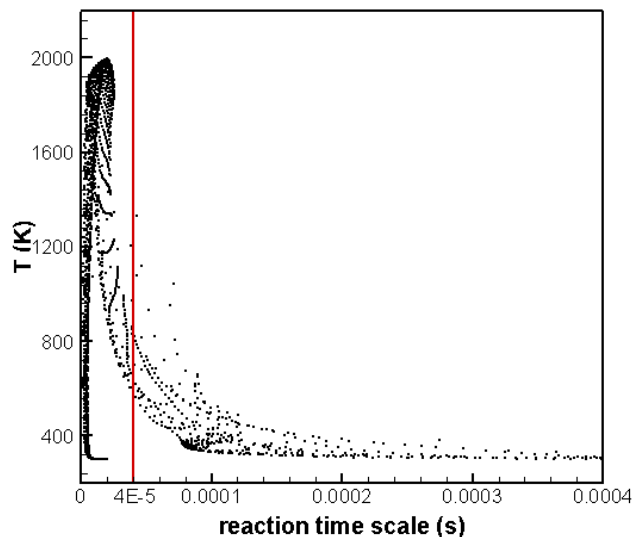


Figure 6.19 Temperature along the time scale of reactions

6.7.5. Comparison of computational time

Figure 6.20 shows a comparison of the computational time of the 4 models for 1000 iterations. In Figure 6.20, the computational time of the reduced mechanism models is longer than the PDF model and the CPU time increases with the addition of the reactive steps. The PDF model shows the smallest computational time, and compared with the reduced mechanism models, the computational time saved is 18.6%, 38.3%, 43.8% for the 3-step, 8-step, 9-step chemical mechanism models, respectively. Aligned with the prediction accuracy of the reduced models discussed in the last section and the efficiency performance in this section, the PDF model is still the most efficient method to simulate the non-premixed flame.

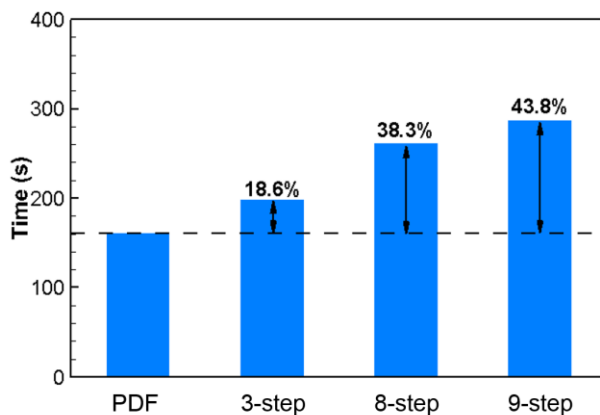


Figure 6.20 Comparison of computational time

6.8. Conclusions

This chapter mainly conducted the study of chemical reactor network, investigated chemical mechanisms of combustion process and pollutants formation through the created network and the study of rate production and sensitivity analysis. Based on the experimental operating conditions and the basic insights of the CFD results, the CRN model was developed and the allocations of volumetric values of elemental reactors were conducted. Extensive measurements of flame characteristics such as temperature, species concentration were compared and validated for two bluff-body flames, namely Correa and Gulati [16] flame and Dally et al. [134] flame. Because of the rational arrangement of the reactor network and accurate prediction of volumetric information and input flow rates from CFD, the CRN model for both bluff-body flames also provided accurate results of temperature and species at the exit of the burner. A thorough study of NO_x formation was conducted based on the calculation of rate of production and the normalized sensitivity coefficient of NO_x . First, NO_x presents higher value at regions with high temperature due to the thermal NO_x mechanism. Second, atomic oxygen and hydrogen are very influential in NO_x formation, since the chain branching of the fuels and oxidizer would not only accelerate combustion process with

temperature increased, but also provide high concentration of important radicals to increase the rate of production of NO_x . In addition, major reactions of combustion also shows high sensitivity to NO_x , since temperature and radicals from the main reactions can be influential to NO_x emission.

A normalized sensitivity analysis of fuel mixture and major products has been conducted, based on which main reactions that have significant impact and control on combustion process have been generated. Then, a comparative study of different reduced chemical mechanism models and the PDF model was conducted to assess the reduced kinetics and compare them with the experimental results from Correa and Gulati [16] flame. Three reduced reaction mechanisms are studied, namely the 3-step from Rogg and Williams [71], 8-step from Collins et al. [83] and 9-step generated from the sensitivity analysis from GRI-Mech 3.0. The comparison results have shown that the 3-step and 8-step have close results, both of which over-predict temperature and show obvious difference of species profile with the experimental data. 9-step results get improvement in the temperature prediction, however, the PDF results of temperature still show the best agreement with the experimental results. Noticeably, the 9-step mechanism shows the closest radial profile of H_2O than other results, indicating that the 9-step mechanism generated through the sensitivity analysis of H_2 and H_2O have provided a more complete set of reactions than the other reduced models.

Chapter 7. Conclusions and Future work

7.1. Summary

Turbulent combustion modeling is a complex system involving turbulent flow, fuel diffusion and oxidation and the formation and burnout of pollutants. [1, 21]. Due to the extreme demands and applications, it is important to have solid understanding of turbulent combustion processes and provide accurate predictions and physical insights of the combustion process.

The main objective of this research was to conduct a thorough analysis and comparison of both turbulence models and chemistry representation methods to test their performance in standalone CFD and CRN models, as well as in a coupled system. Terms like accuracy, memory requirements, and computational costs as well as the effects of modeling assumptions on the long-time error accumulation were assessed. A comparative study was conducted between RANS and LES approaches and it was found that the LES time-averaged results were very close to RANS results. Considering that much longer time is needed for the LES model and that the RANS approach can capture the mean flow features fairly well, the RANS approach was determined more suitable in the study. The symmetric distribution of temperature results made the CFD model even more simplified with a 2D axisymmetric computational domain. The RANS-based turbulence models were tested and it was found that the realizable k - ϵ and RSM model showed better results and agreement with experimental data. To optimize the turbulence model, the discussion of turbulence intensity levels and computational domain (with and without bluff-body for flow development) was considered. The results indicated that the turbulence intensity level had a substantial impact on the axial decay of mixture fraction and temperature, velocity, and strain rate and the value calculated based on the empirical equation from Durst et al. [130] presents the best estimation of turbulent fluctuation at the inlet. It was also found that the addition of the bluff body improved the

2D axisymmetric predictions and diminished differences caused by specifying inlet turbulence intensities, which made the numerical predictions indistinguishable, irrespective of inlet initial values. This was because the length of the bluff body allowed the fuel and air streams fully developed before they mixed and combust.

The established CFD modeling techniques were then applied to the bluff-body flame reported by Dally et al. [134], and the experimental uncertainty, NO_x formation and the effects of fuel mixtures were studied. The method from ASME was found most suitable to estimate the experimental uncertainty. The radial profiles and comparison of mixture fraction and temperature with the experimental data have shown and demonstrated good performance of the established CFD model to predict different bluff-body flames. The NO formation and the effects of fuel mixtures on NO emission were studied using the Zeldovich mechanism. The profiles of NO emission along with the mixture fraction have shown that the CFD model captured close trends of NO from the experimental work. The NO profiles showed similar trends as temperature profiles indicating strong correlation with temperature. For the study of fuel and diluent mixtures, it was found that hydrogen as fuel, CO₂ and H₂O as non-flammable diluents can be applied as one useful fuel or diluent addition to reduce the pollutant emission of NO in the syngas flames.

To obtain a better understanding of the chemical kinetics and emission formation, a CRN model was constructed based on the flow fields and flame patterns from CFD results to capture the chemical processes. Species and pollutants such as NO_x were predicted using the detailed chemical kinetic reaction database of GRI-Mech 3.0 [91]. The CRN results showed predictive and applicable capacities in the bluff-body flames. Based on the study of rate of production and the sensitivity analysis, a better understanding of NO_x formation and distribution was pursued. NO_x has been found very sensitive to temperature, atomic hydrogen and oxygen, and main reactions of combustion

process that contributes to temperature increase and radicals concentrations. In addition, a thorough sensitivity analysis of fuel mixture and major products provided valuable information to create a reduced 9-step reaction mechanism. A comparative study of different reduced chemical mechanism models and the PDF model was conducted to assess the reduced kinetics and compare them with the experimental results from Correa and Gulati [16] flame. The comparisons showed that the 3-step from Rogg and Williams [71] and 8-step Collins et al. [83] had close results, both of which over-predicted temperature and showed obvious difference of species profile with the experimental data. The 9-step results showed improvement in the temperature prediction, while the PDF results of temperature still showed the best agreement with the experimental results. Noticeably, the 9-step mechanism showed the closest radial profile of H₂O than other results, indicating that the 9-step mechanism generated through the sensitivity analysis of H₂ and H₂O provided a more complete set of reactions than the other reduced models.

7.2. Significance and contribution

The main objective of this study was to numerically simulate turbulent combustion problems and identify the most reliable turbulence models and chemistry representation models. CFD has been widely used with significant progress to understand combustion processes and assist with the design of combustors over the last few decades. However, typical CFD modeling issues such as the turbulence-chemistry interactions have not been resolved and still need efforts to not only improve the modeling methods and techniques but also provide both physical and chemical insights of the combustion process.

The first part of work with CFD modeling identified the importance of the turbulence model, boundary conditions, turbulence intensity level and computational domain. The CFD model was simplified and created based on a through comparison and validation work. It was found that using

a 2D axisymmetric domain with uniform inlet velocity profile was reasonable if the turbulence intensity was correctly specified using the empirical correlation from Durst et al. [130]. It was also found that the addition of the bluff-body in the computational domain diminished differences caused by different numerical predictions and initial values at inlet boundary since the length of the bluff-body allowed the streams to fully develop. The discussion of the NO_x formation and the effects of fuel mixtures provided valuable suggestions of pollutant reduction that H_2 , CO_2 and steam are favorable components to reduce NO_x in the syngas combustion system.

In the second part of work, a new CRN model was constructed with the initialization results from CFD. The successful created CRN model for different bluff-body flames demonstrated that a carefully constructed CRN structure can be applied to other similar bluff-body flames and accurately predict temperature, species and NO_x distribution and transportation across the combustor and at the exit of the combustor, which is valuable for both numerical and experimental work in the future. Instead of CFD modeling or other simulations of hundreds gaseous reactions, the temperature and species distribution across the bluff-body flame can be easily obtained through the CRN model with primary volumetric information and initial temperature, which is quite easy to achieve in the experimental work through laser-induced or infrared techniques. In addition, the sensitivity analysis of the CRN results is also promising, which can identify representative reactions efficiently in other syngas flames. The employment of the reduced mechanism in the CFD model also demonstrated that the generated reduced mechanism provides valuable information and good predictions. The use of CRN and the coupled work with CFD has bright new insights for the numerical investigation in turbulent combustion systems.

7.3. Future work

The successful generation of CRN models based on CFD and the study of the rate of production and sensitivity have provided new insights and remarkable progress on modeling turbulent combustion systems. In this study, the CRN was generated based on CFD results and the reduced reactions summarized from the sensitivity analysis of CRN were applied back to CFD model, which makes the modeling system as a fully coupled loop.

However, the work is only one-time coupled and the main future work should be to enable the connection and exchange between CFD and CRN simultaneously. The work of RANS and LES simulations has revealed that the bluff-body flame problems in this study can reach steady-state, which makes the one-time couple between CFD and CRN applicable. However, for a combustion problem that does not achieve a quasi-equilibrium state, the instantaneous couple between CFD and CRN becomes significantly important. With this achieved, CFD will be able to exchange volumetric information and update the thermo-characteristics of reactors to CRN, based on which the reduced reaction mechanisms generated from the calculated sensitivity coefficients will be more accurate.

The current work and a majority of work from other researchers have used and constructed the reactor zones through temperature and flow patterns. However, constructing such a reactor network is rather empirical and slight changes might lead to a new reactor network configuration. Therefore, algorithms need to be developed to create the elemental reactor zones and network in the future work of CRN and the generated algorithms should be able to split flow areas regarding to different interested features.

In addition, as mentioned in Section 6.6, the study of chemical mechanism reduction through sensitivity analysis and the predictive performance of temperature, species and NO_x under the

reduced mechanism will also be conducted. Different NO_x models will be comparatively studied, including the Zeldovich mechanism (FLUENT post-process model) under PDF-equilibrium, the Zeldovich mechanism under reduced chemical mechanism and the main NO_x reaction mechanism from the sensitivity analysis work of NO_x . The prediction under different models will be compared with the experimental data from Dally et al [134] to study the performance of the NO_x models and the reason for changes.

References

- [1] Echehki, T., and Mastorakos, E., 2010, Turbulent combustion modeling: Advances, new trends and perspectives, Springer Science & Business Media.
- [2] Lu, X., Han, D., and Huang, Z., 2011, "Fuel design and management for the control of advanced compression-ignition combustion modes," *Progress in Energy and Combustion Science*, 37(6), pp. 741-783.
- [3] Breidenthal, R., 1981, "Structure in turbulent mixing layers and wakes using a chemical reaction," *Journal of Fluid Mechanics*, 109, pp. 1-24.
- [4] Peters, N., 2000, Turbulent combustion, Cambridge university press.
- [5] Magnussen, B. F., and Hjertager, B. H., "On mathematical modeling of turbulent combustion with special emphasis on soot formation and combustion," *Proc. Symposium (International) on Combustion*, Elsevier, pp. 719-729.
- [6] Pope, S., "Computations of turbulent combustion: progress and challenges," *Proc. Symposium (International) on Combustion*, Elsevier, pp. 591-612.
- [7] Borghi, R., 1988, "Turbulent combustion modelling," *Progress in energy and combustion science*, 14(4), pp. 245-292.
- [8] Correa, S. M., 1993, "A review of NO_x formation under gas-turbine combustion conditions," *Combustion science and technology*, 87(1-6), pp. 329-362.
- [9] Chow, J. C., and Watson, J. G., 2002, "Review of PM_{2.5} and PM₁₀ apportionment for fossil fuel combustion and other sources by the chemical mass balance receptor model," *Energy & Fuels*, 16(2), pp. 222-260.
- [10] Moore, M. J., 1997, "NO_x emission control in gas turbines for combined cycle gas turbine plant," *Proceedings of the Institution of Mechanical Engineers*, 211(1), pp. 43-52.
- [11] Park, J., Kim, S. C., Keel, S. I., Noh, D. S., Oh, C. B., and Chung, D., 2004, "Effect of Steam Addition on Flame Structure and NO Formation in H₂-O₂-N₂ Diffusion Flame," *International Journal of Energy Research*, 28(12), pp. 1075-1088.
- [12] Giles, D. E., Som, S., and Aggarwal, S. K., 2006, "NO_x emission characteristics of counterflow syngas diffusion flames with airstream dilution," *Fuel*, 85(12-13), pp. 1729-1742.
- [13] Mathur, T., Gruber, M., Jackson, K., Donbar, J., Donaldson, W., Jackson, T., and Billig, F., 2001, "Supersonic combustion experiments with a cavity-based fuel injector," *Journal of Propulsion and Power*, 17(6), pp. 1305-1312.
- [14] Kamotani, Y., and Greber, I., 1972, "Experiments on a turbulent jet in a cross flow," *AIAA journal*, 10(11), pp. 1425-1429.

- [15] Huan, X., and Marzouk, Y. M., 2013, "Simulation-based optimal Bayesian experimental design for nonlinear systems," *Journal of Computational Physics*, 232(1), pp. 288-317.
- [16] Correa, S. M., and Gulati, A., 1992, "Measurements and Modeling of a Bluff Body Stabilized Flame," *Combustion and Flame*, 89(2), pp. 195-213.
- [17] Dally, B. B., Feltcher, D. F., and Masri, A. R., 1998, "Flow and mixing fields of turbulent bluff-body jets and flames," *Combustion Theory and Modelling*, 2(2), pp. 193-219.
- [18] Masri, A., Dibble, R., and Barlow, R., 1996, "The structure of turbulent nonpremixed flames revealed by Raman-Rayleigh-LIF measurements," *Progress in Energy and Combustion Science*, 22(4), pp. 307-362.
- [19] Lu, T., and Law, C. K., 2009, "Toward accommodating realistic fuel chemistry in large-scale computations," *Progress in Energy and Combustion Science*, 35(2), pp. 192-215.
- [20] Delarue, B., and Pope, S., 1997, "Application of PDF methods to compressible turbulent flows," *Physics of Fluids (1994-present)*, 9(9), pp. 2704-2715.
- [21] Stöllinger, M., and Heinz, S., 2008, "PDF modeling and simulation of premixed turbulent combustion," *Monte Carlo Methods and Applications*, 14(4), pp. 343-377.
- [22] Zhiyin, Y., 2015, "Large-eddy simulation: Past, present and the future," *Chinese Journal of Aeronautics*, 28(1), pp. 11-24.
- [23] Maele, K. V., Merci, B., and Dick, E., 2003, "Comparative study of k- ϵ turbulence models in inert and reacting swirling flows," 33rd AIAA Fluid Dynamics Conference and Exhibit, 2003-3744.
- [24] Yilmaz, D., Onbasioglu, S. U., and Gökalp, I., 2005, "Computational modeling of hydrogen enriched non premixed turbulent methane air flames," In *Proceedings of European Combustion Meeting Louvain-la-Neuve, Belgium*.
- [25] Frassoldati, A., Sharma, P., Cuoci, A., Faravelli, T., and E., R., 2010, "Kinetic and fluid dynamics modeling of methane/hydrogen jet flames in diluted coflow," *Applied Thermal Engineering*, 30(4), pp. 376-383.
- [26] Angelberger, C., Veynante, D., Egolfopoulos, F., and Poinso, T., 1998, "Large eddy simulations of combustion instabilities in premixed flames," *Proc. of the Summer Program*, pp. 61-82.
- [27] Charlette, F., Trouvé, A., Boger, M., and Veynante, D., 1999, "A flame surface density model for large eddy simulations of turbulent premixed flames," *Proceedings of the Joint Meeting of the British, German and French Sections of the Combustion Institute*.
- [28] McIlroy, A., McRae, G., Sick, V., Siebers, D., Westbrook, C., Smith, P., Taatjes, C., Trouve, A., Wagner, A., and Rohlfing, E., 2006, "Basic research needs for clean and efficient combustion of 21st century transportation fuels," *DOESC (USDOE Office of Science (SC))*.

- [29] Ziani, L., Chaker, A., Chetehouna, K., Malek, A., and Mahmah, B., 2013, "Numerical simulations of non-premixed turbulent combustion of CH₄-H₂ mixtures using the PDF approach," *International Journal of Hydrogen Energy*, 88(20), pp. 8597-8603.
- [30] Choudhuri, A. R., and Gollahali, S. R., 2003, "Characteristics of hydrogen-hydrocarbon composite fuel turbulent jet flames," *International Journal of Hydrogen Energy*, 28(4), pp. 445-454.
- [31] Hwang, C. H., Lee, S., and Lee, C. E., 2008, "The effect of turbulence intensity of ambient air flow on NO_x emissions in H₂/air nonpremixed jet flames," *International Journal of Hydrogen Energy*, 33(2), pp. 832-841.
- [32] Novosselov, I., Malte, P., Yuan, S., Srinivasan, R., and Lee, J., "Chemical reactor network application to emissions prediction for industrial die gas turbine," *Proc. ASME turbo expo 2006: Power for land, sea, and air*, American Society of Mechanical Engineers, pp. 221-235.
- [33] Jones, W., and Whitelaw, J., 1982, "Calculation methods for reacting turbulent flows: a review," *Combustion and flame*, 48, pp. 1-26.
- [34] Liu, K., Pope, S. B., and Caughey, D. A., 2005, "Calculations of bluff-body stabilized flames using a joint probability density function model with detailed chemistry," *Combustion and Flame*, 141(1-2), pp. 89-117.
- [35] Huang, R. F., and Lin, C. L., 2000, "Velocity Fields of Nonpremixed Bluff-Body Stabilized Flames," *J. Energy Resour. Technol.*, 122(2), pp. 88-93.
- [36] "TNF Workshop: <http://www.sandia.gov/TNF/abstract.html>."
- [37] Hassan, G., Pourkashanian, M., Ingham, D., Ma, L., Newman, P., and Odedra, A., 2013, "Predictions of CO and NO_x emissions from steam cracking furnaces using GRI2.11 detailed reaction mechanism—A CFD investigation," *Computers & Chemical Engineering*, 58, pp. 68-83.
- [38] Gran, I. R., and Magnussen, B. F., 1996, "A numerical study of a bluff-body stabilized diffusion flame. Part 1. Influence of turbulence modeling and boundary conditions," *Combustion science and technology*, 119(1-6), pp. 171-190.
- [39] Merci, B., Langhe, C. D., Lodefier, K., and Dick, E., 2004, "Axisymmetric Impingement Heat Transfer with a Nonlinear ke Model," *Journal of Thermophysics and Heat Transfer*, 18(1), pp. 100-107.
- [40] Hossain, M., 1999, "CFD modelling of turbulent non-premixed combustion," Doctor of Philosophy Doctoral Thesis, Loughborough University.
- [41] Mardani, A., and Tabejamaat, S., 2010, "Effect of hydrogen on hydrogen-methane turbulent non-premixed flame under MILD condition," *International Journal of Energy Research*, 35(20), pp. 11324-11331.

- [42] Ligrani, P. M., Burges, N. K., and Won, S. Y., 2004, "Nusselt Numbers and Flow Structure on and Above a Shallow Dimpled Surface Within a Channel Including Effects of Inlet Turbulence Intensity Level," *Journal of Turbomachinery*, 127(2), pp. 321-330.
- [43] Sundaram, S. S., Babu, V., Obulesu, C., and Sivakumar, R., 2012, "Three-dimensional numerical simulations of turbulent, bluff-body stabilized, lean, premixed combustion," *Combustion Science and Technology*, 184(3), pp. 351-373.
- [44] Li, T., Pannala, S., and Shahnam, M., 2014, "CFD simulations of circulating fluidized bed risers, part II, evaluation of differences between 2D and 3D simulations," *Powder Technology*, 254, pp. 115-124.
- [45] Liu, J., Shang, H. M., and Chen, Y. S., 2000, "Development of an unstructured radiation model applicable for two-dimensional planar, axisymmetric and three-dimensional geometries," *Journal of Quantitative Spectroscopy & Radiative Transfer*, 66(1), pp. 17-33.
- [46] Fukumoto, K., and Ogami, Y., 2012, "Combustion simulation technique for reducing chemical mechanisms using look-up table of chemical equilibrium calculations: Application to CO-H₂-air turbulent non-premixed flame," *Computer & Fluids*, 66, pp. 98-106.
- [47] Meester, R. D., Naud, B., Maas, U., and Merci, B., 2012, "Transported scalar PDF calculations of a swirling bluff body flame ('SM1') with a reaction diffusion manifold," *Combustion and Flame*, 159(7), pp. 2415-2429.
- [48] Ren, Z., Goldin, G. M., Hiremath, V., and Pope, S. B., 2013, "Simulations of a turbulent non-premixed flame using combined dimension reduction and tabulation for combustion chemistry," *Fuel*, 105, pp. 636-644.
- [49] Kim, M. Y., and Baek, S. W., 2005, "Modeling of radiative heat transfer in an axisymmetric cylindrical enclosure with participating medium," *Journal of Quantitative Spectroscopy and Radiative Transfer*, 90(3), pp. 377-388.
- [50] Reuge, N., Cadoret, L., Coufort-Saudejaud, C., Pannala, S., Syamlal, M., and Causat, B., 2008, "Multifluid Eulerian modeling of dense gas-solids fluidized bed hydrodynamics: influence of the dissipation parameters," *Chemical Engineering Science*, 63(22), pp. 5540-5551.
- [51] Xie, N., Battaglia, F., and Pannala, S., 2008, "Effects of using two-versus three-dimensional computational modeling of fluidized beds: Part I, hydrodynamics," *Powder Technology*, 182(1), pp. 1-13.
- [52] Xie, N., Battaglia, F., and Pannala, S., 2008, "Effects of using two-versus three-dimensional computational modeling of fluidized beds: Part II, budget analysis," *Powder Technology*, 182(1), pp. 14-24.
- [53] Cammarata, L., Lettieri, P., Micale, G. D. M., and Colman, D., 2003, "2D and 3D CFD simulations of bubbling fluidized beds using Eulerian-Eulerian models," *International Journal of Chemical Reactor Engineering*, 1(1), pp. 1542-6580.

- [54] Jenny, P., Muradoglu, M., Liu, K., Pope, S., and Caughey, D., 2001, "PDF simulations of a bluff-body stabilized flow," *Journal of Computational Physics*, 169(1), pp. 1-23.
- [55] Hossain, M., Jones, J., and Malalasekera, W., 2001, "Modelling of a bluff-body nonpremixed flame using a coupled radiation/flamelet combustion model," *Flow, Turbulence and Combustion*, 67(3), pp. 217-234.
- [56] Medici, D., and Alfredsson, P., 2006, "Measurements on a wind turbine wake: 3D effects and bluff body vortex shedding," *Wind Energy*, 9(3), pp. 219-236.
- [57] Roshko, A., 1954, "On the drag and shedding frequency of two-dimensional bluff bodies," National Advisory Committee for Aeronautics, NACA TN 3169, Washington, D.C.
- [58] Hackett, J., and Cooper, K., 2001, "Extensions to Maskell's theory for blockage effects on bluff bodies in a closed wind tunnel," *Aeronautical Journal*, 105(1050), pp. 409-418.
- [59] Fan, A., Wan, J., Liu, Y., Pi, B., Yao, H., and Liu, W., 2014, "Effect of bluff body shape on the blow-off limit of hydrogen/air flame in a planar micro-combustor," *Applied Thermal Engineering*, 62(1), pp. 13-19.
- [60] Park, J., Lee, D. H., Yoon, S. H., Vu, T. M., Yun, J. H., and Keel, S. I., 2009, "Effects of Lewis number and preferential diffusion on flame characteristics in 80% H₂/20% CO syngas counterflow diffusion flames diluted with He and Ar," *International Journal of Hydrogen Energy*, 34(3), pp. 1578-1584.
- [61] Naha, S., and Aggarwal, S. K., 2004, "Fuel effects on NO_x emissions in partially premixed flames," *Combustion and Flame*, 139(1-2), pp. 90-105.
- [62] Sanusi, Y. S., Habib, M. A., and Mokheimer, E. M. A., 2014, "Experimental Study on the Effect of Hydrogen Enrichment of Methane on the Stability and Emission of Nonpremixed Swirl Stabilized Combustor," *J. Energy Resour. Technol.*, 137(3).
- [63] Rørtveit, G. J., Hustad, J. E., Li, S. C., and Williams, F. A., 2002, "Effects of diluents on NO_x formation in hydrogen counterflow flames," *Combustion and flame*, 130(1), pp. 48-61.
- [64] Zhang, Y., Yang, T., Liu, X., Tian, L., Fu, Z., and Zhang, K., 2012, "Reduction of Emissions From a Syngas Flame Using Micromixing and Dilution With CO₂," *Energy Fuels*, 26(11), pp. 6595-6601.
- [65] Kim, S. G., Park, J., and Keel, S. I., 2002, "Thermal and Chemical Contributions of Added H₂O and CO₂ to Major Flame Structures and NO Emission Characteristics in H₂/N₂ Laminar Diffusion Flame," *International Journal of Energy Research*, 26(12), pp. 1073-1086.
- [66] Imteyaz, B., and Habib, M. A., 2015, "Study of Combustion Characteristics of Ethanol at Different Dilution with the Carrier Gas," *J. Energy Resour. Technol.*, 137(3).

- [67] Azatyan, V. V., Shebeko, Y. N., and Shebeko, A. Y., 2010, "A numerical modelling of an influence of CH₄, N₂, CO₂ and steam on a laminar burning velocity of hydrogen in air," *Journal of Loss Prevention in the Process Industries*, 23(2), pp. 331-336.
- [68] Hasegawa, T., Sudoh, J., and Mochida, S., 1997, "High temperature air combustion with regenerative burner system," *Combustion Sci. Technol.*, 4, pp. 225-238.
- [69] Hasegawa, T., and Tanaka, R., 1998, "High Temperature Air Combustion. Revolution in Combustion Technology.(Part I New Findings on High Temperature Air Combustions.)," *JSME International Journal Series B*, 41(4), pp. 1079-1084.
- [70] Chen, L., and Battaglia, F., 2016, "The effects of fuel mixtures in non-premixed combustion for a bluff-body flame," *J. Energy Resour. Technol.*, 138(2):022204.
- [71] Rogg, B., and Williams, F., "Structures of wet CO flames with full and reduced kinetic mechanisms," *Proc. Symposium (International) on Combustion*, Elsevier, pp. 1441-1451.
- [72] Fukumoto, K., and Ogami, Y., 2010, "Turbulent diffusion combustion model using chemical equilibrium combined with the eddy dissipation concept for reducing detailed chemical mechanisms: An application of H₂ - air turbulent diffusion flame," *Heat Transfer — Asian Research*, 39(5), pp. 292-313.
- [73] Ansys, 2011, "ANSYS FLUENT theory guide," Canonsburg, PA, p. 794.
- [74] Turns, S. R., 1996, *An introduction to combustion*, McGraw-hill New York.
- [75] Burke, S., and Schumann, T., 1928, "Diffusion flames," *Industrial & Engineering Chemistry*, 20(10), pp. 998-1004.
- [76] Kuo, K. K., 1986, "Principles of combustion."
- [77] Warnatz, J., Maas, U., Dibble, R. W., and Warnatz, J., 1996, *Combustion*, Springer.
- [78] Pope, S. B., 2003, "The computation of constrained and unconstrained equilibrium compositions of ideal gas mixtures using Gibbs function continuation," *Cornell University Report FDA*, pp. 03-02.
- [79] Chen, J., "Development of reduced mechanisms for numerical modelling of turbulent combustion," *Proc. Workshop on Numerical Aspects of Reduction in Chemical Kinetics*.
- [80] Ren, Z., Goldin, G. M., Hiremath, V., and Pope, S. B., 2011, "Reduced description of reactive flows with tabulation of chemistry," *Combustion Theory and Modelling*, 15(6), pp. 827-848.
- [81] Collins, W. T., 2008, "Development and validation of a combustion model for a fuel cell off-gas burner," *University of Cambridge*.
- [82] Peters, N., and Kee, R., 1987, "The computation of stretched laminar methane-air diffusion flames using a reduced four-step mechanism," *Combustion and Flame*, 68(1), pp. 17-29.

- [83] Collins, W., Hochgreb, S., Swaminathan, N., and Chen, J., "Simulation of NO_x formation in dilute H₂/CO/N₂-air diffusion flames using full and reduced kinetics," Proc. Proceedings of the European Combustion Meeting.
- [84] Davis, S. G., Joshi, A. V., Wang, H., and Egolfopoulos, F., 2005, "An optimized kinetic model of H₂/CO combustion," Proceedings of the Combustion Institute, 30(1), pp. 1283-1292.
- [85] Frassoldati, A., Faravelli, T., and Ranzi, E., 2007, "The ignition, combustion and flame structure of carbon monoxide/hydrogen mixtures. Note 1: Detailed kinetic modeling of syngas combustion also in presence of nitrogen compounds," International Journal of Hydrogen Energy, 32(15), pp. 3471-3485.
- [86] Wang, L., Haworth, D., Turns, S., and Modest, M., 2005, "Interactions among soot, thermal radiation, and NO_x emissions in oxygen-enriched turbulent nonpremixed flames: a computational fluid dynamics modeling study," Combustion and Flame, 141(1), pp. 170-179.
- [87] Chen, L., and Battaglia, F., 2016, "Computational study comparing reduced chemical mechanisms with the PDF method in non-premixed flames," ASME 2016 Fluids Engineering Division Summer Meeting, FEDSM2016-7543.
- [88] Harris, C., Roekaerts, D., Rosendal, F., Buitendijk, F., Daskopoulos, P., Vreenegoor, A., and Wang, H., 1996, "Computational fluid dynamics for chemical reactor engineering," Chemical Engineering Science, 51(10), pp. 1569-1594.
- [89] Frenklach, M., Wang, H., Yu, C., Goldenberg, M., Bowman, C., Hanson, R., Davidson, D., Chang, E., Smith, G., and Golden, D., 1995, "GRI-Mech-1.2, An Optimized Detailed Chemical Reaction Mechanism for Methane Combustion," Gas Research Institute.
- [90] Bowman, C., Hanson, R., Gardiner, W., Lissianski, V., Frenklach, M., Goldenberg, M., and Smith, G., 1997, "GRI-Mech 2. 11: An Optimized Detailed Chemical Reaction Mechanism for Methane Combustion and NO Formation and Reburning," NASA(19980005146).
- [91] Smith, G. P., Golden, D. M., Frenklach, M., Moriarty, N. W., Eiteneer, B., Goldenberg, M., Bowman, C. T., Hanson, R. K., Song, S., and Gardiner Jr, W., 2011, "GRI-Mech 3.0, 1999," URL http://www.me.berkeley.edu/gri_mech.
- [92] Fukumoto, K., and Ogami, Y., 2012, "Simulation of CO-H₂-air turbulent nonpremixed flame using the eddy dissipation concept model with lookup table approach," Journal of Combustion, 2012.
- [93] Russo, C., Mori, G., Anisimov, V. V., and Parente, J., "Micro gas turbine combustor emissions evaluation using the chemical reactor modelling approach," Proc. ASME Turbo Expo 2007: Power for Land, Sea, and Air, American Society of Mechanical Engineers, pp. 531-542.
- [94] Liu, F., Mu, Y., Liu, C., Yang, J., Mao, Y., Xu, G., and Zhu, J., "Effect of fuel staged proportion on NO_x emission performance of centrally staged combustor," Proc. ASME Turbo Expo 2013: Turbine Technical Conference and Exposition, American Society of Mechanical Engineers, pp. V01AT04A015-V001AT004A015.

- [95] Fichet, V., Kanniche, M., Plion, P., and Gicquel, O., 2010, "A reactor network model for predicting NO_x emissions in gas turbines," *Fuel*, 89(9), pp. 2202-2210.
- [96] Bragg, S., 1953, "Application of reaction rate theory to combustion chamber analysis," DTIC Document.
- [97] Rutar, T., Malte, P. C., and Kramlich, J. C., 2000, "Investigation of NO_x and CO formation in lean-premixed, methane/air, high-intensity, confined flames at elevated pressures," *Proceedings of the Combustion Institute*, 28(2), pp. 2435-2441.
- [98] Schlegel, A., Benz, P., Griffin, T., Weisenstein, W., and Bockhorn, H., 1996, "Catalytic stabilization of lean premixed combustion: method for improving NO_x emissions," *Combustion and Flame*, 105(3), pp. 332-340.
- [99] Feitelberg, A. S., Tangirala, V. E., Elliott, R. A., Pavri, R. E., and Schiefer, R. B., "Reduced NO_x diffusion flame combustors for industrial gas turbines," *Proc. ASME Turbo Expo 2000: Power for Land, Sea, and Air*, American Society of Mechanical Engineers, pp. V002T002A006-V002T002A006.
- [100] Falcitelli, M., Tognotti, L., and Pasini, S., 2002, "An algorithm for extracting chemical reactor network models from CFD simulation of industrial combustion systems," *Combustion science and technology*, 174(11-12), pp. 27-42.
- [101] Skjøth-Rasmussen, M. S., Holm-Christensen, O., Østberg, M., Christensen, T. S., Johannessen, T., Jensen, A., Glarborg, P., and Livbjerg, H., 2004, "Post-processing of detailed chemical kinetic mechanisms onto CFD simulations," *Computers & chemical engineering*, 28(11), pp. 2351-2361.
- [102] Falcitelli, M., Pasini, S., Rossi, N., and Tognotti, L., 2002, "CFD+ reactor network analysis: an integrated methodology for the modeling and optimisation of industrial systems for energy saving and pollution reduction," *Applied thermal engineering*, 22(8), pp. 971-979.
- [103] Novosselov, I. V., and Malte, P. C., 2008, "Development and application of an eight-step global mechanism for CFD and CRN simulations of lean-premixed combustors," *Journal of Engineering for Gas Turbines and Power*, 130(2), p. 021502.
- [104] Wormeck, J. J., 1986, *Computer modeling of turbulent combustion in a Longwell jet-stirred reactor*, University Microfilms.
- [105] Pratt, D. T., and Wormeck, J. J., 1976, *CREK-A Computer Program for Calculation of Combustion Reaction Equilibrium and Kinetics in Laminar or Turbulent Flow*, Thermal Energy Laboratory, Department of Mechanical Engineering, Washington State University.
- [106] Pratt, D. T., 1977, "Calculation of chemically reacting flows with complex chemistry," *Studies in convection: Theory, measurement and applications*, 2, pp. 191-220.

- [107] Chen, L., and Battaglia, F., 2015, "The effects of inlet turbulence intensity levels and computational domains on non-premixed bluff-body flame," ASME International Mechanical Engineering Congress & Exposition, IMECE2015-51048.
- [108] Rabitz, H., Kramer, M., and Dacol, D., 1983, "Sensitivity analysis in chemical kinetics," Annual review of physical chemistry, 34(1), pp. 419-461.
- [109] Tomlin, A. S., Turányi, T., and Pilling, M. J., 1997, "Mathematical tools for the construction, investigation and reduction of combustion mechanisms," Comprehensive chemical kinetics, 35, pp. 293-437.
- [110] Turányi, T., 1990, "Sensitivity analysis of complex kinetic systems. Tools and applications," Journal of mathematical chemistry, 5(3), pp. 203-248.
- [111] Turányi, T., 1997, "Applications of sensitivity analysis to combustion chemistry," Reliability Engineering & System Safety, 57(1), pp. 41-48.
- [112] Ansys, 2003, "Fluent User's Manual."
- [113] Jones, W. P., and Launder, B. E., 1972, "The prediction of laminarization with a two-equation model of turbulence," International Journal of Heat and Mass Transfer, 15(2), pp. 301-314.
- [114] Christo, F. C., and Dally, B. B., 2005, "Modeling turbulent reacting jets issuing into a hot and diluted coflow," Combustion and Flame, 142(1), pp. 117-129.
- [115] Yakhot, V., and Orszag, S. A., 1986, "Renormalization-group analysis of turbulence," Physical Review Letters, 57(14), pp. 1722-1724.
- [116] Shih, T. H., Liou, W. W., Shabbir, A., Yang, Z., and Zhu, J., 1995, "A new k- ϵ eddy viscosity model for high Reynolds number turbulent flows," Computer Fluids, 24(3), pp. 227-238.
- [117] Gibson, M. M., and Launder, B. E., 1978, "Ground effects on pressure fluctuations in the atmospheric boundary layer," Journal of Fluid Mechanics, 86(3), pp. 491-511.
- [118] Launder, B. E., 1989, "Second-moment closure: Presenty and future," International Journal of Heat Fluid Flow, 10(4), pp. 282-300.
- [119] Lübcke, H., Rung, T., and Thiele, F., 2001, "Comparison of LES and RANS in bluff-body flows," Journal of Wind Engineering and Industrial Aerodynamics, 89(14), pp. 1471-1485.
- [120] Ansys, 2009, "Determining Turbulence Parameters," Fluent User's Guide.
- [121] Ferziger, J. H., and Peric, M., 2012, Computational methods for fluid dynamics, Springer Science & Business Media.
- [122] Cheng, P., 1964, "Two-dimensional radiating gas flow by a moment method," AIAA journal, 2(9), pp. 1662-1664.

- [123] Siegel, R., and Howell, J. R., 1992, "Thermal radiation heat transfer, Hemisphere Pub," Corp., Washing ton DC.
- [124] Kontogeorgos, D., Keramida, E., and Founti, M., 2007, "Assessment of simplified thermal radiation models for engineering calculations in natural gas-fired furnace," *International Journal of Heat and Mass Transfer*, 50(25), pp. 5260-5268.
- [125] Gosman, A., and Lockwood, F., "Incorporation of a flux model for radiation into a finite-difference procedure for furnace calculations," *Proc. Symposium (International) on Combustion*, Elsevier, pp. 661-671.
- [126] Ilbas, M., 1997, *Studies of ultra low NOx burners*.
- [127] Ilbas, M., 2005, "The effect of thermal radiation and radiation models on hydrogen–hydrocarbon combustion modelling," *International Journal of Hydrogen Energy*, 30(10), pp. 1113-1126.
- [128] Chen, L., and Battaglia, F., 2017, "The Effects of Inlet Turbulence Intensity and Computational Domain on a Nonpremixed Bluff-Body Flame," *Journal of Energy Resources Technology*, 139(2), p. 022205.
- [129] Celik, I. B., Ghia, U., Roache, P. J., Freitas, C. J., Coleman, H., and Raad, P. E., 2008, "Procedure for estimation and reporting of uncertainty due to discretization in CFD applications," *ASME J. Fluids Eng.*, 130(7).
- [130] Durst, F., Fischer, M., Jovanović, J., and Kikura, H., 1998, "Methods to set up and investigate low Reynolds number, fully developed turbulent plane channel flows," *ASME J. Fluids Eng.*, 120(3), pp. 496-503.
- [131] Dibble, R., Warnatz, J., and Maas, U., 1996, "Combustion: physical and chemical fundamentals, modelling and simulations, experiments, pollutant formation," Springer, New York.
- [132] Han, Z., and Reitz, R. D., 1995, "Turbulence modeling of internal combustion engines using RNG k-epsilon models," *Combustion Science and Technology*, 106(4-6), pp. 267-295.
- [133] Liu, S., Hewson, J. C., Chen, J. H., and Pitsch, H., 2004, "Effects of strain rate on high-pressure nonpremixed n-heptane autoignition in counterflow," *Combustion and Flame*, 137(3), pp. 320-339.
- [134] Dally, B., Masri, A., Barlow, R., and Fiechtner, G., 1998, "Instantaneous and mean compositional structure of bluff-body stabilized nonpremixed flames," *Combustion and Flame*, 114(1), pp. 119-148.
- [135] Roquemore, W., Bradley, R., Stutrud, J., Reeves, C., and Obringer, C., 1984, "Utilization of laser diagnostics to evaluate combustor models," Air Force Wright Aeronautical Labs., Wright-Patterson AFB, OH (USA).

- [136] Masri, A., 1997, "Database available from Mechanical and Mechatronics Engineering, The University of Sydney, NSW 2006, Australia."
- [137] Bland, J. M., and Altman, D. G., 1996, "Statistics notes: measurement error," *Bmj*, 313(7059), p. 744.
- [138] Rood, E. P., and Telionis, D. P., 1991, "JFE Policy on Reporting Uncertainties in Experimental Measurements and Results," *ASME J. Fluids Eng.*, 113(9), pp. 313-314.
- [139] Kim, J. H., Simon, T. W., and Viskanta, R., 1993, "Journal of Heat Transfer Policy on Reporting Uncertainties in Experimental Measurements and Results," *Journal of Heat Transfer*, 115(1), pp. 5-6.
- [140] Coleman, H. W., and Steele, W. G., 1995, "Engineering application of experimental uncertainty analysis," *AIAA journal*, 33(10), pp. 1888-1896.
- [141] Coleman, H. W., and Steele, W. G., 2009, *Experimentation, validation, and uncertainty analysis for engineers*, John Wiley & Sons.
- [142] Drake, M., Correa, S., Pitz, R., Shyy, W., and Fenimore, C., 1987, "Superequilibrium and thermal nitric oxide formation in turbulent diffusion flames," *Combustion and Flame*, 69(3), pp. 347-365.
- [143] Blauvens, J., Smets, B., and Peters, J., 1977, "In 16th Symp.(Int'l.) on Combustion," The Combustion Institute, p. 1055.
- [144] Flower, W., Hanson, R., and Kruger, C., "Kinetics of the reaction of nitric oxide with hydrogen," *Proc. Symposium (International) on Combustion*, Elsevier, pp. 823-832.
- [145] Monat, J., Hanson, R., and Kruger, C., "Shock tube determination of the rate coefficient for the reaction $N_2 + O \rightarrow NO + N$," *Proc. Symposium (International) on Combustion*, Elsevier, pp. 543-552.
- [146] Baulch, D., Drysdall, D., Horne, D., and Lloyd, A., "Evaluated kinetic data for high temperature reactions, 1973," Butter Worths.
- [147] Hanson, R. K., and Salimian, S., 1984, "Survey of rate constants in the N/H/O system," *Combustion chemistry*, pp. 361-421.
- [148] De Soete, G. G., "Overall reaction rates of NO and N₂ formation from fuel nitrogen," *Proc. Symposium (international) on combustion*, Elsevier, pp. 1093-1102.
- [149] Warnatz, J., 1991, "NO_x formation in high temperature processes," University of Stuttgart, Germany.
- [150] Baulch, D., Cobos, C., Cox, R., Esser, C., Frank, P., Just, T., Kerr, J., Pilling, M., Troe, J., and Walker, R., 1992, "Evaluated kinetic data for combustion modelling," *Journal of Physical and Chemical Reference Data*, 21(3), pp. 411-734.

- [151] Westbrook, C. K., and Dryer, F. L., 1984, "Chemical kinetic modeling of hydrocarbon combustion," *Progress in Energy and Combustion Science*, 10(1), pp. 1-57.
- [152] Grudno, A., and Seshadri, K., 1996, "Characteristic residence times of laminar nonpremixed flames at extinction," *Combustion Science and Technology*, 112(1), pp. 199-210.
- [153] MacDonald, M. A., Jayaweera, T. M., Fisher, E. M., and Gouldin, F. C., 1998, "Variation of chemically active and inert flame-suppression effectiveness with stoichiometric mixture fraction," In *Symposium (International) on Combustion*, 27(2), pp. 2749-2756.
- [154] Zhao, D., Yamashita, H., Kitagawa, K., Arai, N., and Furuhashi, T., 2002, "Behavior and effect on NO_x formation of OH radical in methane-air diffusion flame with steam addition," *Combustion and Flame*, 130(4), pp. 352-360.
- [155] Novosselov, I. V., 2006, "Chemical reactor networks for combustion systems modeling," Phd Diss.
- [156] ANSYS, 2016, "ANSYS Chemkin Tutorials Manual 17.0," Reaction Design.
- [157] Glassman, I., Yetter, R. A., and Glumac, N. G., 2014, *Combustion*, Academic press.
- [158] Rezvani, R., 2010, "A conceptual methodology for the prediction of engine emissions."
- [159] Kee, R. J., Rupley, F. M., Meeks, E., and Miller, J. A., 1996, "CHEMKIN-III: A FORTRAN chemical kinetics package for the analysis of gas-phase chemical and plasma kinetics," Sandia national laboratories report SAND96-8216.
- [160] Hwang, Y., 1982, "On the proper usage of sensitivities of chemical kinetics models to the uncertainties in rate coefficients," *Proceedings of the National Science Council B. ROC*, 6, pp. 270-278.
- [161] Ray Jr, W. J., 1983, "Rate-limiting step: a quantitative definition. Application to steady-state enzymic systems," *Biochemistry*, 22(20), pp. 4625-4637.
- [162] Marzouk, O. A., and Huckaby, E. D., 2010, "A comparative study of eight finite-rate chemistry kinetics for CO/H₂ combustion," *Engineering applications of computational fluid mechanics*, 4(3), pp. 331-356.